An experimental investigation into the conversion of optical spin to orbital angular momentum using internal conical diffraction

By David O'Dwyer

A thesis submitted for the degree of
Doctor of Philosophy in the University of Dublin

School of Physics
Trinity College Dublin
Ireland

November 2010

Declaration:

This thesis has not been submitted as an exercise for a degree at this or any other University. The work presented is entirely my own, apart from the assistance mentioned in the acknowledgements. I agree that Trinity College Library may lend or copy this thesis upon request.

"Dave cannot die only the actor playing Dave can die"

A wise German man

Dedication:

To granddad:

'Education is no load to carry'

Abstract

Internal conical refraction (ICR) transforms a ray incident upon the optic axis of a biaxial crystal into a cone of light within the medium and a hollow cylinder of light upon exiting. If the incident ray is circularly polarised each of the electric field components is separated out forming a π rotation of linear polarisation around the ring. The phenomenon of ICR has recently been expanded to incorporate paraxial diffraction of the conical beam (ICD). The paraxial transformation of a Gaussian beam results in the radial electric field of the conical beam described as a superposition of Bessel functions of zero- and first-order. At the position of the Gaussian beam waist the sharpest image of the conical rings is formed, which diffracts into the far field forming an on axis intensity peak of intensity. A left-circularly polarised Gaussian light beam, which has spin angular momentum (SAM) J_{sp} = $\sigma\hbar$ = 1$\hbar$ per photon generates a superposition of orthogonally polarised zero and first-order Bessel like beams of equal amplitude. The zero-order beam is left-circularly polarised with zero orbital angular momentum (OAM) J_{orb} = $\ell\hbar$ = 0, while the first-order beam is right-circularly polarised but carries OAM of J_{orb} = 1$\hbar$ per photon in the form of an optical vortex with a net angular momentum of composite beam of ½$\hbar$ per photon. We demonstrate an all-optical process for the generation light beams with fractional OAM up to ± 1$\hbar$ using elliptically polarised light with a fractional SAM per photon.

The process in which a conically diffracted beam is propagated through a successive biaxial media is termed cascade conical diffraction. Right-circularly polarised light generates a right-handed optical vortex of order -1$\hbar$. Upon propagation of the first-order beam through a second biaxial crystal, the generated beam is a superposition of orthogonally polarised fields of order 0, -1 and -2. This SAM to OAM conversion provides a new method for the manipulation of optical vortices that is solely dependent on the incident polarisation and vortex handedness.

Conical diffraction of linearly polarised light in a biaxial crystal produces a beam with a crescent shaped intensity profile. Rotation of the plane of polarisation produces the unique effect of spatially moving the crescent shaped beam around a ring. We use this effect to trap microspheres to position them at any angular position on the ring. Continuous motion around the circle is also demonstrated. This crescent beam does not require an interferometeric arrangement to form it, nor does it carry orbital angular momentum.

Acknowledgements

I would like to acknowledge and express my profound gratitude to both John Donegan and James Lunney for their guidance and patience over the past four years. Their understanding, ideas and enthusiasm for this project was crucial for pushing us through the finer details of conical refraction/diffraction. I would like to thank Ciaran whom I shared this project with. I would like to think that we helped each other through the past few years, with his grasp of the detailed mathematics involved invaluable. This project would have not had progressed half as far if it was I alone trying to understand it all, thank you Ciaran. The recent addition of Paul Eastham to the Physics dept provided clarity and direction to our work on the angular momentum of light. Yury Rakovich for his sound advice and help in the lab. Kyle who has helped with the recent optical trapping work and simulation. Mick Lynch and Vincent Weldon also deserve a massive thank you; their expertise in free space optics was always forthcoming and immensely helpful.

Sir. Michael Berry, who advised and liaised with us on our publications and provided a helping hand enabling us to again associate Trinity College with conical refraction after 180 years. I would also like to thank Prof. Kishan Dholakia and Dr. Tomas Cizmar from the University of St. Andrews who allowed me to work in their lab. They were always very helpful and forthcoming with advice at conferences and the occasional emails. The fine images that you will see in this thesis would not have been possible without access to some very fine quality single crystal biaxial media provided by Croptics and Todor Kirilov.

Next on the list are my fellow basement dwellers, Rob, Ed, Pablo, Diarmuid, Dave and many more over the years. The troubleshooting, banter and general chit chat about physics and life in general was essential for keeping the sanity from the distinct lack of sunlight. Rob, Diarmuid, and the other members of IPDT and ACTTT thanks for the games of football, even though our teams never won a game it was immense fun! Thanks to my

housemates over the years Ed, Joe and Phil. There was some immense banter to be had over the years. Those years were some of the best I have ever had! Joe, Rob, Gman, Keith, Darren, Declan and all I have forgot to mention you are all great friends thank you. Naomi thanks for all the Skype's over the years since you left, the ranting to someone far away was fun.

My family Mam, Colm, Paul and Kevin for having to put up with me being the eternal student, those days are now over I am afraid. I have to somehow be an adult now albeit begrudgingly. I would like to thank Emma whom I met November 3 years ago. Experiencing the last three years with you far surpasses my PhD experiences. Thank you for listening to my Physics rants and putting up with my unfaltering clumsiness.

Finally, to my Granddad Patrick I dedicate this thesis. I remember the day when I told him I was attending Trinity College when he was in hospital nine years ago. The pride and joy he expressed that day will stay with me for a long time. To him I was on my way to do something that was never open to him or any of his family before. This thesis is as much his as it is mine.

List of publications and oral presentations:

Peer reviewed:

C. F. Phelan, D. P. O'Dwyer, Y. P. Rakovich, J. F. Donegan, and J. G. Lunney, "Conical diffraction and Bessel beam formation with a high optical quality biaxial crystal," Optics Express 17, 12891-12899 (2009).

D. P. O'Dwyer, C. F. Phelan, Y. P. Rakovich, J. F. Donegan, and J. G. Lunney, "Generation of continuously tunable fractional optical orbital angular momentum using internal conical diffraction," Optics Express, Vol. 18, Issue 16, pp. 16480-16485 (2010).

D. O'Dwyer, C. Phelan, K. Ballantine, Y. Rakovich, J. Lunney, and J. Donegan, "Conical diffraction of linearly polarised light controls the angular position of a microscopic object," Optics Express 18, 27319-27326 (2010).

D. O'Dwyer, C. Phelan, Y. Rakovich, P. Eastham, J. Lunney, and J. Donegan, "The creation and annihilation of optical vortices using cascade conical diffraction," Optics Express 19, 2580-2588 (2011).

Not peer reviewed:

D. P. O'Dwyer, C. F. Phelan, Y. P. Rakovich, J. F. Donegan, and J. G. Lunney, " Polarisation distribution for internal conical diffraction and the superposition of zero and first order Bessel beams.", SPIE Optics and Photonics 2008.

Talks and poster presentations:

D. P. O'Dwyer (poster), "Generation of continuously tunable fractional optical orbital angular momentum using internal conical diffraction". International conference on optical angular momentum, York 2010.

D. P. O'Dwyer (oral presentation), "Polarisation distribution for internal conical diffraction and the superposition of zero and first order Bessel beams." Presented at SPIE Optics and Photonics San Diego 2008.

D. P. O'Dwyer (poster), "Polarisation distribution for internal conical diffraction and the superposition of zero and first order Bessel beams." Photonics Ireland Galway 2009.

D. P. O'Dwyer (oral presentation), "Generation of light beams with non-integer orbital angular momentum via internal conical diffraction" Presented at Photonics Ireland Kinsale 2007.

Table of Contents

Chapter 1

INTRODUCTION

1.1 Abstract

This chapter provides the historical context for the discovery and experimental observation of internal conical refraction. Internal conical refraction proved to be a milestone in the history of the development of scientific method. Firstly it is the first recorded case of a theoretical investigation dictating the direction of experimental research. Secondly it provided the final verification of Fresnel's wave theory of light. Following the initial observation of conical refraction there has been sporadic investigations into the effect. The recent availability of high grade biaxial crystals has resulted in resurgence in the study of this optical effect. The number of publication based on conical refraction since work started on this thesis is now greater than all the proceeding years since the initial paper was submitted. This chapter provides a review of previous work in this area prior to submission of this thesis.

1.2 Introduction to conical refraction – Historical context

The phenomenon of conical refraction was first predicted by Sir W.R. Hamilton, Andrews Professor of Astronomy, Trinity College Dublin in 1832. It was demonstrated experimentally by Professor Humphrey Lloyd at the same university a year later [1]. Conical refraction occurs when light travelling along the optic axis of a biaxial crystal is refracted into a hollow cone within the crystal and emerges as a hollow cylinder of light. The theory of conical refraction is one of the first examples in physics where a mathematical prediction pre-dated the experimental research to confirm its validity. It is perhaps a surprise that such a discovery that was enthusiastically received at the time has been consigned to at best a side-note in only the most detailed optical physics texts. The textbooks by Landau and Lifshitz [2], Born and Wolfe[3] and Ditchburn [4] provide a detailed explanation of the propagation of electromagnetic waves in anisotropic media including conical refraction. A brief overview of the geometric theory published by Lunney and Weaire also provides an excellent and detailed explanation of the phenomenon [5]. The historical context leading up to and preceding the discovery of conical refraction has been dealt with in detail by O'Hara [6].

Dutch physicist Huygens first proposed the idea of light propagating as a transverse wave [7]. This was later expanded by Fresnel and is commonly referred to as the Fresnel-Huygens wave theory (chapter 12 of Ditchburn [4]). The refraction of light through isotropic media generates a symmetrical spherical wave surface where the propagation of the refracted wave is described by a single refractive index. Fresnel-Huygens approach also explains the optical effect known as birefringence where a ray of light refracted at the surface of a crystal of Iceland spar is refracted into two separate rays of light. One ray obeys the normal laws of refraction whilst the other is subject to a new

extraordinary law. The two rays exit the crystal linearly polarised in orthogonal planes. The wave surface for such a material is composed of a sphere describing the refraction of the ordinary ray and ellipsoidal surface describing the refraction of the extraordinary ray. The construction of such a surface is achieved using the Fresnel equation which maps out the wave surface as a function of crystallographic direction. From this surface the direction, polarisation and phase of a generated ray can be extracted. The direction of the propagation of a ray of light, which is the direction of energy flow of a wave, is determined from the normal to the tangent plane of the wave surface for given directions see Figure 1-1. In birefringence, a double-sheeted surface generates two rays one from each surface.

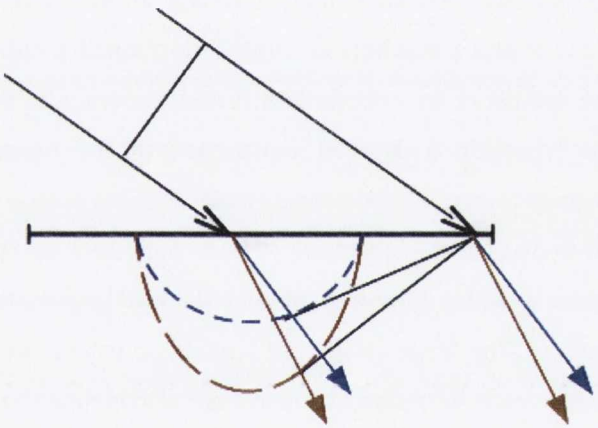

Figure 1-1: Huygens construct for double refraction. Two rays are generated from the tangent plane of each surface, the ordinary surface (blue) and extraordinary surface (red).

Materials that exhibit birefringence are either uniaxial or biaxial. Uniaxial crystals such as Iceland spar are characterised by two refractive indices and biaxial crystals have three principal refractive indices (page 98 of Landau and Lifshitz [2]). The Fresnel equation for uniaxial materials exhibits one direction within the crystal where the wave surfaces

intersect whilst a biaxial material has two (page 99 of Landau and Lifshitz [2]). The points of intersection on the wave surface correspond to a direction known as the optic axes. Hamilton's insight was that light propagating along the optic axis of a biaxial crystal does not have two tangent planes but a single tangent plane touching the wave surface along a circle of contact that generates a corresponding infinite number of rays forming the cone of internal conical refraction. Light refracts into a cone of light within the medium and exits as a hollow cylinder of light. The cone of internal conical refraction (ICR) is a slant cone of light, with the direction of the incident ray of light corresponding to the position on the cone that is tangentially polarised with respect to the ring.

Lloyd performed his experiments with a single crystal of aragonite. He observed the cone of external conical refraction by projecting the cone onto a glass plate using direct sunlight. Early the next year he observed the cone of internal conical refraction. Lloyd used a 12mm thick piece of aragonite with a pinhole approximately 200 μm in diameter generating a cone with a radius of 0.2mm [8]. He reported the formation of a single ring of light with zero intensity on axis, not too dissimilar from Figure 1-2 where the above parameters were used to simulate his experiment.

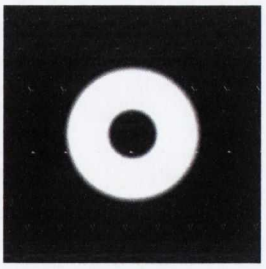

Figure 1-2: A simulation of the ring of ICR that Lloyd saw in 1833, with the zero on axis clearly seen.

Lloyd detailed the cone properties and discovered by observation with a tourmaline plate (linear polariser), that all rays of the cone were polarised in different planes. He observed a $\pi/4$ rotation of polarisation around a $\pi/2$ rotation around the cone axis. He also proved this to be a necessary consequence of Fresnel's theory.

The first major revision of ICR is attributed to Poggendorff (1839)[9]. Using a more refined technique, he observed a "dark" ring separating a double ring of light, Figure 1-3. Voigt explained this feature when he realised the infinity of rays refracted in the cone is actually a zero of intensity in the direction Hamilton's ideal axial ray, so Hamilton's cone should be dark, not bright[10]. From this, he concluded that Hamilton's ideal conical refraction does not exist. Instead, double refraction in the neighbourhood of the conical point gives rise to a pair of concentric cones, separated by a dark cone Figure 1-2.

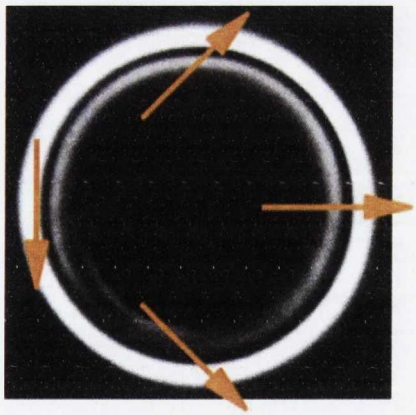

Figure 1-3: Experimental image of the double ring structure showing the polarisation structure and the Poggendorff dark ring.

Voigt deduced that light propagating thought the crystal has a range of k-vectors that describe the direction of propagation of the rays, the range of directions is proportional to an area around the conical point of

intersection on the wave surface. The light originating from the point of conical intersection is zero, the spread of directions around this point gives real solutions to the direction of the conically refracted rays, and revealing the commonly observed double ring structure of the conically refracted ring of light [10-11].

The first technical investigation of the effect of diffraction of the conical field was by Raman et al[12], who noted that by imaging the conical beam the sharpest ring structure is observed at the focus. As the beam diffracts away from this point the rings diffract and form an on axis intensity spike in the centre of the rings, corresponding to the direction of the optic axis of the wave surface. This experimental work was preceded by numerous attempts to qualitatively describe the propagation and subsequent diffraction of wavelets of light. Laylor [13] initially described the angular spread of a plane wave. Portigal [14] described qualitatively the direction of the Poynting vector for the rays propagating around the cone within the crystal. Belski and Khapalyuk [15] provided the first derivation of conically diffracted light accompanied by an experimental observation of conical diffraction [16]. In this thesis, the formulation provided by Berry [17-19], which is a reformulation of the work by Belski and Khapalyuk is used. Berry describes the biaxial crystal as a linear operator transforming the incident field using quite fittingly a Hamiltonian operator. This provides a full wave theory enabling the calculation of the electric field profile for any position in space as a function of incident polarisation and Fourier transformation of the incident electric field [18-22].

The main outcome of Berry's theory is the description of the conically diffracted field as a superposition of waves, whose radial electric field profiles are described by Bessel functions of differing order. The work of King et al. [23] provided the first demonstration of the up scaling of the order of the Bessel beam from internal conical diffraction (ICD), and the subsequent generation of an optical vortex in a spin to orbital angular

momentum conversion process. His work demonstrated that ICD could be used convert SAM into a corresponding OAM state either adding or subtracting from the OAM of the incident beam. The ability to manipulate both the SAM and OAM of a photon is important in the field of quantum encryption and cryptography[24-27]. Circularly polarised light may possess a maximum SAM value of ±1ħ per photon, depending upon the handedness of the light. OAM however does not such have a restriction upon the maximum value of the OAM per photon, increasing the density of information. Spin angular momentum is used in quantum cryptography to encode information in the form of polarisation (left- and right-hand circular polarisation are the quantum-mechanical spin eigen-states with respective spins of -ħ and +ħ per photon). OAM is not restricted to be just either ±1ħ per photon, but may possess many distinct OAM values. Information may then be encoded to carry a large amount of information in the form of a bit of quantum information called a qbit or qdit [28].

Bessel beams are widely used in the fields of optical trapping were their special properties such as self-repair and divergence-less propagation increases the depth of field of the trap enabling the stacking of particles [29]. Recent work by Jeffrey and Berry [30-31] investigated the properties of optical activity and chirality in conical diffraction. The polarisation/phase pattern in the full beam created by conical diffraction generated from a circularly polarised incident beam is an object with many given names: a "C-polarisation singularity" (Berry), a "half-vortex" or "Mermin-Ho vortex" (in Helium-3 and polariton condensates), or a "meron" (in generally field theory) [32].

Since work began on this thesis four years ago, there has been a resurgence of interest in this optical effect. Groups from Spain, Scotland[33] and Estonia[34] have begun their own experimental work into internal conical diffraction (ICD) fuelled by the access to high grade biaxial crystals specifically cut with their optic axis perpendicular to the

entrance face. One such example of progression within the field is the use of ICD in a laser cavity. It has been reported that a solid-state laser based on ICD generates a mode with excellent beam quality and slope efficiency close to the theoretical maximum[33,35-36]. Successive passages of light through a biaxial crystal in a cavity also lead to the development of cascade conical diffraction. This prompted Berry to expand his diffraction theory for n-cascaded crystals [37]. Ciaran Phelan, Trinity College Dublin (personal communication), has also independently reformulated the process of cascade ICD. ICD generates an off-axis cylinder of light of radius R_0 that directly depends upon the length of the crystal, the non-centred cone results in an angular dependence between the successive crystals on the final intensity profile.

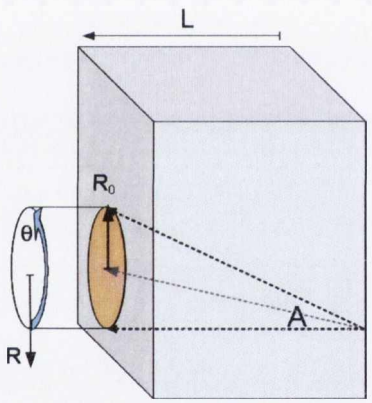

Figure 1-4: Refraction of a ray of light down the binormal of a biaxial medium forming a cylinder of light of radius R_0. R is the cone centred radial distance, (θ) angle around the beam axis and (A) is the cone angle.

The aim of the research presented in this thesis is to use the newly developed theory of conical diffraction in conjunction with the availability of high quality biaxial crystals to continue the investigation into the phenomenon of conical diffraction. Specifically the possibility of ICD as an optical vortex generator is investigated. ICD as it will be shown provides an interface by which the spin angular momentum of light can be coupled directly to the orbital component, providing a new means of

generating and controlling the total angular momentum of light. Finally, this research concludes by using ICD in an optical trap that demonstrates the angular momentum of the conical beam and the polarisation controlled intensity distribution around the ring to manipulate and control micron-sized particles.

1.3 Thesis overview

Chapter 2: This chapter provides a geometrical introduction into the phenomenon of internal conical refraction using Maxwell's electromagnetic theory. A ray of light incident on optic axis of the wave normal's of a biaxial crystal, the optic axis of the Fresnel wave surface, is transformed into a hollow, skewed slant cone of light within the medium and a hollow cylinder of light upon exiting the crystal. This phenomenon is known as internal conical refraction. Conical refraction is then expanded to incorporate the paraxial wave diffraction theory known as internal conical diffraction (ICD) as published by Berry. A Gaussian beam is transformed, by conical diffraction, into a diffracting double ring of light. In this case, the radius R_0 is the distance from the centre of the double ring profile to the intensity minimum between the double ring. The width of the double ring is of the order of the waist, w_0, of the incident Gaussian and the angular width of the rings is the same as that of the Gaussian [5,39]. Hence, a tightly focused Gaussian will be transformed into a narrow, highly divergent, double ring profile. The outer ring will diverge away from the propagation axis and the inner ring will converge towards it forming an intensity profile that is dominated by an axial peak in the far field. The ratio of the R_0 to w_0 determines the azimuthal intensity profile of the rings. The position of the ring profile, termed the focal image plane (FIP), occurs at the focal point of the focusing lens plus the increased optical path length due to the propagation of the light through a higher index medium. This enables

the direct imaging of the rings if the crystal is positioned before the focus or imaging of the ring with further lenses if the focus is positioned before the crystal as outlined in [39]. In both the near- and far-field the experimental profiles compare excellently with theory.

Chapter 3: Introduces the concept of the angular momentum of light. The total angular momentum of light is composed of both spin and orbital angular momentum (OAM) components. Spin angular momentum of a photon is more commonly referred to as polarisation and can be subsequently controlled with a quarter-wave plate. Initially we demonstrate that ICD transforms a circularly polarised Gaussian beam into a superposition of orthogonally polarised beams, one with a vortex and one without, giving the total OAM to be ½ħ per photon. The optical vortex is of same handedness as the generating polarisation and is easily isolated albeit with a loss of half the incident intensity. This chapter provides the experimental procedure for the control over the OAM per photon up to $\ell = \pm 1\hbar$ from an incident circularly polarised state of $\sigma = \pm 1\hbar$. This requires the use of polarisation optics plus a single biaxial crystal.

Chapter 4: This expands on the previous chapter with the introduction of a second biaxial crystal in a process termed cascade conical diffraction. The generated output upon exiting the second crystal will depend upon the respective orientation of the optic axes with respect to each other. If the cones of ICD are aligned parallel the cascade system acts like a single. Aligning the cones anti-parallel cancels the conical effect and the initial Gaussian beam is reformed. At intermediate angles, a compound structure is formed composed of the a and a central Gaussian spot. Varying the angles between 0 and 180° varies the power between both features. The SAM to OAM conversion properties of ICD are expanded further to include the possibilities of further addition and subtraction of optical vortices from the conical field, demonstrating the

flexibility ICD provides to the manipulation of OAM using polarisation optics.

Chapter 5: The ability to control and manipulate the position of micro-sized particles using the conically diffracted beam is presented in this chapter. Linear polarised light incident upon the biaxial crystal generates an intensity gradient around the ring. A particle confined in the position of maximum intensity on the ring can be positioned at any point on the ring by rotating the plane of polarisation incident upon the crystal. This method for the circulation mimics the circulation of a particle circulating due to the transfer of OAM, without need for absorption or backscatter off the particle. As a result the angular position of the confined particle can be directly controlled by controlling the orientation of the electric field of the linearly polarised beam incident upon the biaxial crystal. A cascade ICD optical trap based on the work presented in Chapter 4 is demonstrated. A pair of biaxial crystals in series with their optic axes rotated at a small angle to each other forms a ring + Gaussian spot. This enables a particle trapped on the ring to be rotated or positioned on the ring around a centrally trapped particle.

Chapter 6: A summary of the previous chapters is presented outlining the future possible avenues of research that can be continued as a result of the work performed in this thesis.

1.4 References

1 W. R. Hamiliton, "Third supplement to an essay on the theory of systems of rays," Transactions of the Royal Irish Academy **17**, 1-144 (1833).

2 L. Landau and E. M. Lifshitz, *Electrodynamics of Continuous Media*. (1984).

3 M.Born and E.Wolf, *Principles of Optics 7th Ed.* (Cambridge University Press, 7th Ed1999).

4 R. W. Ditchburn, *Light*. (Academic Press, London, 1975).

5 D. W. Weaire, J.G Lunney, "The ins and outs of conical refraction," Europhysics news **3** (37), 26-39 (2006).

6 J. G. O'Hara, "The Prediction and Discovery of Conical Refraction by William Rowan Hamilton and Humphrey Lloyd (1832-1833)," Proceedings of the Royal Irish Academy. Section A: Mathematical and Physical Sciences **82A** (2), 231-257 (1982).

7 F. J. Dijksterhuis, Lenses and waves : Christiaan Huygens and the mathematical science of optics in the seventeenth century (Kluwer Academic, Dordrecht ; London :, 2004).

8 H. Lloyd, "On the phenomenon presented by light in its passage along the axis of biaxial crystals,," Transactions of the Royal Irish Academy **17**, 145-158 (1833).

9 J.C. Poggendorff, "Ueber die konische Refraction,," Poggendorff Ann. **124** (11), 461-462 (1839).

10 D. Voigt, "Bemerkung zur Theorie der konischen Refraktion," Physics Z. **6**, 672-673 (1905a).

11 D. Voigt, "Theoretisches unt Experimentelles zur Aufklärung des optisches Verhaltens aktiver Kristalle," Annalen der Physik, **18**, 645-694 (1905b).

12 C. Raman, V. Rajagopalan, and T. Nedungadi, "Conical refraction in naphthalene crystals," Proceedings of Mathematical Sciences **14** (3), 221-227 (1941).

13 E. Laylor, "An Analytical Approach to the Theory of Internal Conical Refraction," Journal of Mathematical Physics, **13**, 449-454 (1972).

14 D. L. Portigal and E. Burstein, "Internal Conical Refraction," Journal of the Optical Society of America, **59** (12), 1567-1573 (1969).

15 A.M. Belskii and K. Khapalyuk, "Internal conical refraction of bounded light beams in biaxial crystals," Optical Spectroscopy (USSR) (44), 436–439 (1978).

16 A. J. Schell and N. Bloembergen, "Laser studies of internal conical diffraction. I. Quantitative comparison of experimental and theoretical conical intensity distribution in aragonite," Journal of the Optical Society of America, **68** (8), 1093-1098 (1978).

17 M. V. Berry, "Conical diffraction asymptotics: fine structure of Poggendorff rings and axial spike," Journal of Optics A **6** (4), 289 (2004).

18 M. V. Berry and M. J. Jeffrey, "Conical diffraction: Hamilton's diabolical point at the heart of crystal optics," Progress in Optics (50), 13-50 (2007).

19 M. J. Jeffrey,(PhD Thesis), Bristol, 2008.

20 M.V. Berry, R. Bhandari, and S. Klein, "Black plastic sandwiches demonstrating biaxial optical anisotropy," European Journal of Physics **20** (1), 1 (1999).

21 M. V. Berry, M. R. Jeffrey, and M. Mansuripur, "Orbital and spin angular momentum in conical diffraction," Journal of Optics A **7** (11), 685 (2005).

22 M V Berry, M R Jeffery, and J G. Lunney, "Conical diffraction: Observations and theory," Proceedings of the Royal Society A **462** (2070), 1629-1642 (2006).

23 T. A. King, W. Hogervorst, N. S. Kazak, N. A. Khilo, and A. A. Ryzhevich, "Formation of higher-order Bessel light beams in

biaxial crystals," Optics Communications **187** (4-6), 407-414 (2001).

24 Jennewein T. Gröblacher S., Vaziri A., Weihs G., and Zeilinger A., "Experimental quantum cryptography with qutrits," New Journal of Physics **8** (5), 75 (2006).

25 S. Franke-Arnold, S. Barnett, E. Yao, J. Leach, J. Courtail, and and M. Padgett., "Uncertainty principle for angular position and angular momentum," New Journal of Physics **6** (1), 103 (2004).

26 L. Chen and W. She, "Increasing Shannon dimensionality by hyperentanglement of spin and fractional orbital angular momentum," Optics Letters **34** (12), 1855-1857 (2009).

27 S. Straupe and S. Kulik, "Quantum optics: The quest for higher dimensionality," Nature Photon **4** (9), 585-586 (2010).

28 J.P. Torres G. Molina-Terriza, L. Torner, "Twisted Photons," Nature Physics **3** (305), 305-310 (2007).

29 D. McGloin and K. Dholakia, "Bessel beams: diffraction in a new light," Contemporary Physics **46** (1), 15 - 28 (2005).

30 M. R. Jeffrey, "The spun cusp complexified: complex ray focusing in chiral conical diffraction," Journal of Optics A: Pure and Applied Optics **9** (7), 634 (2007).

31 M.R Jeffrey, University of Bristol, 2005 (Personal Correspondence).

32 Volovik. E. , *The Universe in a Helium Droplet*. (Oxford University Press, 2009).

33 A. Abdolvand, K. G. Wilcox, T. K. Kalkandjiev, and E. U. Rafailov, "Conical refraction Nd:$KGd(WO_4)_2$ laser," Optics Express **18** (3), 2753-2759 (2010).

34 V. Peet, "Biaxial crystal as a versatile mode converter," Journal of Optics **12** (9), 095706 (2010).

35 A. J. Schell and N. Bloembergen, "Laser studies of internal conical diffraction. I. Quantitative comparison of experimental and

theoretical conical intensity distribution in aragonite," Journal of the Optical Society of America A **68** (8), 1093 (1978).

36 H. H. J. Hellström, V. Pasiskevicius, U. Bünting, and D. Haussmann, "Polarisation-tunable Yb:KGW laser based on internal conical refraction," Optics Letters **32** (19), 2783-2786 (2007).

37 M. V. Berry, "Conical diffraction from an N -crystal cascade," Journal of Optics **12** (7), 075704 (2010).

38 M. V. Berry and M. R. Jeffrey, "Chiral conical diffraction," Journal of Optics A **8** (5), 363 (2006).

39 C.F. Phelan, D.P O'Dwyer, Y.P. Rakovich, J.F. Donegan, and J.G. Lunney,
"Conical diffraction and Bessel beam formation with a high optical quality biaxial crystal " Optics Express **17** 12891-12899 (2009).

CHAPTER 2

CONICAL DIFFRACTION

2.1 Abstract

Biaxial media are direction dependent materials where the laws of refraction for rays of light entering or leaving such a medium dependent on the direction of the refracted ray. The propagation of light through biaxial media is discussed in this chapter in terms Maxwell's electromagnetic wave theory. The initial prediction and observation of internal conical refraction by Hamilton and Lloyd considered the propagation of only a single ray or a bunch of rays in a single direction down the optic axis. Subsequent expansions of Hamilton's initial theory to incorporate the refraction of rays with a narrow range of directions revealed a fine double ring structure. This expansion of Hamilton's theory to incorporate the diffraction of the conically diffracted beam is treated according to the paraxial wave theory as developed by Belski, Berry and others. The recent access of laser grade biaxial media has revitalised experimental interest in this very old optical phenomenon. The work in this chapter resulted in the first publication on conical refraction, now termed conical diffraction and marked the beginning of a resurgence of interest in this optical effect

C. F. Phelan, D. P. O'Dwyer, Y. P. Rakovich, J. F. Donegan, and J. G. Lunney, *"Conical diffraction and Bessel beam formation with a high optical quality biaxial crystal," Optics Express* ***17*** *(15), 12891-12899 (2009).*

2.2 Propagation of light in biaxial media – Conical refraction

The propagation of light through anisotropic media will be presented using the terminology of Landau from [1] and Ditchburn [2]. An isotropic medium such as glass or air is characterised by a single refractive index, regardless of the direction in which the light propagates. The light is refracted and reflected according to Snell's law. The propagation of an electromagnetic wave through an isotropic medium the displacement vector **D** is related to the electric vector **E** by the relation **D** = ε**E**, where ε is the dielectric constant which is related to the refractive index n = $\sqrt{\varepsilon}$.

In an optically anisotropic medium, the permittivity is no longer a scalar quantity but described as a tensor, which changes the direction and magnitude of a vector. As a result, the electric field **E** is no longer restricted to be in the same direction as **D**. The dielectric tensor ε (and consequently the refractive index) now depends upon direction as well as frequency in the discussion that follows this is kept constant. The relationship between **E** and **D** is now expressed as a function of propagation direction within the medium,

$$D_i = \varepsilon_{ik} E_k = \begin{pmatrix} D_x \\ D_y \\ D_z \end{pmatrix} = \begin{pmatrix} \varepsilon_{xx}E_x + \varepsilon_{xy}E_y + \varepsilon_{xz}E_z \\ \varepsilon_{yx}E_x + \varepsilon_{yy}E_x + \varepsilon_{yz}E_z \\ \varepsilon_{zx}E_x + \varepsilon_{zy}E_y + \varepsilon_{zz}E_z \end{pmatrix} \tag{2.1}$$

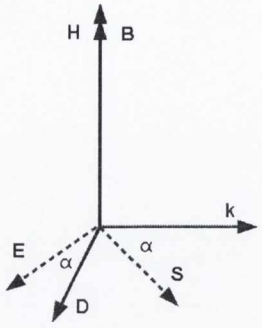

Figure 2-1: In anisotropic media, E and hence S are no longer parallel to D and k.

The wave vector **k** can now be used to define a vector **n**, describing the magnitude of the refractive index as a function of direction. In an isotropic medium n is independent of direction, but for anisotropic media the magnitude of the vector depends upon direction. The direction and magnitude of a given wave vector is given by,

$$\mathbf{k} = \frac{\omega \mathbf{n}}{c}, \tag{2.2}$$

$$\mathbf{D} = \mathbf{n} \times (\mathbf{E} \times \mathbf{n}) = n^2 \mathbf{E} - (\mathbf{n} \cdot \mathbf{E})\mathbf{n}. \tag{2.3}$$

Equating Eq. (2.3) to (2.1) the linear homogenous equations in terms of the three principal dielectric constants ε_{ik} gives,

$$E_k \varepsilon_{ik} = n^2 E_i - n_i n_k E_k. \tag{2.4}$$

This equation is only valid when the determinant of the coefficients equal zero. The determinant is evaluated by defining the axes of the tensor ε_{ik}, such that the principal values of the tensors are ε_x, ε_y, ε_z. The final form is the Fresnel equation, using the coordinate system n_x, n_y, n_z gives the equation,

$$n^2\left(\varepsilon_x n_x^2+\varepsilon_y n_y^2+\varepsilon_z n_z^2\right)-$$
$$\left[n_x^2\varepsilon_x\left(\varepsilon_y+\varepsilon_z\right)+n_y^2\varepsilon_y\left(\varepsilon_x+\varepsilon_z\right)+n_z^2\varepsilon_z\left(\varepsilon_y+\varepsilon_x\right)\right]. \qquad (2.5)$$
$$+\varepsilon_x\varepsilon_y\varepsilon_z=0$$

For a monochromatic wave, the magnitude of the wave-vector is solely a function of direction. Solving Eq. (2.5) gives n^2 as a quadratic. The general solution for n for all directions generates two different magnitudes for the wave vector for a given direction. This when mapped around all possible directions generates a double-sheeted surface known as the wave surface or wave vector surface describing the generated wave vectors as a function of direction. Using the wave surface one is able to define a reciprocal surface known as the ray surface, which defines the direction of propagation of the rays for the corresponding directions of the wave surface. The normal to the tangent plane of the wave surface generates the corresponding ray. The two separate solutions to the wave surface generate two separate rays one from each solution to the wave surface. This is the optical effect known as birefringence. The properties of the wave surface depend upon the symmetry of the tensor from Eq. (2.1). Uniaxial materials have two principal dielectric axes, and biaxial material has all three principal values of the tensor different. As a consequence of this, there exist directions known as the optic axes where, the solution of Eq. (2.5) is single valued. In a uniaxial material, there exists one such direction and in a biaxial direction, there are two.

Using the wave-vector surface the direction of the resulting refracted rays can be determined. The directions of the rays are given by the vector **s** and are related to the wave vectors **n** by,

$$\mathbf{n}\cdot\mathbf{s}=1 \qquad (2.6)$$

The direction of the propagating rays defines the direction of energy flux or Poynting vector **S.** This relationship enables the transposing of the

wave surface on to a ray surface via a simple conversion of variables creating a reciprocal surface. The conversion of the wave surface to the ray surface is achieved using the following change of variables.

$$\mathbf{E} \leftrightarrow \mathbf{D},\ \mathbf{n} \leftrightarrow \mathbf{s},\ \varepsilon_{ik} \leftrightarrow \varepsilon^{-1}{}_{ik},$$

From each value of the wave vector, the direction of the corresponding ray is the normal of the tangent plane at that point. This enables the definition of the Fresnel ray surface, quadratic in s^2 giving the general solution for two rays of different wave vectors,

$$s^2(\varepsilon_y\varepsilon_z s_x^2 + \varepsilon_x\varepsilon_z s_y^2 + \varepsilon_x\varepsilon_y s_z^2) - [s_x^2(\varepsilon_y + \varepsilon_z) + s_y^2(\varepsilon_x + \varepsilon_z) + s_z^2(\varepsilon_y + \varepsilon_x)] + 1 = 0 \tag{2.7}$$

Biaxial materials are characterised by three different principal values for the tensor ε_{ik}, with,

$$n_x < n_y < n_z \rightarrow \varepsilon_x < \varepsilon_y < \varepsilon_z \tag{2.8}$$

To define the spatial structure of the wave surface in terms of the principal coordinate planes Eq. (2.5) has $n_z = 0$ with the results giving the intersection with the coordinate planes.

$$\left(n^2 - \varepsilon_z\right)\left(\varepsilon_x n_x^2 + \varepsilon_y n_y^2 - \varepsilon_x\varepsilon_y\right) = 0 \tag{2.9}$$

The double sheeted surface in the x-y plane consists of a circle, whose normal generates the ordinary ray,

$$n^2 = \varepsilon_z, \tag{2.10}$$

and an ellipse defining a normal defines the direction of the extraordinary ray,.

$$\frac{n_x^2}{\varepsilon_y} + \frac{n_y^2}{\varepsilon_x} = 1. \tag{2.11}$$

This surface has two sheets that touch at four points in the x-y plane. Thus, the n_x intercepts are $\sqrt{\varepsilon_x}$ and $\sqrt{\varepsilon_z}$. Similarly, the n_y intercepts are $\sqrt{\varepsilon_y}$ and $\sqrt{\varepsilon_z}$ and the n_z intercepts are $\sqrt{\varepsilon_x}$ and $\sqrt{\varepsilon_y}$. Figure 2-2 shows the wave vector surfaces as 2-D slices in the (a) z-y and (b) x-y planes showing the wave vector surfaces forming an ellipse and a circle in the plane. Figure 2-3(a) shows the n_x-n_z plane, revealing the directions of the optic axes at an angle β to the x-axis. When β is parallel to either x-axis the material becomes uniaxial. The direction of the optic corresponds to a point of degeneracy, where the wave vector has only one magnitude. Figure 2-2(b) shows a 3D cut away of the wave surface revealing the point of degeneracy occurs in each quadrant of the plane.

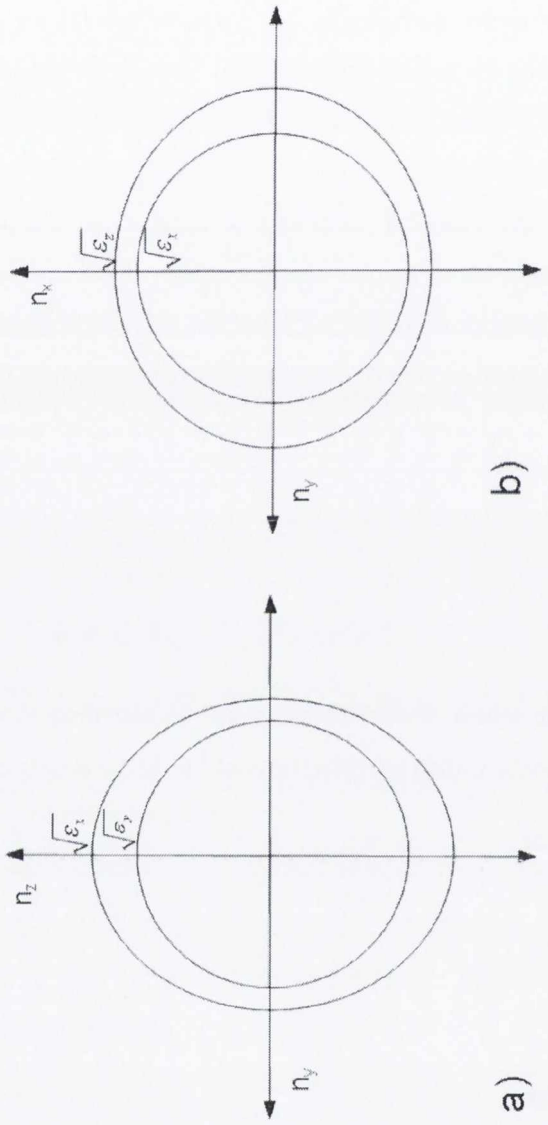

Figure 2-2: Wave vector surfaces (a) z-y plane,(b) x-y plane. For any wave propagation in any direction, there are two solutions to the ray surface.

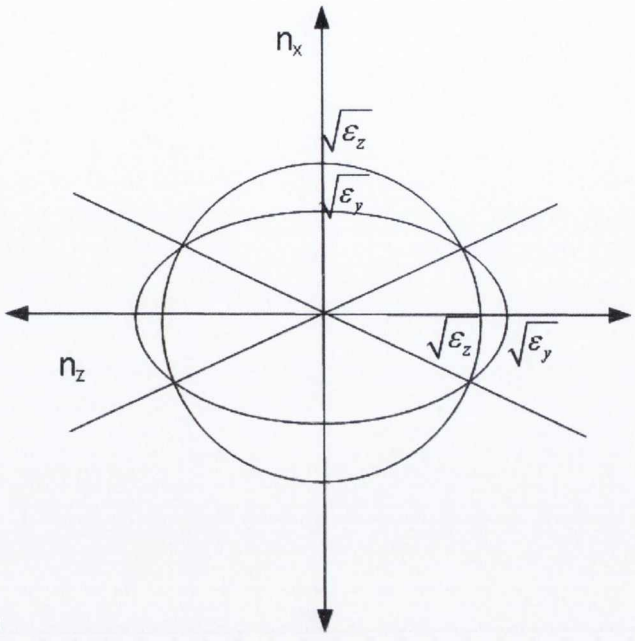

(a)

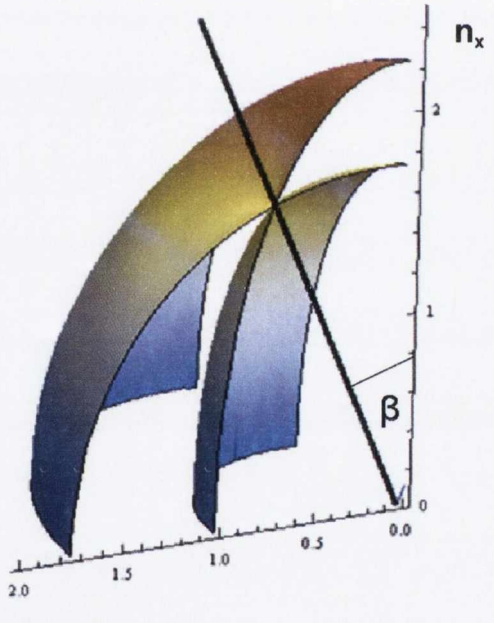

(b)

Figure 2-3: Wave vector surface in x-z plane showing the intersection of the wave surfaces and the directions of the optic axes. (b) Octant of the wave surface in the x-z plane Intersection between the sheets denoted the direction of the optic axis.

The direction in which the degeneracy will occur is obtained by differentiating Eq. (2.5) and setting n_y to zero,

$$n_x^2 = \frac{\varepsilon_z\left(\varepsilon_y - \varepsilon_x\right)}{\varepsilon_z - \varepsilon_x}, n_z^2 = \frac{\varepsilon_x\left(\varepsilon_z - \varepsilon_y\right)}{\varepsilon_z - \varepsilon_x} \tag{2.12}$$

The angle (A) these coordinates make with the z-axis is simply given by

$$\frac{n_x}{n_y} = \pm\tan\beta = \sqrt{\frac{\varepsilon_z\left(\varepsilon_y - \varepsilon_x\right)}{\varepsilon_x\left(\varepsilon_z - \varepsilon_y\right)}} \tag{2.13}$$

In this direction, the wave vector generates infinity of rays as a result of Eq.(2.14) being indeterminate, this is determined by manipulating Eq.(2.7) and (2.5), noting Eq.(2.6),

$$\frac{s_x}{n_x} = \frac{\varepsilon_x\left(\varepsilon_y + \varepsilon_z\right) - 2\varepsilon_x n_x^2 - \left(\varepsilon_x + \varepsilon_z\right)n_z^2}{2\varepsilon_x\varepsilon_y\varepsilon_z - n_x^2\varepsilon_x\left(\varepsilon_y + \varepsilon_z\right) - n_y^2\varepsilon_y\left(\varepsilon_x + \varepsilon_z\right) - n_z^2\varepsilon_z\left(\varepsilon_x + \varepsilon_y\right)} = 0 \tag{2.14}$$

A single tangent plane normal to the direction of the wave vector touches the surface not at one or two points but in an infinity of points tracing out a circle of contact on the wave vector surface creating a corresponding infinity of rays.

To determine the cone of rays as light propagates in the material, it is useful to examine the relationship between the ray and wave surface in. The outer rings (solid) are the ray surface and the inner rings (dashed) define the wave surface. Light propagating along the optic axis of the wave surface, defined by the line (O-n) generates a corresponding infinity of rays on the tangent plane of the ray surface forming the cone of internal conical refraction (Oab). The direction Os is also known as the diabolical point of intersection between the wave and ray surfaces, and one exists in each quadrant of the z-x plane.

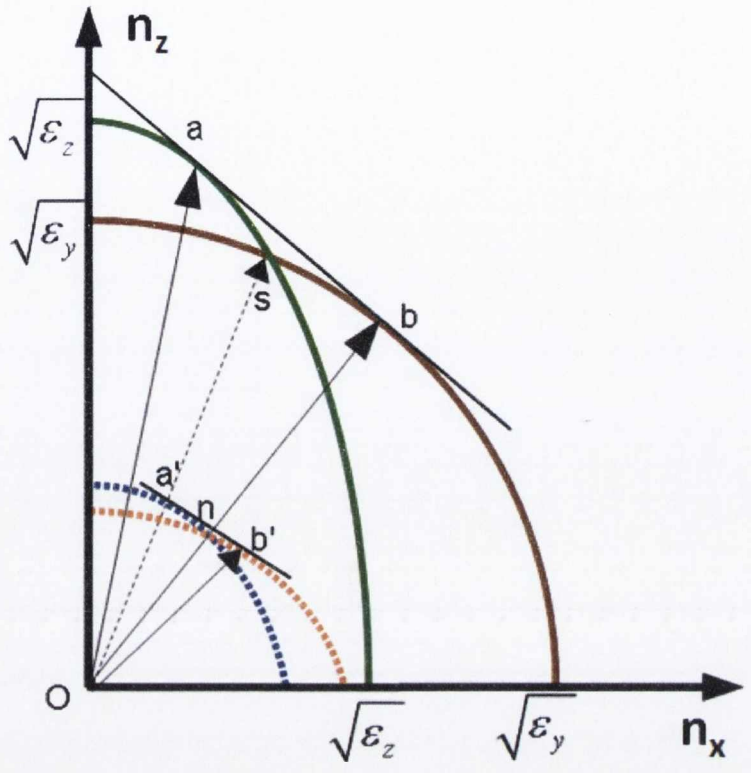

Figure 2-4: Depiction of the wave surface cone –solid lines (Oab) and ray surface - dashed (Oa'b'). Line Ob is the binormal, Os is the biradial.

Figure 2-5 shows the transition from double refraction to conical refraction in our experimental arrangement. Figure 2-5(a) shows light propagating slightly off the direction of the optic axis, undergoes double refraction. As the light is directed closer to the optic axis light is refracted around either side of the cone and the ring of light begins to form. When the direction of the light corresponds to the optic axis the light is refracted symmetrically around the cone of ICR forming a ring of light Figure 2-4(c).

The polarisation profile around the ring contains a π rotation of polarisation around the beam axis. Each point on the ring is linearly polarised, rotating from the point of the ordinary ray in the x-z plane

(line 0-a in Figure 2-4) around to the orthogonally polarised point corresponding to the surface defining the extraordinary ray (line 0-b in Figure 2-4). The polarisation distribution around the ring is shown Figure 2-6.

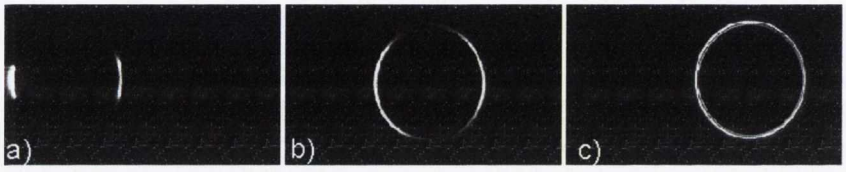

Figure 2-5: Transition from double refraction to ICR. (a) Shows double refraction near away from the binormal. (b) Refraction of light around the binormal, light is being refracted around the cone. (c) Ring of internal conical refraction, light is refracted into a symmetrical ring of light

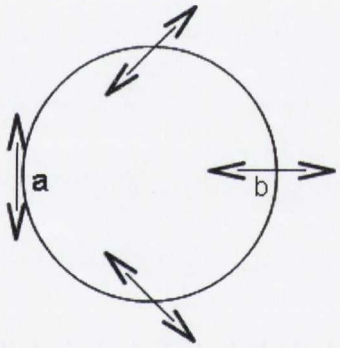

Figure 2-6: Polarisation distribution around the ring of ICR. Points a,b corresponds to the Figure 2-4 wave surface showing the ring of contact.

The angle of the cone Oab of ICR is given by Eq. (2.15). The resulting radius R_0 of the ring of light is given by the cone angle (A) times the length (L) of the crystal Eq. (2.16),

$$Tan2A = n_2^2 \sqrt{\left(\frac{1}{n_2} - \frac{1}{n_1}\right)\left(\frac{1}{n_3} - \frac{1}{n_2}\right)} \tag{2.15}$$

Giving the radius of the cone upon exiting the crystal

$$R_0 = AL \tag{2.16}$$

Conversely light propagating along the biradial line of Figure 2-4 determines the direction of single ray velocity generating the cone of external conical refraction Oa'b'. When a hollow cone of rays is incident upon the crystal, each wave normal is in the direction of the single ray velocity. The emergent beam is refracted into a similar cone from which is derived. This phenomenon is not investigated in this study and will not be mentioned further.

2.3 Conical diffraction

The theory of internal conical refraction as derived by Hamilton only considered the propagation of parallel rays down the optic axis, and consequently the general relationship between **n** and **s** is indeterminate (Eq.(2.14)). Experimentally however, one always has a system of rays with a finite angular spread. Later observations by Poggendorff[3] and Potter[4] using a more refined technique with a smaller aperture, restricting the range of angles of the incident rays revealed a double ring of light on either side of a dark ring now termed the Poggendorff ring. Voigt [5] explained this effect as a result of rays propagating at a slight angle (ϕ) to the optic axis. Rays that do not propagate along the optic axis are consequently not conically refracted but undergo double refraction.

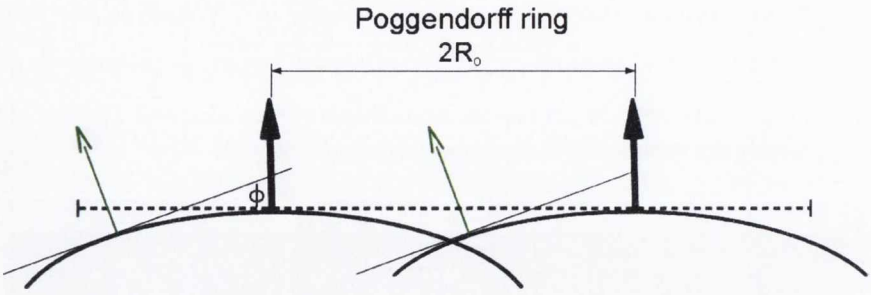

Figure 2-7: Segment of the z-x plane of a wave surface near the diabolical point. Dashed line is the single tangent plane of ICR, with the black arrows the rays of ICR. Rays (green) propagating off axis to the optic axis by angle ϕ are double refracted, generating two rays one from each sheet of the wave surface.

Rays at an inclined angle ϕ to the optic axis give rise to a pair of rays at an angle ($\frac{1}{2}A + \phi$) and ($\frac{1}{2}A - \phi$) to the central axis Figure 2-7 (section 16.26 of [6]). This, when expanded to include all off axis rays forms two cones of doubly refracted light. It can be shown that all the energy in the angular range of ϕ and ($\phi + \Delta\phi$) will appear in two cones of semi-aperture ($\frac{1}{2}A \pm \phi$). The intensity of light from the cones is proportional to the angle ϕ, and is zero when $\phi = 0$. Consequently, an angular spread of rays will be doubly refracted into two solid cones inside and outside the cone of ICR, with a dark cone of ICR having zero intensity. The double refraction of each ray around the cone also preserves the polarisation change around the beam axis. Therefore each doubly refracted ray is separated into two orthogonally linearly polarised states on diametrically opposed sides of the ring. The dark cone of ICR generated is the Poggendorff dark ring with a radius of R_0, as seen in Figure

2-8. A direct consequence of including the refraction of the off axis rays is the change in intensity distribution as the conical beam propagates, as noted by Raman in 1941[7].

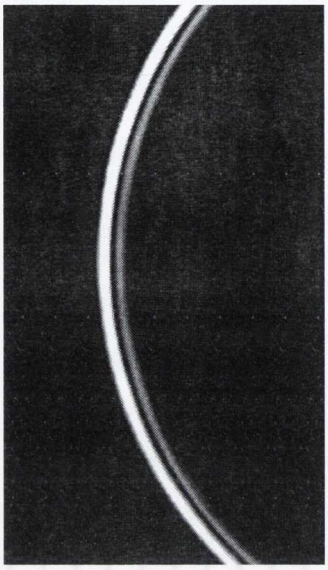

Figure 2-8: Magnified experimental image of the double ring of ICR. A dark Poggendorff ring separates two bright rings.

In order for interference and phase effects to be taken into account as the beam diffracts, a full wave theory needed to be developed. Attempts to achieve this were made by Laylor [8] and Schnell [9] and Portigal[10], but it was not until Belsky and Khapalyuk [11] [12] incorporated the simplification that paraxiality provides did a full wave theory become available. The paraxial approximation can be summarised as follows, the electric field written in standard complex notation given by a plane wave and a slowly varying envelope is,

$$\mathbf{A}(\mathbf{r},t) = \mathbf{u}(\mathbf{R},z)e^{i(kz-\omega t)}, \qquad (2.17)$$

where **A**(**r**,t) is a complex electric field, **u**(**R**,z) is the amplitude, R = (x,y) is the transverse 2D position vector , **r** = (**R**,**z**) is the position vector in three dimensions and ω = ck. The complex scalar function describing the

distribution of the field amplitude satisfies the paraxial wave equation when the transverse profile of A varies slowly with z [13].

$$\left(\frac{\partial^2}{\partial \mathbf{R}^2}+2ik\frac{\partial^2}{\partial z^2}\right)\mathbf{u}(\mathbf{R},z)=0 \tag{2.18}$$

The paraxial approach taken later by Berry is derived and explained in detail in references [14-16]. The following is a basic overview of the transformation and consequences of a paraxial approach to internal conical diffraction applying the methodology of Berry [16].

A biaxial slab of length L has three principal dielectric constants ε_i and refractive indices n_i such that,

$$\varepsilon_1 = n_1^2 < \varepsilon_2 = n_2^2 < \varepsilon_3 = n_3^2 . \tag{2.19}$$

The crystal wave number along the optic axis is given as,

$$k = n_2 k_0 . \tag{2.20}$$

This enables the description of the cone centred radial position of R around the azimuthal angle of the cone (θ) in terms of the transverse wave vectors as $k\mathbf{P} = k(P_x, P_y) = kP(\cos\theta_P, \sin\theta_P)$, where $P \ll 1$ as a consequence of paraxiality. A Hamiltonian operator transforms the linear state of the transverse profile of a paraxial beam, where the wave vector is k_0 along the optic axis. After a lengthy calculation the electric field of a conically diffracted paraxial beam is described in terms of R the radial component and Z the propagation distance and the Fourier transform of the incident electric field profile **a(P)** as,

$$\mathbf{E}(\mathbf{R},Z)=\frac{k}{2\pi}\iint e^{ik\left(\mathbf{P}\cdot\mathbf{R}-\frac{1}{2}ZP^2\right)}\times\left[\cos(kPR_0)\mathbf{I}-i\sin(kPR_0)B(kPR_0)\mathbf{M}(\theta_P)\right]\mathbf{a}(\mathbf{P})d\mathbf{P} \tag{2.21}$$

,

$$\mathbf{M}(\theta_P)=\begin{pmatrix}\cos\theta_P & \sin\theta_P\\ \sin\theta_P & -\cos\theta_P\end{pmatrix}, \tag{2.22}$$

I is the identity matrix and R_0 is the radius of the cylinder after exiting the crystal. Z denotes the effective propagation distance in units of n_2 from the position of the beam waist,

$$Z=L+(z-L)n_2, \tag{2.23}$$

where L is the length of the medium and z is the distance from the entrance face. This can also be referred to as the longitudinal shift, as propagation through a higher refractive index medium changes the optical path travelled by the beam.

Using Eq. (2.21) one can determine the electric field profile of the conical beam at any point in space in terms of polarisation and the Fourier transform of the incident electric field. Assuming that the incident beam is Gaussian, uniformly polarised and circularly symmetric and of the form of Eq. (2.24) one can compare theory with experiment.

$$\mathbf{E}(\mathbf{R},0)=e^{-\left(R^2/2w^2\right)}\begin{pmatrix}e_x\\ e_y\end{pmatrix}, \tag{2.24}$$

(e_x,e_y) represents the polarisation Jones matrix such that $|e_{x0}|^2+|e_{y0}|^2=1$. These Jones matrices can be expressed in a reduced form in terms of left (e^+) and right (e^-) circular polarisations. The corresponding Fourier transform of Eq.(2.24) is of the form,

$$a(P)=kw^2e^{-\frac{1}{2}k^2P^2w^2}. \tag{2.25}$$

Substituting Eq. (2.25) into Eq.(2.21) and performing the integration in momentum space to convert it into a real space electric field profile yields Eq. (2.26). The B_0 integral Eq. (2.27) described by a zero-order Bessel function (J_0) and the B_1 integral Eq. (2.28) described by a first-order Bessel function (J_1) are generated in superposition.

$$\mathbf{E}(R,z) = B_0(R,R_0,Z)\begin{pmatrix} e_x \\ e_y \end{pmatrix} + B_1(R,R_0,Z)\mathbf{M}(\theta_P)\begin{pmatrix} e_x \\ e_y \end{pmatrix} \qquad (2.26)$$

$$B_0(R,R_0,Z) = k\int_0^\infty P\cos(kPR_0)a(P)J_0(kpR)e^{-\frac{1}{2}ikP^2Z}dP \qquad (2.27)$$

$$B_1(R,R_0,Z) = k\int_0^\infty P\sin(kPR_0)a(P)J_1(kpR)e^{-\frac{1}{2}ikP^2Z}dP \qquad (2.28)$$

These are the exact paraxial solutions for the E field of the conical beam enabling the numerical calculation of any plane normal to the propagation.

The experimental arrangement for the observation of ICD from a Gaussian incident beam is presented in Figure 2-9. A 10 mW 632 nm Gaussian laser beam linearly polarised in the horizontal plane is left circularly polarised using a quarter wave plate P2, with the fast axis making an angle of 45° to the horizontal. The light is focused using a x10 objective lens (L_1) to a $1/e^2$ width beam waist size (w) of 14 μm. This is then directed down the optic axis of a 3 cm slab of the biaxial crystal $KGd(WO_4)_2$, oriented such that the plane containing the two optic axes also lies in the horizontal plane. At 632 nm the refractive indices are: n_1 = 2.01169, n_2 = 2.042198 and n_3 = 2.09510 determined from the Semillon equations for this material[17]. Using Eq. (2.15)and (2.16) gives a $R_0 = 5.9\times10^{-4}$ m resulting in $\rho_0 = R_0/w = AL/w = 42.1$. Setting Z = 0 in Eq. (2.23) results in a shift of focus of the position of the Gaussian beam waist by

$$Z = L\left(1 - \frac{1}{n_2}\right). \tag{2.29}$$

The position corresponding to Z = 0 is known as the Focal Image Plane or FIP. The position of the FIP lies 1.53 cm away from the position of the focus for the Gaussian beam. In this geometry, the position of the FIP lies inside the crystal and needs to be imaged onto a CCD. This is achieved using a 10cm lens (L_2) placed 20cm away from the Z = 0 position, which is 1.53 cm in front of the focal position of the lens L_1. The resulting 1:1 image is captured on a standard CCD 20cm away from L_2.

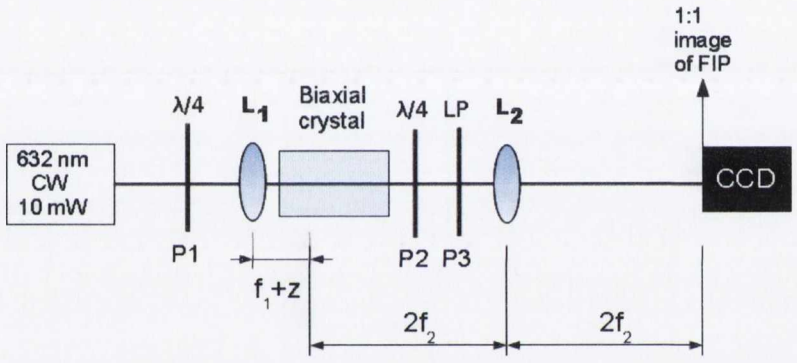

Figure 2-9: Experimental arrangement for the imaging of the FIP. Lens L_1 is an x20 objective with a focal length of 8.5mm. Imaging lens L_2 is a 10cm converging lens placed 20cm away from FIP imaging 1:1 on to CCD. Polarisers P2 and P3 are only inserted when B_0 or B_1 components need to be isolated.

Figure 2-10 shows the 1:1 image of the FIP. The high value of the ρ_0 value of 42.1 generates a sharp double ring structure with the Poggendorff ring clearly defined. The radial intensity profile Figure 2-11 compares excellently with theory.

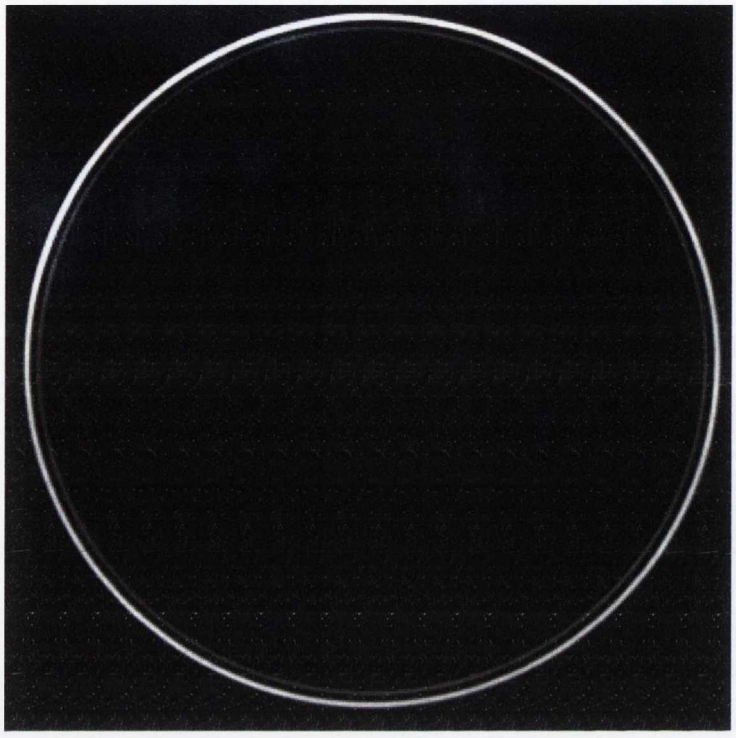

Figure 2-10: Focal image plane of a conical beam at Z = 0 with a $_0$ value of 42.1. Ring diameter of 1.18mm.

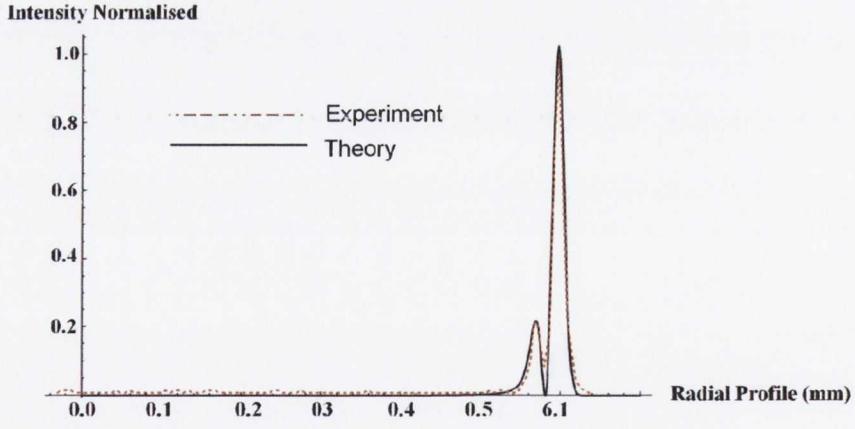

Figure 2-11: Radial intensity plots of Figure 2-10 FIP (Z = 0) of the conical beam (red-dashed) compared to theory (black-solid).

Close inspection of Eq. (2.26) shows that the B_0 field retains the polarisation of the incident beam, while the matrix $M(\theta_p)$ transforms the polarisation of the B_1 field to be orthogonal to the B_0 beam. Using Eq. (2.26) the polarisation of the two generated beams are mapped out to show their distribution around R_0, Figure 2-12. The vector addition of the beams results in the rotation of the position of maximum intensity over a wavelength. If the light is circularly polarised the polarisation distribution of the fields B_0 and B_1 are mutually orthogonal at all points around R_0, as Figure 2-12(a) depicted. If the incident light is circularly polarised the $M(\theta_p)$ reduces along to $e^{+(-)i\theta}$ depending upon the handedness of the incident polarisation. This introduces a 2π variation of phase around the beam axis. This phase term is indicative of the presence of a helical wavefront in the form of an optical vortex and the presence of orbital angular momentum; this is the subject of Chapter 2. Only when the incident field is circularly polarised are the separate conical beam components B_0 and B_1 mutually orthogonal at all points around R_0. However if the incident light is linearly polarised there is a gradient of intensity around the ring. The point of maximum intensity corresponds to the position on the wave-surface for corresponding to that polarisation, with the point of zero intensity corresponding to the diametrically opposed point on the ring with orthogonal polarisation, Figure 2-12(b).

Figure 2-13 shows the electric field amplitudes Eq. (2.27) and Eq.(2.28) for a circularly polarised incident beam. Both B_0 and B_1 show a change of phase across the Poggendorff ring at $R = R_0$. The B_1 component Figure 2-13(b) shows an extra phase change at $R = 0$, indicating a 2π phase change across the beam axis. The combined electric field as per Eq. (2.26) shows a half phase change around the beam axis, Figure 2-13(c).

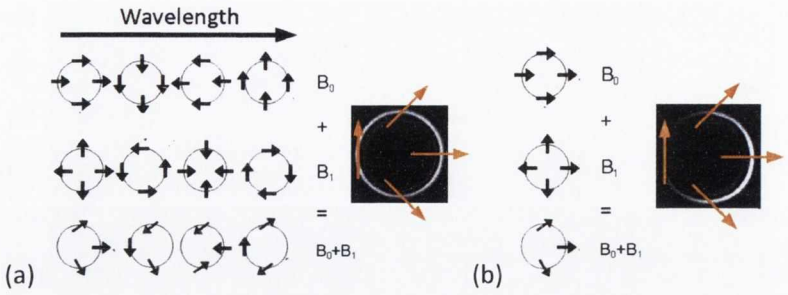

Figure 2-12: Distribution of polarisation vectors around the B_0 and B_1 beams with combined superimposed beams. (a) Left circular incident light. (b) Horizontal linear polarisation. Note this is for one ring.

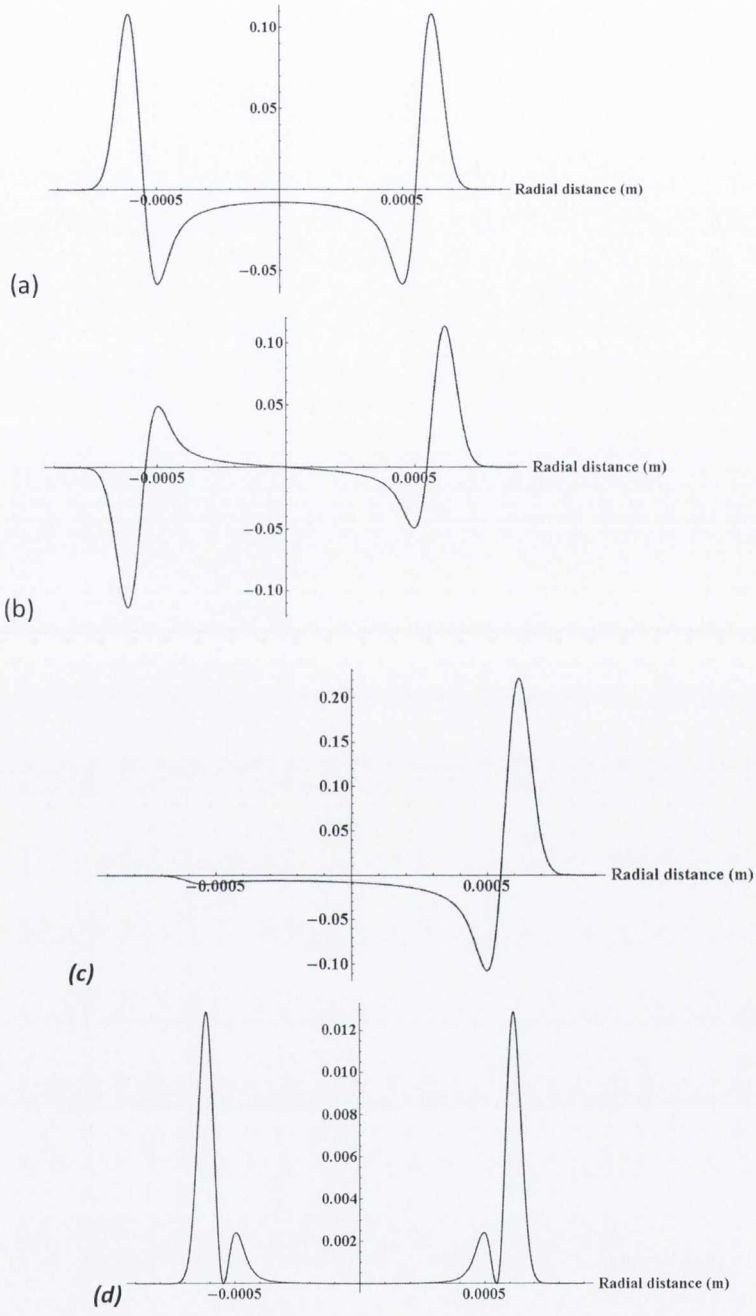

Figure 2-13: Theoretical radial electric field plots for (a) B_0 component, (b) B_1 component, (c) B_0+ B_1 field combined. (c) Radial intensity plot of a conical beam.

Figure 2-14 shows the propagation of the electric field along the z in the x-y plane for a beam waist size of 14 μm. The B_0+B_1 electric field show a π phase across the beam axis as the beam propagates the field. Figure 2-14(c) shows the diffraction of the electric field as the beam propagates. The left hand side of B_0 is of opposite phase to the B_1 field resulting in a cancellation of the electric fields with B_0 when in superposition. The corresponding intensity profiles for Figure 2-14 are presented in Figure 2-15. The B_0 component Figure 2-15(a), which is a double ring of azimuthally uniform intensity and phase yields a zero-order Bessel beam in the far-field. However, due to the azimuthal variation of phase in the B_1 component, it yields a first-order Bessel beam, which has zero intensity on axis as shown in Figure 2-15(b). Taking both beams in superposition yields the beams diffracted into the far field around x-y plane forming what is known as the axial spike, Figure 2-15 (c).

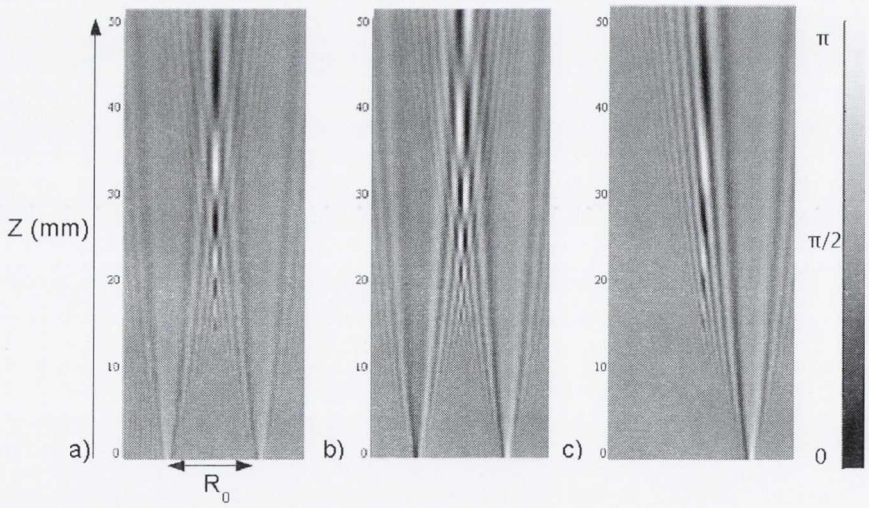

Figure 2-14: Simulated electric distributions in the x-y plane for the diffraction of the conical beams away from the FIP (Z = 0) position. (a) B_0, (b) B_1 and (c) B_0 + B_1 field.

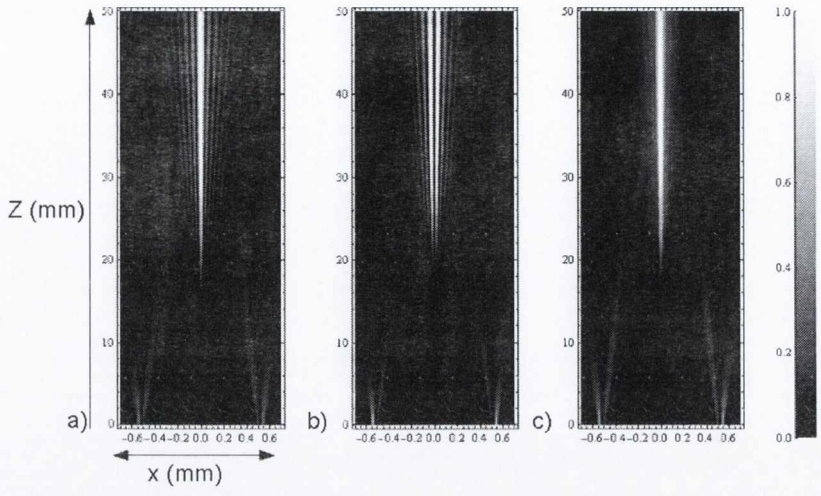

Figure 2-15: Corresponding simulated intensity distributions of Figure 2-14 in the x-y plane for the diffraction of the conical beams away from the FIP (Z = 0) position. (a) B_0 (b) B_1 and (c) $B_0 + B_1$ field.

Figure 2-15Figure shows the simulated intensity profiles along the z-axis away from the FIP in the x-y plane. The B_0 component Figure 2-15(a), which is a double ring of azimuthally uniform intensity and phase yields a zero-order Bessel beam in the far-field. However, due to azimuthal variation of phase in the B_1 component, it yields a first-order Bessel beam, which has zero intensity on axis, as shown in Figure 2-15(b).

The B_0 and B_1 field components can be isolated using a λ/4 plate (P2) and linear polariser positioned combination after the crystal, to transform the orthogonal circular polarisation states into orthogonal linearly polarised states using P2 and selecting either linear state with P3. Setting the fast axis of P1 parallel to P2 enables the linear polariser P3 to select the B_0 by blocking the polarisation in the horizontal plane and vice versa to block the B_1 component. The experimental intensity profile images from the Z = 22 cm plane for the conical beam are presented in Figure 2-16(a) for the B_0 profile, Figure 2-16(b) for the B_1 profile and Figure 2-16(c) for the B_0 + B1 profile. A comparison of the

radial intensity profiles of Figure 2-16 with Eq. (2.26) are presented in Figure 2-17 and compare favourably with theory.

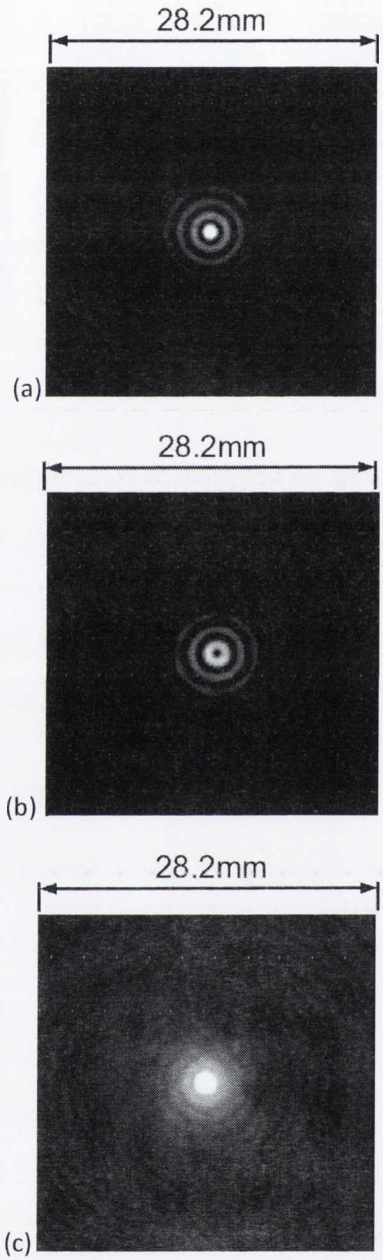

Figure 2-16: Experimental images of (a) B_0 field, (b) B_1 field, (c) Axial spike B_0 +B_1 field.

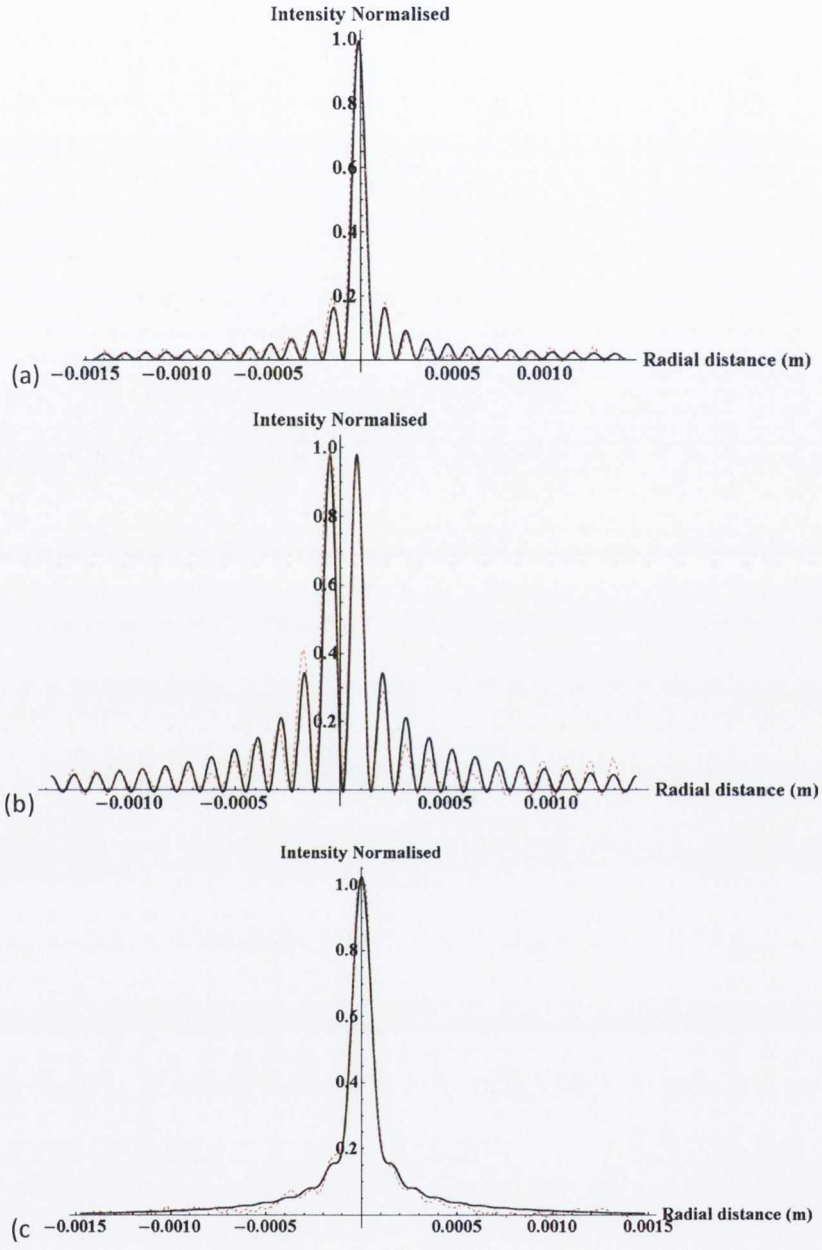

Figure 2-17: Radial intensity profiles of profiles in Figure 2-16 (red-dashed) compared with theory (black- solid) for (a) B_0 ,(b) B_1 (c) B_0+B_1cases

Alternatively, the FIP can be directly imaged using a lens with a focal length that is greater than the length of the biaxial crystal used, negating the requirement for an imaging lens. As a result the beam waist (w) will be greater and the ρ_0 will decrease. Figure 2-18 shows the simplified arrangement for the direct imaging of the FIP using a single lens. The L_1 with a focal length of 22cm forms a $1/e^2$ beam waist of 0.1mm, giving a ρ_0 5.9. The corresponding FIP and radial profile are presented in Figure 2-19, showing again excellent correlation. Finally if the lens L1 is removed and the laser is directed thought the crystal with a $1/e^2$ beam waist of 0.8 mm giving a ρ_0 0.7. Examining the B_1 intensity distribution as pre Figure 2-20, shows zero intensity on axis with a radially smooth intensity distribution. The position of the point of zero amplitude corresponds to the direction of the binormal to the wave surface. This intensity profile closely resembles that of a first-order Laguerre Gaussian mode.

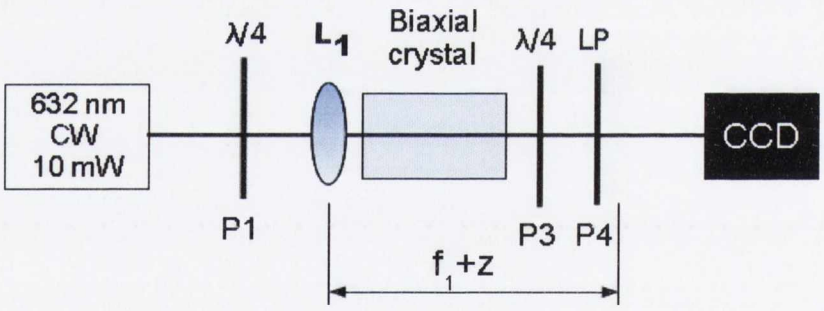

Figure 2-18: Experimental setup for the direct imaging of the FIP.

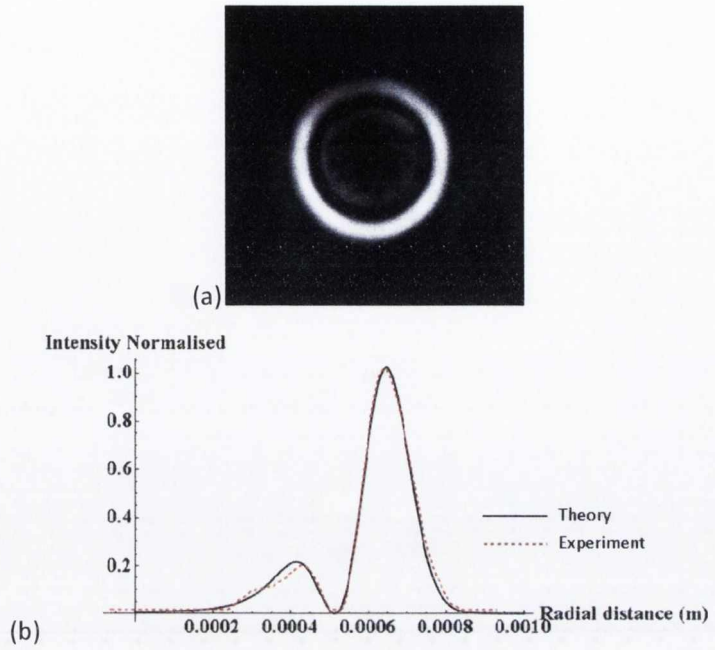

Figure 2-19: Experimental image of FIP w = .1mm (b) Radial intensity profile and theoretical fit

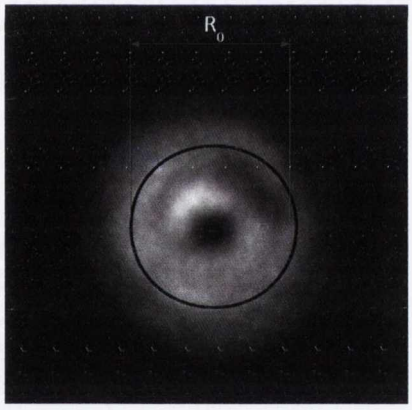

Figure 2-20: FIP B_1 field for ρ_0<1 showing the zero intensity at the centre of the beam axis corresponding to the direction of the binormal.

2.4 Conclusions

To conclude, this chapter contains the geometric theory of Hamilton's prediction of internal conical refraction (ICR). Internal conical diffraction (ICD) expands the geometric theory in to a full paraxial wave theory using the methodology developed by Berry. This enables the calculation of the electric field and intensity profile of the conical beam at any point in space. Using this transformation, a paraxial Gaussian beam is converted into two orthogonally polarised electric fields, whose radial electric field profiles are described by Bessel functions of zero and first-order. The zero-order beam retains the incident polarisation structure, while the first-order beam is orthogonally polarised and contains a 2π phase variation around the beam axis. The experimental transformation of a circularly polarised Gaussian beam in the FIP and in the far field compared excellently with theory.

2.5 References

1 L. Landau and E. M. Lifshitz, *Electrodynamics of Continuous Media*. (1984).

2 R. W. Ditchburn, *Light*. (Academic Press, London, 1975).

3 J.C. Poggendorff, "Ueber die konische Refraction,," Pogg. Ann. **124** (11), 461-462 (1839).

4 R. Potter, "An examination of the phaenomena of conical refraction in biaxial crystals," Philosophical Magazine. **18** (343-353) (1841).

5 W. Voigt, "Bemerkungen zur Theorie der konischen Refraktion," Annalen der Physik **324** (1), 14-21 (1906).

6 M. Born and E. Wolf, "Principles of Optics," (1959).

7 C. Raman, V. Rajagopalan, and T. Nedungadi, "Conical refraction in naphthalene crystals," Proceedings Mathematical Sciences **14** (3), 221-227 (1941).

8 E. Laylor, "An Analytical Approach to the Theory of Internal Conical Refraction," Journal of Mathematical Physics **13**, 449-454 (1972).

9 A. J. Schell and N. Bloembergen, "Laser studies of internal conical diffraction. I. Quantitative comparison of experimental and theoretical conical intensity distribution in aragonite," Journal of the Optical Society of America A **68** (8), 1093 (1978).

10 D. L. Portigal and E. Burstein, "Effect of Optical Activity or Faraday Rotation on Internal Conical Refraction," Journal of the Optical. Society of America **62** (7), 859-864 (1972).

11 A. M. Belskii and A. P. Khapalyuk, "Propagation of confined light beams along the beam axes (axes of single ray velocity) of biaxial crystals," Optical Spectroscopy (USSR) **44**, 312 (1978).

12 A. M. Belskii and A. P. Khapalyuk, "Internal conical refraction of bounded light beams in biaxial crystals," Optical Spectroscopy (USSR) **44**, 436 (1978).

13 M. V. Berry, "Paraxial beams of spinning light," SPIE Optical Engineering Press **3487**, 6-13 (1998).

14 M. V. Berry, "Conical diffraction asymptotics: fine structure of Poggendorff rings and axial spike," Journal of Optics A, **6** (4), 289 (2004).

15 M. V. Berry, M. R. Jeffery, and J. G. Lunney, "Conical diffraction: Observations and theory," Proceedings of the Royal Society A, **462** (2070), 1629-1642 (2006).

16 M. V. Berry and M. J. Jeffrey, "Conical diffraction: Hamilton's diabolical point at the heart of crystal optics," Progress in Optics (50), 13-50 (2007).

17 M. C. Pujol, M. Rico, C. Zaldo, R. Solé, V. Nikolov, X. Solans, M. Aguiló, and F. Díaz, "Crystalline structure and optical spectroscopy of Er3+-doped $KGd(WO_4)_2$ single crystals," Applied Physics B: Lasers and Optics **68** (2), 187-197 (1999).

Chapter 3

SPIN TO ORBITAL ANGULAR MOMENTUM CONVERSION USING INTERNAL CONICAL DIFFRACTION

3.1 Abstract

The transformation of spin angular momentum in the form of polarisation into an orbital angular momentum in the form of an optical vortex via ICD is discussed. Circularly polarised light with a maximum SAM of ±1ħ is converted into a superposition of orthogonally polarised Bessel like beams, B_0 with $\ell = 0$ and B_1 with $\ell = \pm 1$ also retaining the incident SAM helicity. This superposition results in a net pure OAM state of ½ħ per photon. The conversion of SAM to OAM using elliptically polarised light in the B_1 field component is discussed and experimentally presented. ICD provides a means to actively tune and select any non-integer OAM state up to ±1ħ using just polarisation optics. The main results of this chapter resulted in the publication,

"Generation of continuously tunable fractional optical orbital angular momentum using internal conical diffraction," D. P. O'Dwyer, C. F. Phelan, Y. P. Rakovich, P. R. Eastham, J. G. Lunney, and J. F. Donegan, Optics Express ***18*** *(16), 16480-16485 (2010).*

3.2 Introduction

When an object is in motion it possesses momentum, for motion in a straight line the velocity of the object multiplied by its mass gives the momentum. An object in circular motion around a fixed point possesses angular momentum, the linear momentum multiplied by the radius of the circle. Angular momentum may possess both spin and orbital components. The same applies for a photon, Maxwell's theory states that electromagnetic radiation carries both energy and momentum[2]. Radiation may have both linear and angular momentum[3]. In general, a light beam may have both spin angular (SAM) and orbital angular momentum (OAM) components. These two distinct (albeit only realistically separable in the paraxial regime[4]) angular momentum components are required for the complete understanding of the classical and quantum mechanical nature of light.

The angular momentum properties of photons was first demonstrated by Beth [5] by showing that circularly polarised light exerts a torque on a freely suspended half wave-plate. Quantum mechanically a photon has a SAM of either left (+1ħ) or (-1ħ) right per photon. The polarisation and hence SAM of a beam of light is easily modified via a quarter wave-plate.

The generation and control of the OAM component of light is not as easily achieved and requires a new set of optical tools. The generation of OAM requires the introduction of an azimuthal phase component into the electric field. Experimentally this is most commonly realised via the generation of higher order Gaussian modes known as Laguerre-Gaussian beams. These beams are characterised by the presence of a helical phase structure of complex phase denoted by $e^{i\theta\ell}$, where the integer ℓ denotes the number of 2π variations of phase around the beam axis over one wavelength, which under the right conditions carry OAM of $\ell\hbar$ per photon[6-9].

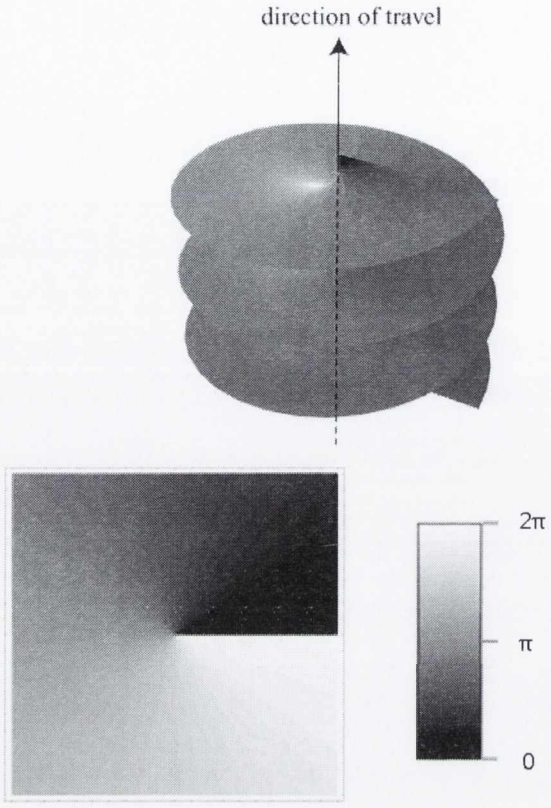

Figure 3-1: Helical wavefront of a beam with OA M with accompanying phase profile. Phase rotates from 0 to 2π over a wavelength with a point of zero amplitude at the centre of the beam.

The OAM of light is often associated with the presence of an optical vortex. shows the helical phase profile of an optical vortex, where the phase varises from 0 to 2π around the direction of propagation. The helical wavefront is a result of the Poynting vector (**S**), which is perpendicular to the wavefront is not parallel with the direction of propagation of the beam. These optical vortices are restricted to be integer valued as the phase rotation must be continuous around a fixed point of zero amplitude, known as optical singularities [10]. As for SAM, the OAM for a single photon is quantized. It has been shown experimentally that at the single photon level spin angular momentum could be added to or subtracted from the orbital component, confirming that the optical angular momentum of a light beam is $(\ell+\sigma)\ \hbar$ per

photon, where ℓ is an integer and $\sigma = \pm 1$ [11]. In general, any beam with inclined phase fronts carries OAM about the beam axis which, when integrated over the whole beam can be an integer on non-integer multiples of $\hbar$ per photon [12]. The OAM of a beam of light or an ensemble of photons can be of any integer or non-integer value, achieved via the superposition of integer valued OAM states of differing optical power. The resulting net OAM gives the expectation value per photon of the field. This increased dimensionality that OAM of photons provides opens the possibility for use in quantum information processing where entangled photons with OAM enable the transfer of much higher density of information per q-bit (bit of quantum information)[13]. This increased density is exploited in the fields of quantum encryption, cryptography and quantum information transfer. Such schemes have an intrinsic security as any attempt to intercept or eavesdrop changes the orbital angular momentum and angular position uncertainty principle [14].

Laboratory beams which possess this helical phase structure are generally generated via the illumination of numerous devices, such as computer generated holograms (CGH) [15-16], spiral phase plates (SPP)[17], spatial light modulator (SLM) or "Q-plates" with a normal Gaussian laser beam[18]. Spiral phase plates (SPP) are transparent dielectric heliocoidal shaped devices with a physical step edge. The step height introduces a dislocation to the wave front and a non-uniform delay in phase around the incident beam profile introducing a phase variation that is proportional to the step height. These devices are mechanically or thermally adjustable to introduce the required number of phase rotations[16]. Due to their step edge along the dislocation, there is a point in the centre of the device which causes a disruption to the transmitted beam which adversely affects beam mode quality[17].

Computer generated holograms (CHG) have the required phase profile generally in the form of a forked hologram (Figure 3-2), which imprints the required number of 2π phase steps around the beam axis[19].

The insertion of an extra fringe at the centre of the hologram insures that each diametrically opposed point is π out of phase with each other. Increasing the number of extra fringes increases the number of phase steps. While these devices provide the most cost effective means of generating OAM (phase patterns can be printed onto acetate sheets and placed directly into the optical setup), they do have diffraction related conversion problems. Spatial light modulators (SLM) are programmable LCD devices containing computer controlled refractive elements, light reflecting off its surface may have a phase delay programmed into it by a pixel with an appropriate phase delay[20]. Each pixel can be considered as a variable wave-plate. However, the device resolution is restricted to the pixel resolution of the device. Increasing the pixel density increases the price, much like their CCD counterparts. The fork gratings generated via CHG or SLM's are amplitude gratings, diffraction gratings with extra fringes present. This disperses the incident light into a large number of diffraction orders, and as a result these methods provide an inefficient means for generating a single mode[21].

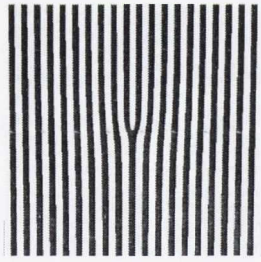

Figure 3-2: A fork hologram showing an extra phase dislocation generating a beam $\ell = 1$.

The conversion of SAM into OAM provides a means to generate and control the total angular momentum (AM) of light using all optical polarisation based devices. Such optical devices manipulate the polarisation of the light compared to the interaction of the AM with matter. In all the above methods, the phase profile is imprinted on the

generated wave front, whose orbital helicity is therefore fixed, although SLM's allow a slow dynamical control of the generated helicity, by changing the pixel information on the sensor. The ability to control the chirality and phase profile of the generated wavefront by just controlling the input polarisation handedness and ellipiticty provides the ability to control the generated OAM per photon using standard optical components.

One such device is a Q-plate; these are birefringent uniaxial liquid crystals, which convert SAM into OAM. Circularly polarised light with a SAM state of +1ħ upon propagation through such a plate is converted into an OAM state of +2ħ with high efficiency up to 98% but with low beam fidelity [18,22-23]. Light passing through such a Q-plate, has each photon converted from left-circular to right-circular changing its spin z-component angular momentum from +ħ to -ħ. The orbital z-component angular momentum of each photon changes instead from zero to 2 ħ. Therefore, the total variation of the angular momentum of light is nil, and there is no net transfer of angular momentum to the plate: The plate in this case acts only as a "coupler" of the two forms of optical angular momentum, allowing their conversion into each other. In this chapter the demonstration of a non-interferometric method for the control of the OAM per photon using polarisation optics and internal conical diffraction is described.

3.3 Angular momentum of light

In this section, the distinction between linear and angular momentum of light will be discussed, showing explicitly in the paraxial regime that the spin and orbital components can be separated into distinct local densities of the electric field as shown in [24]. Using the notation of chapter 2 from[24] the angular momentum of light can be described in terms of Maxwells equations. The linear momentum of a photon is given

by the wave-vector k = $(2\pi/\lambda)$ times $\hbar$. More formally, the cycle averaged linear momentum density is given by;

$$\mathbf{p} = \varepsilon_0 \mathbf{E} \times \mathbf{B}. \tag{3.1}$$

The angular momentum density of a transverse electromagnetic field is given by,

$$\mathbf{j} = \varepsilon_0 \mathbf{r} \times \langle \mathbf{E} \times \mathbf{B} \rangle, \tag{3.2}$$

where **E** is the electric field and **B** is the magnetic field. The total angular momentum (AM) is given by the integral of Eq. (3.2) over the entire field.

$$\mathbf{J} = \varepsilon_0 \int \mathbf{r} \times (\mathbf{E} \times \mathbf{B}) d\mathbf{r}. \tag{3.3}$$

$$\mathbf{J} = \int \mathbf{j} d\mathbf{r}, \tag{3.4}$$

Equation (3.3) can be separated out further such that a body rotating around a centre of mass has a radius of rotation given by r = **R**+**r'**, where **R** is the position of the centre of mass and **r'** is the position in the centre of mass system. When Eq. (3.4) is adjusted for this and integrated over position the total AM is now separable into two distinct components[25].

$$\mathbf{J} = \mathbf{L} + \mathbf{S}, \tag{3.5}$$

where **L** is the orbital component and **S** is the spin contribution. The **S** component is intrinsic in nature as the calculation point for the origin of the rotation is fixed. If we take **L** to be

$$\mathbf{L} = \mathbf{R} \times \mathbf{P}, \tag{3.6}$$

$$\mathbf{P} = \int \mathbf{p} d\mathbf{r}, \tag{3.7}$$

the **L** component depends of the centre of mass position defining an anchor point for **R** describing the point of origin for the calculation. This

position is not fixed so OAM can be either extrinsic or intrinsic In this case, the distinction between spin and orbital angular momentum is not well defined for a general quantum radiation field. However in the paraxial regime these AM components are distinct and separate [8,26-27].

The paraxial approximation as explained in on page 29, enables the separation of the distinct angular momentum component into *L* and *S* as shown in section 2.5 of [24].

$$L(\mathbf{R},\mathbf{z}) = \frac{\varepsilon_0}{i\omega}\mathbf{u}^* . \frac{\partial}{\partial\theta}\mathbf{u} + \mathbf{c.c.}, \tag{3.8}$$

$$S(\mathbf{R},\mathbf{z}) = -\frac{\sigma}{2\omega} R \frac{\partial}{\partial R}(\mathbf{u}^* \times \mathbf{u}). \tag{3.9}$$

One can see in Eq. (3.8) the L is determined by the phase gradient of the field **u** in the azimuthal direction (θ) this is the z-component of the orbital AM per photon. The S component arises from the radial derivative of the transverse field amplitude.

3.3.1. Polarisation - Spin angular momentum

The SAM component ($J_{sp} = \sigma\hbar$) is associated with the polarisation of the light, where the sign of σ denotes the chirality of the light. In the quantum description of light, the spin of a single photon is quantised to be in units of ħ per photon to be either pure left (+1ħ) or (-1ħ) right-circularly polarised light. A single photon cannot have a non-integer SAM value. Elliptical polarised light results in a non-integer SAM state, such a beam is composed of an ensemble of photons of opposite SAM states of differing amplitudes. Linear polarised light has a $J_{sp} = 0$, composed of a superposition of two beam of equal amplitude with ±1ħ photons

Classically one considers the polarisation of light as the variation of the orientation of the electric field as is propagates over a period of one oscillation. When the orientation remains constant and only the amplitude varies, the light is plane polarised, in effect **E** only oscillation in one plane. When the amplitude remains constant (over a cycle) the orientation of the vector must vary regularly such that the tip of the vector traces out a circle, and so the light is circularly polarised. The direction of rotation can be either counter/clockwise giving the respective rotation to be either left or right circularly polarised light. If both the amplitude and orientation vary such that the tip of the vector rotates around an ellipse the field is elliptically polarised.

Each of these representations can be resolved into two orthogonal electric field directions E_x and E_y. Varying the phase delay between each of these components with use of a quarter-wave-plate changes the time averaged position of the electric field **E**. When the phase delay is zero the field is linearly polarised and the plane of oscillation is the vector sum of the separate fields. When the phase delay is set to $\pi/2$, the field is circularly polarised and the field components oscillate out of phase and the resulting **E** field rotates symmetrically. The intermediate case is when there is an unequal division of amplitudes between E_x and E_y, the resultant tip of the **E** field will vary in amplitude and propagates tracing out an ellipse, and is elliptically polarised.

3.3.2. Jones matrix

The mathematical description of the electric field vectors of light that is most commonly used is the Jones vector. This terminology treats the electric field vector as a column vector describing the constituent E_x and E_y as the instantaneous scalar components of **E**. This enables any polarisation state to be described as a linear combination of the principal electric field vectors E_x and E_y,

$$\mathbf{E} = \begin{pmatrix} E_x(t) \\ E_y(t) \end{pmatrix} \tag{3.10}$$

A linearly polarised state has all of the amplitude of the electric field residing in one direction. For example, Eq. (3.11) shows horizontal linear polarisation where the horizontal is the x-axis. A left circularly polarised representation is shown in Eq.(3.12), where both directions are of equal amplitude with *i* representing a $\pi/2$ phase delay.

$$\mathbf{E} = \begin{pmatrix} 1 \\ 0 \end{pmatrix}, \tag{3.11}$$

$$\mathbf{E} = \begin{pmatrix} 1 \\ i \end{pmatrix}. \tag{3.12}$$

Eq. (3.13) represents a linearly polarised state of arbitrary orientation, the angle (α) represents the angle the electric field vector makes with the reference principal axis. Multiplying Eq. (3.13) through the corresponding transformation matrices for a quarter wave-plate, half wave-plate or linear polariser enables the representation of and polarisation state in this form.

$$\mathbf{E} = \begin{pmatrix} E_x \\ E_y \end{pmatrix} = \begin{pmatrix} \cos(\alpha) \\ \sin(\alpha) \end{pmatrix} \tag{3.13}$$

These Jones matrices are used in Section 2.5 to describe the polarisation of the conically diffracted beam as it propagates through the optical

system. There also exists Jones-like matrix operators for beams carrying OAM[28] where polarisation wave-plates are replaced by cylindrical mode converters or cylindrical lens, however they are not utilised in this study.

3.3.3. Quantum mechanical SAM

The spin component of angular momentum Eq. (3.9)is given by the gradient in the radial direction. This complex vector field **u**(**R**,z), can be rearranged in terms of the complex normalised local polarisation vector (**e**) and the local field strength, u =|**u**| such that the energy density of the beam directly depends on the helicity (σ) times the energy density (w) of the transverse position **R** such that,

$$2\varepsilon_0 \frac{(\mathbf{u}^* \times \mathbf{u})}{i} = w\sigma. \tag{3.14}$$

The helicity σ is;

$$\sigma = \frac{(\mathbf{e}^* \times \mathbf{e})}{i}. \tag{3.15}$$

The helicity is for circular rotation whose sign depends on the direction of the leading transverse vector **R**, denoted by the leading electric field vector in Eq.(3.16). This takes a maximum value of σ = ±1 for circular polarisation,

$$\mathbf{e}_{\pm} = \frac{(\mathbf{e}_x \pm \mathbf{e}_y)}{\sqrt{2}}. \tag{3.16}$$

The spin angular momentum in terms of photon density is given by nħσ for n photons or as ħσ per photon. The spin σħ is restricted to a maximum of ±1ħ per photon, where positive (clockwise) rotation corresponds to a negative SAM per photon. If the spin angular momentum of a single photon was measured with a detector it would only register integer values of the SAM. A non-integer (elliptical polarisation) σ state consists of the superposition of differing integer

states of differing amplitudes, generating a non-integer expectation value of the SAM per photon. Quantum mechanically this can still be valid if we measure the SAM of an ensemble of photons[24].

Experimentally a quarter-wave-plate is used to change the polarisation from linear through elliptical to circular, in effect changing the expectation value of the SAM. Combining Eqs.(3.13) and (3.16) the SAM expectation value can be determined as a function the angle (α) that linearly polarised light makes with the fast axis of a quarter wave-plate. When normalised it reduces to,

$$J_{sp} = \sigma\hbar = \hbar \frac{-i\left(E_x E_y^* - E_y E_x^*\right)}{\left|E_x^2\right| + \left|E_y^2\right|} = \hbar \sin(2\alpha) \tag{3.17}$$

One can see from Eq. (3.17) that the SAM (J_{sp}) varies as sin(2α). When α = 0° J_{sp} = 0ħ per photon. When α =±45° the linearly polarised light is converted into left/right circularly polarised light and J_{sp} = ±1ħ per photon.

3.3.4. Orbital angular momentum-optical vortices

The orbital component (L) Eq. (3.8) contains a derivative with respect to θ (the angle around the beam axis) of the electric field, which can otherwise be termed a phase gradient around the azimuthal angle, and is independent of the polarisation. In order for this component to be non-zero a beam profile must contain a complex phase component of the form $e^{i\theta\ell}$, ℓ must be integer valued.

$$A(R,\theta,z) = A_\ell(R,z)e^{i\ell\theta}. \tag{3.18}$$

An optical vortex of topological charge ℓ, is one in which the phase winds by 2πℓ on a closed path around the beam. Consequently, these

vortices are the eigen-modes of the differential operator $\partial/\partial\theta$. The number is always an integer, and can be positive or negative, depending on the handedness of the twist [10]. It should be noted however that presence of an optical vortex of topological charge ℓ is not indicative of a beam carrying an OAM of $\ell\hbar$ per photon. This only holds true for a scalar beam with an azimuthally uniform intensity distribution in which the variation of the spin and orbital angular momentum is smooth and continuous, as Berry has shown[4]. Like SAM, the OAM of a single photon can only be integer valued. A non-integer OAM value, like a non-integer SAM is the probability of an ensemble of photons with $\ell\hbar$ per photon.

The ability to actively tune and select any integer or non-integer OAM state has been the subject of recent research. The formation of a beam with a non-integer or fractional OAM state has been achieved using numerous combinations of the earlier mentioned devices. Spiral phase plates can have a step height tuned to be either integer or non-integer valued, generating a beam with a fractional phase step[16]. It has been shown by Berry and Leach that if the phase variation around the beam is not continuous, the beam is unstable upon propagation[29-30]. High order optical vortices $\ell>2$, the vortices disassociate and separate upon propagation.

The vortex structure of a beam with a non-integer OAM per photon is characterised by a string of integer strength vortices along the line of discontinuous phase. Similarly, with CHG or SLM's the formation of a beam with fractional OAM using a fractional phase step generates an unstable beam unsuitable for propagation longer than the Rayleigh length. The superposition of integer strength vortices, generated by any of the above methods, in an interformetric arrangement has been shown to provide an adjustable means of generating non-integer OAM. Simply varying the intensity between the different modes enables access to a non-integer expectation value of the OAM per photon. These

beams have been shown to have increased structural stability over SPP's by matching the Guoy phases of the superimposed beams[30-31].

For a paraxial beam, only the component of angular momentum along the optic axis will be significant. The orbital angular momentum is given by the local expectation value of the operator R×(−iħ∇), integrated over the transverse electric field of the beam. The spin angular momentum is given by the integral of the local expectation value of the operator σħ. Using the paraxial approximation, as derived by Berry[8,32], the constituent J_{orb} & J_{sp} components can be expressed as,

$$J_{orb} = \frac{\hbar \mathrm{Im} \iint dR E^{*} \bullet \partial_{\theta} E}{\iint dR E^{*} \bullet E}$$
$$J_{sp} = \frac{\hbar \mathrm{Im} \iint dR E^{*} \times E \bullet e_{z}}{\iint dR E^{*} \bullet E} \qquad (3.19)$$

where θ is the azimuthal angle around the beam axis. The total angular momentum per photon of a light beam is given by,

$$J_{tot} = J_{orb} + J_{sp} = \frac{\hbar \mathrm{Im} \iint dR (E^{*} \bullet \partial_{\theta} E + e_{z} \bullet E^{*} \times E)}{\iint dR E^{*} \bullet E} \qquad (3.20)$$

The total angular momentum of a photon is summation of the expectation value of each of the spin and orbital components.

3.3.5. Observation of a beam with an optical vortex

The intensity pattern of a beam carrying an optical vortex is generally azimuthally uniform in intensity with a point of zero amplitude at the centre of the beam. The azimuthal intensity pattern alone will not reveal the underlying phase profile or topological order of the vortex present.

The phase profile and vortex order can be extracted interferometrically via the interference with a reference wave with a known phase profile and field curvature. For this, there are two different interference arrangements: (a) collinear interference and (b) wedge interference. Collinear interference is the direct superposition of two different beams, where the beams are spatially superimposed along the same path. Generally, the reference arm is a Gaussian beam, with a surface of constant phase (modulo 2π). If two Gaussian beams with matching field curvatures are collinearly interfered the resulting intensity pattern will either be the sum of the intensities or the difference of the intensities. The resulting intensity pattern resembles a Newton's ring pattern, alternating rings of constructive and destructive interference. Replacing the sample arm with a beam with complex phase, the resulting intensity pattern will reveal a contour line of constant phase in the form of a spiral, the number of which reveals the number of 2π phase rotations.

Alternatively, when a wedge is introduced between the beams, the overlap only occurs over a small region of space. The resulting mismatch in propagation angle results in a fringe intensity pattern of parallel lines. Each successive fringe indicates a 2π phase jump between the overlapped beams. When both beams are of planar phase the resulting fringe pattern in the region of overlap is a series of parallel lines. When one of the arms contains an optical vortex the fringe patterns contains

an extra fringe, indicating an extra 2π phase step around the beam axis. The base of the extra fringe is a point of zero amplitude; this is the position of the optical singularity and the position of the centre of the vortex. The number of extra fringes present reveals the topological order of the vortex present. These wedge interference patterns are the inverse of the patterns a CHG or SLM imprints on to a incident beam, Figure 3-3 shows a $\ell = 1$ interference pattern/ CHG hologram. Increasing the number of extra fringes increases the topological order of the imprinted vortex[21,33-34].

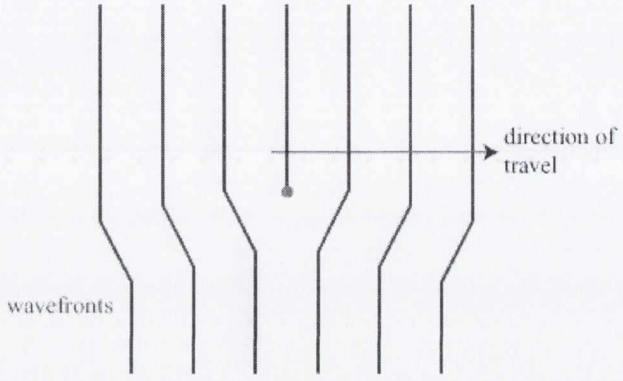

Figure 3-3: Wedged fringe profile showing the position of dislocation and position of the optical singularity of an optical vortex (blue spot).

3.4 Bessel beams

A key feature of the paraxial solution for ICD is the description of the radial amplitude in terms of Bessel functions J_n. This put ICD into the family of beams known as Bessel beams. These are a class of diffraction-less solutions of the Helmholtz differential wave equation in cylindrical polar coordinates using Bessel functions[35-36]. Bessel beams a superposition of plane waves with the wave vectors lying on the surface of a cone.

$$E(R,\theta,z) = A_0 \, e^{ik_z z} \, J_n(k_r, R) e^{\pm in\theta} \qquad (3.21)$$

where, ad r, z are the radial longitudinal and azimuthal components and θ is the azimuthal angle, k_z and k_r and the azimuthal and radial wave vectors. Comparing Eq. (3.21) to (2.27) and (2.28) one can see that the ICD beam components are of the same kind and should share much of the same properties. The radial profile of such beams depends upon the order of the Bessel function from Eq.(3.21). A zero order Bessel profile as shown in Figure 3-4, is characterised by a maximum peak of intensity on axis, with a transverse profile of concentric rings with a Bessel function periodicity and a π phase change between alternating rings. Each of the rings contains the same optical power as the central peak. Higher order Bessel beams n > 1, are characterised by a zero point of intensity on axis with a ring periodicity pertaining to the order of the Bessel function used. The higher order Bessel beams also contain an n2π phase change around the ring due to the presence of the $e^{\pm in\theta}$ phase term. These beams as already mentioned are associated with the orbital angular momentum of light and possess a helical wave front structure [37].

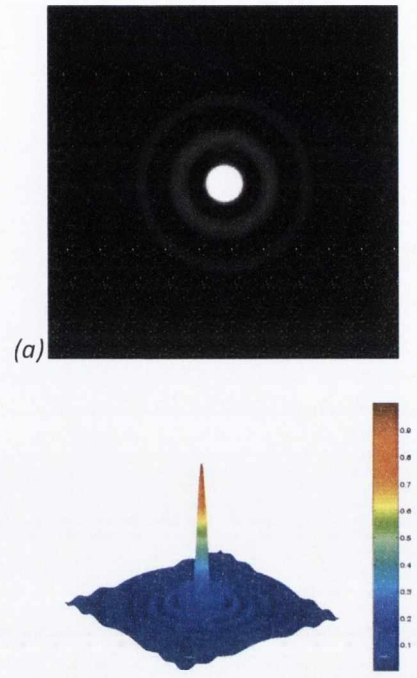

Figure 3-4: (a) Theoretical intensity profile of a zero order Bessel beam. (b) 3-D intensity profile.

3.4.1. Formation of Bessel beams

Bessel beams are of particular importance because of their low-divergence and self repair properties. Bessel beams are non-diffracting in the sense that the central core (or lack thereof for higher order mode) does not spread as it propagates. In reality Bessel beams may be non-diverging over many times the Rayleigh length of an equivalent Gaussian beam. Bessel beams can be generated using a conical lens known as an axicon[20,38-40] or an annular slit and lens combination[41-42].

The method used by Durnin involved a narrow annular (circular) slit with a converging lens placed at its focal length away from the slit. This forms near the focal length of the lens giving the beam a low divergence. A zero order Bessel beam can be considered a Fourier transform of a ring of constant phase and intensity. A conical lens

known as an axicon may be used to form a Bessel beam[20]. These are optical elements that focus light such that the transformed wave vectors lie on the surface of a cone given by the cone angle of the lens.

Bessel beams (BB) are widely utilised in optical trapping where the periodic ring structure and non-diverging region can be used to optically sort and stack micron-sized particles. The reconstruction properties of Bessel beams also provide an advantage over standard Gaussian traps. The increased depth of field enables the stacking of particles along the beam path but the Bessel beam also reconstructs around the particle [37,43]. Highly focussed Gaussian beams diverge very quickly and as a result the optical forces on a particle fall off quite rapidly, limiting trapped particles to be around the focus.

They are also used in non-linear optics and spectroscopy due to the strong peak intensity distribution ranging over long distances. Laser material processing, such as two photon polymerisation also exploit the high intensity non-diverging core to create micron sized optical trenches and pillars due the greater depth penetration of the core over an equivalent Gaussian beam[44].

3.4.2. Higher order Bessel beams

A higher order Bessel beam given by Eq. (3.21)with n>1, can have the azimuthal phase factor (R) decomposed into Cartesian coordinates such that x = cos(R) and y = sin(R). As Soares described in [45], the use recurrence relation of Bessel functions when n = ±1 Eq. (3.22) can be expressed as,

$$BB_{\pm 1}(z,R,\theta) = \pm\frac{k_r}{2}e^{ik_z z}\left\{\left[J_0(k_r R)+J_1(k_r R)\right]x \pm i\left[J_0(k_r R)+J_1(k_r R)\right]y\right\}. \quad (3.22)$$

Noting that the Hermite polynomial identities $H_{10}(x)$ and $H_{02}(y)$, which are solutions to the Helmholtz equation in Cartesian coordinates are of the form,

$$HB_{10} = \left[J_0(k_r R) + J_1(k_r R)\right] H_1(x) H_0(y)$$
$$HB_{01} = \left[J_0(k_r R) + J_1(k_r R)\right] H_0(x) H_1(y) \tag{3.23}$$

This enables Eq. (3.22)to be now written as

$$BB_1 = k_r e^{ik_z z}\left(HB_{10} + iHB_{01}\right)$$
$$BB_{-1} = -k_r e^{ik_z z}\left(HB_{01} + iHB_{10}\right) \tag{3.24}$$

This shows that a first-order Bessel beam can be expressed as a superposition of orthogonal Hermite-Bessel (HB) modes with a $\pi/2$ phase delay. Switching the phase delay to be either + $\pi/2$ or - $\pi/2$ will switch the chirality of the phase rotation and consequently the OAM of the Bessel beam. These beams are analogous to circular polarisation, which can be described as a superposition of orthogonal linear polarisations with a $\pi/2$ phase delay.

(a) 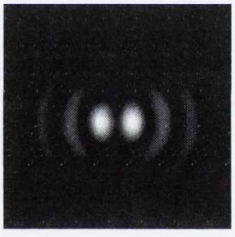 (b) 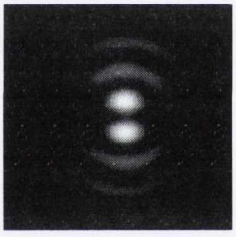

Figure 3-5: Hermite Bessel profiles (a) HB_{10} and (b) HB_0.

3.5 Conical diffraction SAM to OAM conversion

In this section, the experimental conversion of SAM to OAM under the conditions of internal conical diffraction is experimentally described and discussed. Chapter 2 described the polarisation dependence on the intensity distribution of the conically diffracted beam was explained in terms of the superposition of orthogonally polarised zero (B_0) and first-order (B_1) Bessel like beams. The zero-order profile retains the incident

polarisation and phase structure, while the first-order beam is orthogonally polarised with a phase change around the beam axis. This complex phase structure is associated with the presence of OAM and under the correct conditions an optical vortex.

The OAM per photon of the entire conically diffracted beam was calculated by Berry [46] to be a purely OAM state of half the incident SAM per photon.

$$J_{orb} = \frac{J_{sp}}{2}\hbar. \tag{3.25}$$

So when the incident field is circularly polarised with a J_{sp} = 1ħ per photon the resultant OAM per photon is ½ ħ per photon. This fractional OAM state is composed of the integer vortex state in the B_1 component and a non-OAM state from the B_0 field component. The fractional OAM of the composite conical beam is a result of a superposition of integer strength beams giving a non-integer OAM expectation value. The generation of a fractional strength vortex is very unstable, and quickly decomposes into separate integer valued vortices. A radial dislocation line of zero amplitude indicates the presence a fraction phase step around the beam axis (i.e. between 0 and 2π). As predicted by Berry the dislocation line contains a string of low amplitude vortices of alternating helicity to compensate for the fractional phase step. The OAM per photon is still quantised; an optical vortex is born when the net OAM per photon is above ½ ħ.

The conversion of circular polarisation into a superposition of OAM states of differing order was also experimentally performed by King using circularly polarised Bessel beams of zero order [47].

3.5.1. Experimental observation of spin to orbital angular momentum in conical diffraction

In this section, the conversion of SAM for an arbitrarily polarised Gaussian beam into a corresponding pure OAM state is presented. Chapter 2 outlined the generation separation of the orthogonally polarised conically diffracted beam modes, described by Bessel functions of zero- and first-order. The first-order beam component contains a phase change around the ring, giving rise to the OAM. The following details the isolation of the first-order beam component that is mutually orthogonal to the incident polarisation using Jones matrices.

Linearly polarised light, polarised in an arbitrary plane is incident upon a quarter wave-plates, where (α) is the angle the polarised light makes with the wave-plate fast axis.

$$\begin{pmatrix} 1 & 0 \\ 0 & i \end{pmatrix}\begin{pmatrix} \cos\alpha \\ \sin\alpha \end{pmatrix}=\begin{pmatrix} \cos\alpha \\ i\sin\alpha \end{pmatrix}. \tag{3.26}$$

Circularly polarised light now undergoes ICD transformation according to Eq. 2.21:

$$\mathbf{E}(\mathbf{R},z)=B_0\begin{pmatrix} \cos\alpha \\ i\sin\alpha \end{pmatrix}+B_1\begin{pmatrix} \cos\theta & \sin\theta \\ \sin\theta & -\cos\theta \end{pmatrix}\begin{pmatrix} \cos\alpha \\ i\sin\alpha \end{pmatrix} \tag{3.27}$$

A quarter wave-plate positioned after the crystal is set orthogonal to the quarter wave-plate before the crystal in Eq(3.26).

$$\begin{aligned}&\begin{pmatrix} 1 & 0 \\ 0 & -i \end{pmatrix}[B_0\begin{pmatrix} \cos\alpha \\ i\sin\alpha \end{pmatrix}+B_1\begin{pmatrix} \cos\theta & \sin\theta \\ \sin\theta & -\cos\theta \end{pmatrix}\begin{pmatrix} \cos\alpha \\ i\sin\alpha \end{pmatrix}] \\ &=B_0\begin{pmatrix} \cos\alpha \\ \sin\alpha \end{pmatrix}+B_1\begin{pmatrix} \cos\theta\cos\alpha & \sin\theta\sin\alpha \\ -i\cos\alpha\sin\theta & +i\cos\theta\sin\alpha \end{pmatrix},\end{aligned} \tag{3.28}$$

A linear polariser transmission axis is set such that $\beta = \alpha+90^0$ to remove the polarisation component corresponding to the incident polarisation,

$$\begin{pmatrix} \cos^2\beta & \sin\beta\cos\beta \\ \sin\beta\cos\beta & \sin^2\beta \end{pmatrix} B_1 \begin{pmatrix} \cos\theta\cos\alpha & \sin\theta\sin\alpha \\ -i\cos\alpha\sin\theta & +i\cos\theta\sin\alpha \end{pmatrix}. \quad (3.29)$$

This reduces to,

$$\mathbf{E}(\mathbf{R},z) = B_1[\cos\theta\sin 2\alpha + i\sin\theta]\begin{pmatrix} \sin\alpha \\ -\cos\alpha \end{pmatrix}. \quad (3.30)$$

When $\alpha = 0^0$ Eq. (3.30) reduces to Eq(3.31). This beam is described by a sinusoidal phase modulation, with a line of zero amplitude in the direction corresponding to the incident polarisation direction, which corresponds to $\alpha = 0^0$,

$$\mathbf{E}(\mathbf{R},z) = B_1[-i\sin\theta\begin{pmatrix} \sin\alpha \\ -\cos\alpha \end{pmatrix}]. \quad (3.31)$$

When $\alpha = 45^0$ Eq. (3.30)reduces to Eq. (3.32) as an optical vortex of same handedness as the incident circular polarisation, and is of the same form as Eq. (3.18)containing an optical vortex with an OAM of +1ħ per photon,

$$\mathbf{E}(\mathbf{R},z) = B_1[e^{i\theta}\begin{pmatrix} \sin\alpha \\ -\cos\alpha \end{pmatrix}]. \quad (3.32)$$

If the handedness of the polarisation is reversed by setting $\alpha = -45^0$ then Eq. (3.30) flips becoming,

$$\mathbf{E}(\mathbf{R},z) = B_1[e^{-i\theta}\begin{pmatrix} \sin\alpha \\ -\cos\alpha \end{pmatrix}]. \quad (3.33)$$

The linearly polarised case of Eq. (3.30)shows the SAM component to be zero. Applying Eq. (3.20) to (3.30) yields the dependence of the OAM on wave-plate angle α (incident SAM J_{sp}):

$$J_{orb} = \hbar \frac{2\sin(2\alpha)}{\sin^2(2\alpha)+1} = \hbar J_{sp} \frac{2}{\sin^2(2\alpha)+1} \qquad (3.34)$$

The OAM per photon of the B_1 field generated via ICD can now be calculated and controlled as a function of wave-plate angle (α)[1]. The entire conical beam (B_0+B_1) the generated OAM depends directly on the incident SAM where the net OAM per photon is $J_{sp}/2$.

3.6 Experimental details and methods

The experimental arrangement was set up as in Figure 3-6. A 10 mW 632 nm Gaussian laser beam linearly polarised in the horizontal plane was focused using a 5 cm lens (L1) to a beam waist size of 52 μm and directed along the optic axis of a 3 cm slab of the biaxial crystal $KGd(WO_4)_2$. At 632 nm the refractive indices are: n_1 = 2.01169, n_2 = 2.042198 and n_3 = 2.09510 [48], giving R_0 = 5.9×10^{-4} m and $\rho_0 = R_0/w = AL/w$ =11.3. The λ/2 plate rotates the plane of polarisation relative to the fast axis of the λ/4 plate (P1) which was also oriented in the horizontal plane. The biaxial crystal is oriented such that the plane containing the two optic axes also lies in the horizontal plane. The field orthogonal to the incident polarisation is selected via the orientation of the λ/4 plate (P2) and linear polariser positioned after the crystal. The fast axis of wave-plate P2 is oriented so that it is orthogonal to the fast axis of P1 and the output linear polariser (LP) was rotated so that it is always orthogonal to the linear polarisation incident on P1. If α is the angle of the input linear polarisation relative to the fast axis of P1, then the polarisation of the light incident on the crystal changes from linear for $\alpha = 0^0$, through elliptical, to left-circular for $\alpha = +45^0$, with a SAM of σ = +1ħ. Eq. (3.17) shows that this changes the SAM incident on the crystal from 0 to 1ħ per photon. The optical setup also included a Mach-Zehnder interferometer to examine the phase distribution of the output

beam as the polarisation into the crystal was changed. The polarisation of Gaussian reference arm is rotated 90^0 so that it has the same polarisation as the output beam.

The intensity distributions and fringe patterns were recorded using a CCD camera. The camera is in the far-field region of the conical diffracted beam, situated 35 cm away from the FIP position in the region where the FIP has diffracted to into the far field.

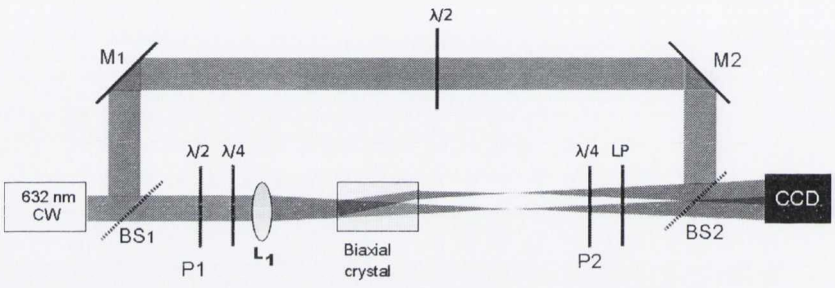

Figure 3-6: Experimental setup. BS: 50/50 beam splitters, M: broadband dielectric mirror, L1: 5 cm lens, LP: linear polariser, CCD: camera.

3.6.1.Results

The measured intensity distributions for the collinear and wedge interference patterns for $\alpha = 45^0$, together with their simulations of the same for both are shown in Figure 3-7 for B_o, and Figure 3-8 for the B_1 beam components. Figure 3-7 (a) shows the experimental (a-i) and simulated (a-ii) intensity profiles of the zero order mode. The collinear interference images Figure 3-7 (b) show a constructive and destructive interference patters between each of the consecutive rings as a result of each ring being of alternate phase. The wedge interference pattern Figure 3-7 (c) shows a series of parallel interference fringes. Consequently, the zero order beam is of planar phase with zero OAM per photon.

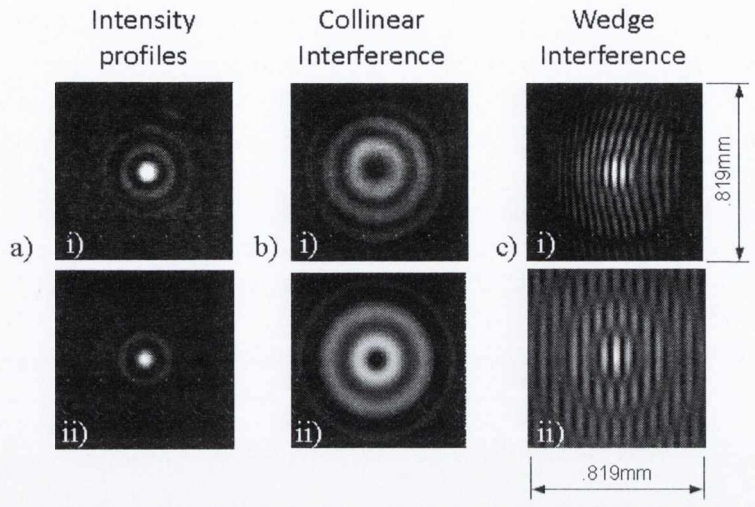

Figure 3-7: Experimental and simulations using Mathematica. (i) zero order beam profile, (ii) Collinear interference with a Gaussian beam, (iii) wedge interference with Gaussian mode. (iv-vi) Simulation of (i-iii).

Figure 3-8 (a-c) shows the experimental (a-i) and simulated (a-ii) intensity profiles of the first-order mode. The first-order mode contains the characteristic point of zero intensity at the centre of the beam profile and an azimuthally smooth intensity profile around each of the rings. Figure 3-8(b) shows the collinear interference image for (i) experimental and (ii) simulated profiles. The counter clockwise interference pattern shows the spiralling path of constant phase around the beam axis indicative of the presence of a $\ell = +1$ vortex. Figure 3-8(c) shows the wedge interference patterns for (i) experimental and (ii) simulated profiles. Close inspection reveals the presence of an extra fringe at the centre of the beam profile to the top of the singularity. The extra fringe reveals the presence of a 2π phase jump around the beam axis, indicating the presence of a continuous 2π winding of the phase and the presence of a non-zero OAM per photon.

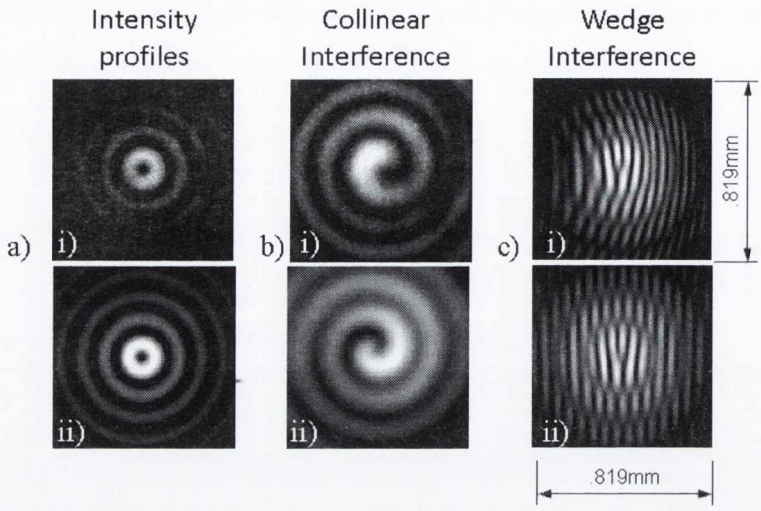

Figure 3-8: Experimental (i) and Mathematica simulations (ii) of the first-order conical beam profiles for, (a) intensity profile, (b) collinear interference with a Gaussian of planar phase, (c) wedge interference with a Gaussian of planar phase.

Figure 3-9 (a-c) shows the experimental (i) and Mathematica simulations (ii) intensity profiles for $\alpha = 0^0$. The intensity profiles are known as Hermite-Bessel beams with a sinusoidal modulation of intensity around the azimuth. The line of zero amplitude known as a dislocation line is a shear dislocation of phase along the plane of the incident polarisation. The interference images Figure 3-9 (b-c) show a π phase shift across the dislocation line. This is most notably seen in Figure 3-9(b) where the two central lobes interfering with the Gaussian destructively or constructively interfere on the opposite lobes. These patterns show the sinusoidal electric field amplitude distribution along the direction perpendicular to the incident polarisation (in accordance with Eq.(3.31)), along with a shear dislocation of phase along the plane of the incident polarisation. The collinear interference patterns show that there is no spiralling phase. The wedge interference shows no phase step, indicating that there is no complex phase distribution or optical vortex present.

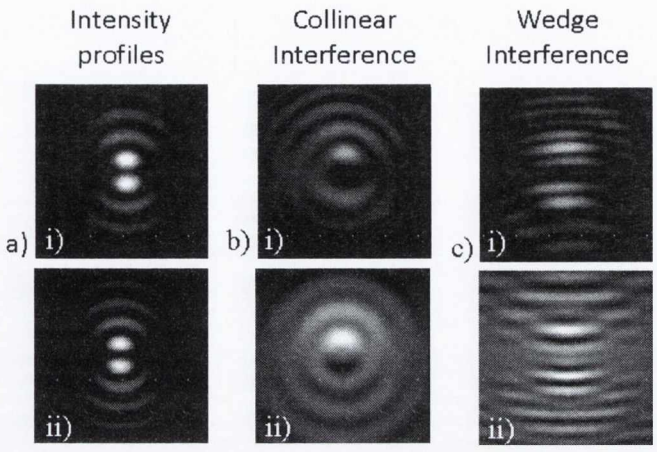

Figure 3-9: 1st order beam mode for $\alpha = 0°$. (a) Intensity profiles (i) experimental (ii) simulation. (b) Collinear interference (i) experimental. (c) Wedge interference (i) experimental (ii) simulation (ii) simulation.

The intensity profiles for the isolated first-order profile, that is orthogonally polarised with respect to the input, as α is increased from zero to 45^0 is presented in Figure 3-10(a) for the experimental profiles and Figure 3-10(b) for Mathematica simulations. As α increases the intensity along the dislocation increases, from zero when $\alpha = 0^0$ degrees Figure 3-10(a-i) to a maximum at $\alpha = 45^0$ where each ring has an azimuthally smooth intensity profile Figure 3-10(a-vii), until each ring has an azimuthally smooth intensity profile Figure 3-10 (a-vii).

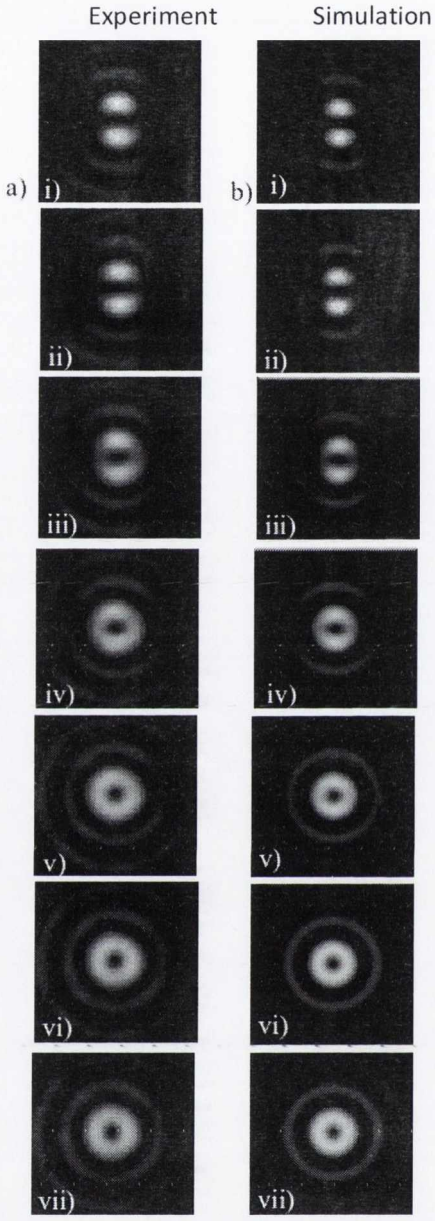

Figure 3-10: Experimental (a) and simulations (b) of the isolated 1st order beam component as a function of (i) 0°(ii) 8° (iii) 16° (iv) 24° (v) 32° (vi) 40° (vii) 45°.

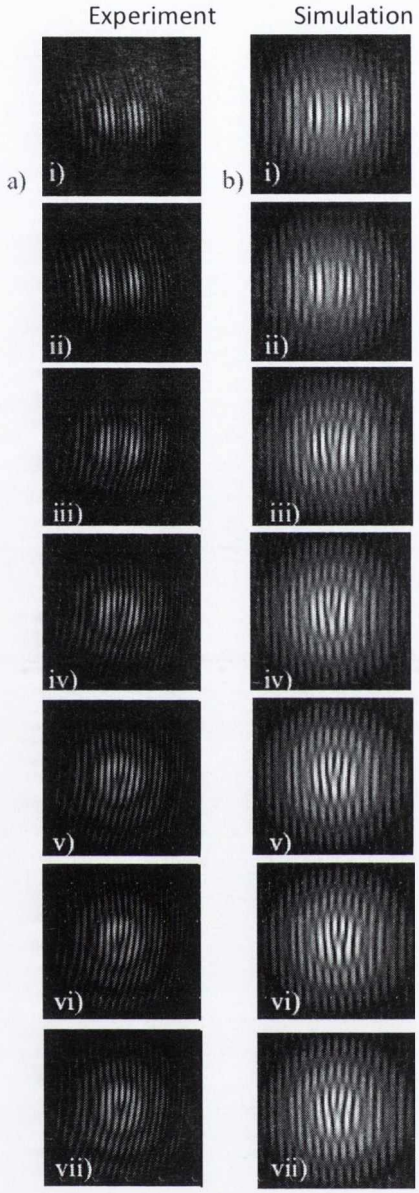

Figure 3-11: Experimental (a) and simulations (b) of the isolated 1st order beam component interfered with a Gaussian beam as a function of (i) 0°(ii) 8° (iii) 16° (iv) 24° (v) 32° (vi) 40° (vii) 45°.

The corresponding experimental wedge interference images are presented in Figure 3-11(a) and Mathematica simulations in Figure 3-11(b). For $\alpha > 0^0$ the interference patters reveal the presence of an extra fringe located at the position of the singularity indicating the presence of a 2π phase step around the beam axis. The alternating π phase between the rings is also seen revealing the radial phase profile.

3.6.2. Stokes polarimetry and phase extraction

The phase profile of a beam with complex phase can be extracted using Stokes polarimetry using the method outlined here [51]. This method requires the interference between orthogonally polarised sample and reference beam with matching radius of curvatures. The superposition of two orthogonally polarised beams generates an elliptically polarised state. If the reference beam is of planar phase and the sample beam has a complex phase, measuring the ellipiticty as a function of angle around the beam will reveal the complex phase profile.

The S_2 and S_3 Stokes parameters as defined by Eq. (3.35), are used to determine the phase difference between two beams using Eq.(3.36).

$$\begin{aligned} S_2 &= 2E_x E_y \cos\kappa \\ S_3 &= 2E_x E_y \sin\kappa \end{aligned} \tag{3.35}$$

$$\kappa = \tan^{-1}\left(\frac{S_3}{S_2}\right). \tag{3.36}$$

The experimental arrangement for the determination of the Stokes parameters was setup as in Figure 3-12, the selection of the 1st order

beam is the same as the previous section. The polarisation of the Gaussian arm is set to be orthogonal to the conical arm. A 5 cm positive lens is used in the Gaussian arm to match the curvature of the beam in the conical arm and is positioned such that the propagation length in each arm is the same. After recombination at BS2 a further quarter-wave plane P3 and linear polarised (LP) are used as the Stokes polarisers. The Stokes parameters are measured using Eq.(3.37), the subscript described the angle of the fast axis of P3 or the transmission plane of LP relative to one of the incident polarisation planes,

$$\begin{aligned} S_2 &= I(P3_{45}, LP2_{45}) - I(P3_{135}, LP2_{135}), \\ S_3 &= I(P3_{45}, LP2_0) - I(P3_{135}, LP2_0). \end{aligned} \tag{3.37}$$

Processing the intensity profiles was preformed using Matlab.

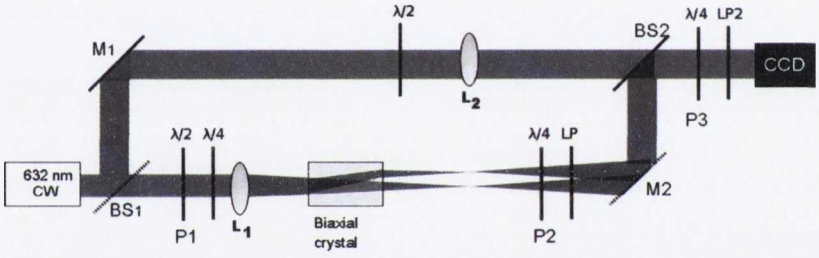

Figure 3-12: Experimental setup for stokes polarimetry.

3.6.3. Phase profiles

Figure 3-13 presents the phase profiles extracted via Stokes polarimetry for the values of α as used in Figure 3-13. For α = 0° there is a maximum phase modulation of π between the alternating rings and across the dislocation line, as Figure 3-13(i) shows. For α > 0° a complete revolution around the beam axis now incurs a 2π phase modulation. Elliptically polarised light generates a B_1 field component with 2π winding of phase Figure 3-13(ii-vi) indicates the presence of an optical vortex. Figure 3-14 compares the experimental and theoretical weighting of phase around

the beam axis (θ) for angles (α) for the isolated conical B_1 field. For α = 45°, there is an even variation of phase around the beam axis.

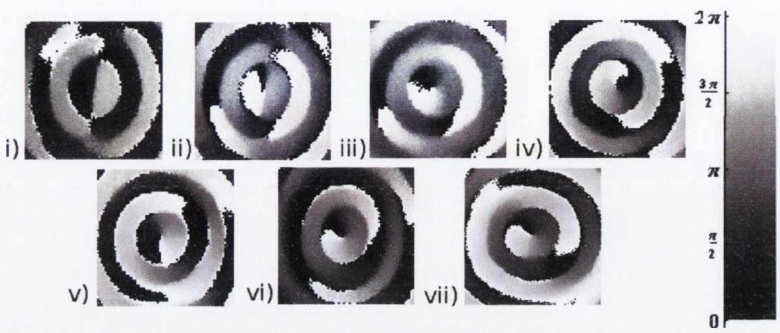

Figure 3-13: Phase plots as a function of α (i) 0°(ii) 8° (iii) 16° (iv) 24° (v) 32° (vi) 40° (vii) 45°.

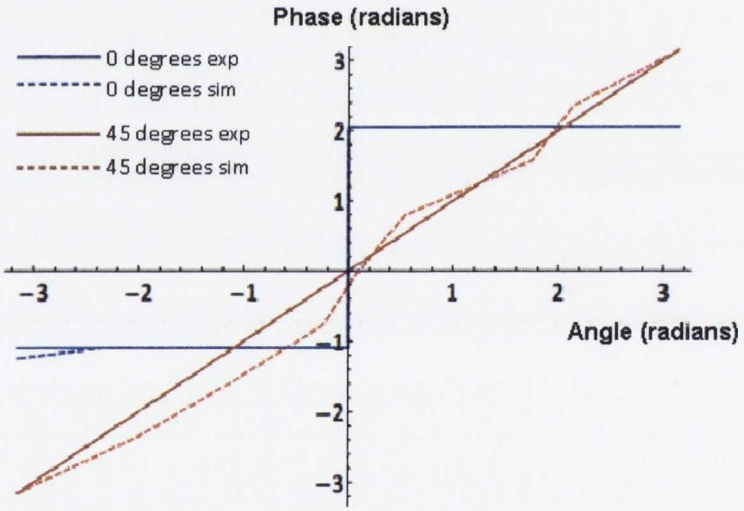

Figure 3-14: Theoretical and experimental distribution of phase around the beam axis. Experimental phase extracted from Figure 3-13 (i) for 0° and (ii) 45°.

3.7 Discussion

To assure continuity of a field with an optical vortex component there must be a 2π phase step at $\theta = 2\pi$. Isolating the B_1 field component from the B_0 field component transforms the conically diffracting beam from a vector field describing the rotation of the polarisation vector around the beam axis into a scalar field where the polarisation is uniform around the axis. As section 3.3.4 demonstrated, a scalar beam with an azimuthally uniform intensity profile carries an OAM per photon corresponding to the topological charge of the vortex present. This is seen in Figure 3-8(a-b), where the first-order mode generated from circularly polarised light generated an azimuthally smooth intensity profile around each of the rings. The incident left circular polarisation with SAM of $\sigma = +1\hbar$ generates an OAM of $\ell = +1\hbar$, arising from the formation of a scalar beam described by an optical vortex of charge +1. When $\alpha = 0°$, the presence of a dislocation line results in a discontinuity of the field along the direction of the dislocation. The extracted phase profiles Figure 3-13(i) show a π phase step, in conjunction with the interference measurement from Figure 3-11(i) show that there is no optical vortex present and the field has zero OAM per photon. As α is increased, the SAM incident upon the crystal is non-zero and consequently the optical vortex component of the field is non-zero. The phase profiles from Figure 3-13 (ii-vi) show the 2π winding of phase around the beam axis, indicating the optical Figure 3-13 vortex component is non-zero. The intensity along the direction of the shear dislocation in Figure 3-10 varies as $\sin(2\alpha)$, the J_{sp} component of Eq.(3.34), as Figure 3-15 shows. The superimposed fields (B_0 and B_1) are only mutually perpendicular when the incident light is circularly polarised, ensuring an even division of power between the fields upon separation. When the light is linearly polarised, the B_1 component only accounts for ½ of the power in the B_0 component, or a ¼ of the total incident power. The intensity pattern in Figure 3-9(a) is that of a

Hermite Bessel beam, one of the basis states of a first-order Bessel beam. The characteristic features of these beams is the line of zero amplitude separating the alternating lobes. A radial electric field profile of these beams along for HB_{01} in the horizontal direction would correspond to the electric field profile of a first-order Bessel beam. These constituent Bessel beam component are formed in the conical beam and have been referred to as "fermoinic brushes" in the literature [52]. The lobes are π out of phase as the interference and phase measurement show, and represent one-half of the phase rotation of the first-order beam. Rotating the incident polarisation by setting $\alpha = 90°$, generates the orthogonal Hermite Bessel beam with the direction of the dislocation lying in the perpendicular plane. These orthogonal Hermite Bessel beam states can be used to construct a first-order Bessel beam with radial and azimuthal polarisation[45].

When the incident light is elliptically polarised, the B_0 and B_1 fields are not mutually perpendicular at all points around R_0, due the shared polarisation vectors between the elliptically polarised states. The variation of the ratio of optical power between the B_0 and B_1 fields varies as one over the non J_{sp} component of Eq.(3.38)

$$\frac{\sin^2(2\alpha)}{2} \tag{3.38}$$

The variation of transmitted power as a function of α in Figure 3-15, and agrees closely with theory. This variation of ratio of the optical power between the respective fields coupled with the phase dependence on the incident SAM, gives the variation of J_{orb} due to ICD in accordance with Eq.(3.34). For $\alpha = (0^0, 8^0\ 16^0, 24^0, 32^0, 40^0, 45^0)$ the corresponding experimental OAM expectation values $J_{orb} = (0, 0.442, 0.76, 0.928, 0.966, 0.984, 1)\ \hbar$ per photon, which compares closely to theory as in Figure 3-17.

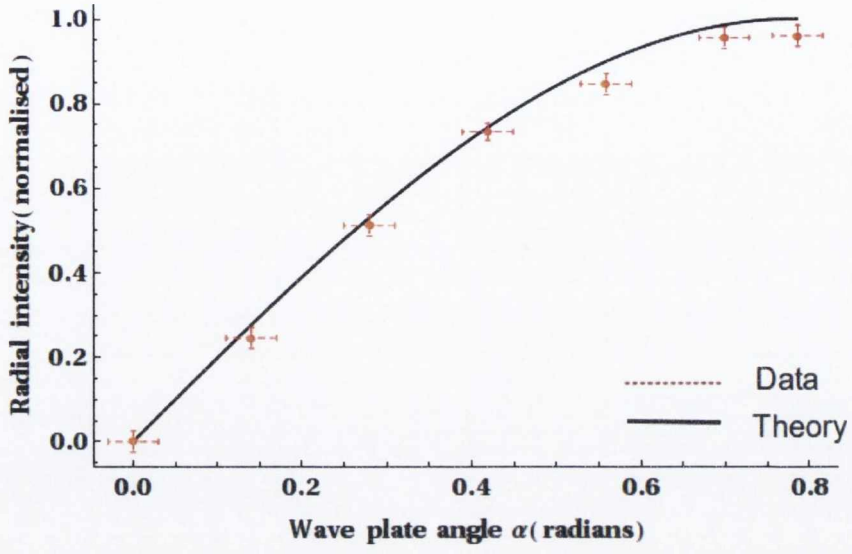

Figure 3-15: Intensity along the direction of the shear dislocation as a function of wave-plate angle (α).

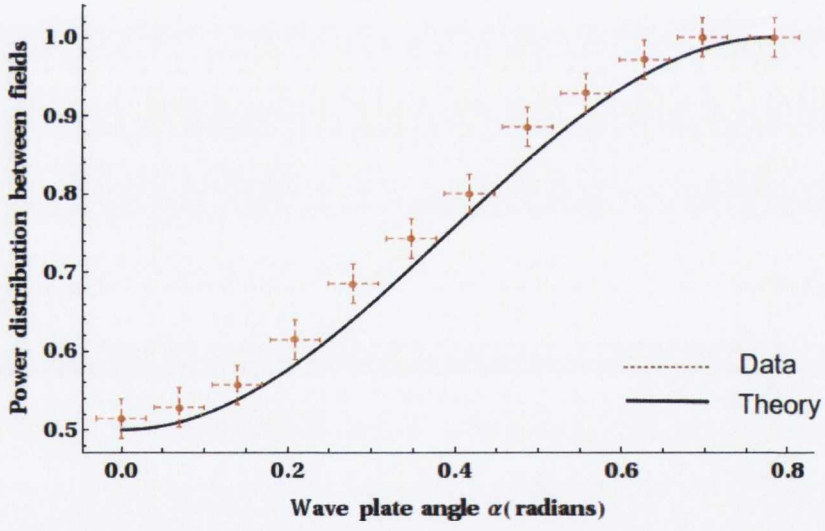

Figure 3-16: Power distribution as a function of α between the separated B_0 and B_1 field fitted against the experimental data

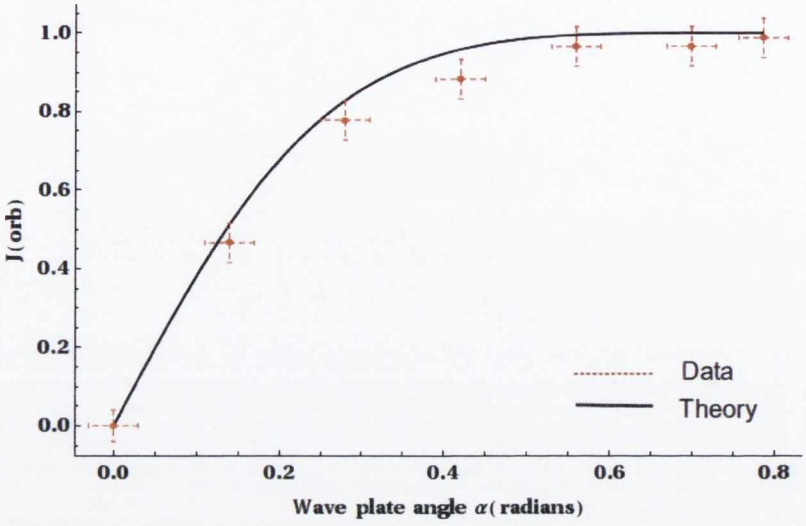

Figure 3-17: Combining Figure 3-15 and Figure 3-16 gives the experimental OAM per photon as a function of wave-plate angle (α).

3.8 Conclusion

To conclude, the method for the transformation of elliptically polarised light and subsequent isolation of the conical beam component with continuously variable fractional OAM in the range 0 to 1ħ per photon has been presented. Investigations into the SAM to OAM of ICD in the literature have so far only covered the conversion of circularly polarised light [32,47]. This work provides the first expansion of the circularly polarised case examining the generation of non-integer OAM from an elliptically polarised incident beam.

A circularly polarised beam with a known handedness is transformed into a superposition of orthogonally polarised beams, one with and the other without an optical vortex. These beams are mutually orthogonal at all points around R_0 enabling the complete isolation of the vortex beam from the planar component. The resulting transformation enables 1:1 mapping of the incident SAM expectation value to the OAM expectation value albeit at half the incident intensity. Elliptically

polarised light does not generate two mutually orthogonal beams at all points around R_0, and therefore the optical vortex component cannot be fully isolated. Upon isolation of the orthogonal polarisation component, the phase profile of the optical vortex is no longer smoothly varying giving it a fractional OAM. The non-integer expectation value of the incident SAM is converted into a non-integer OAM expectation value but has a term dependent on the incident polarisation describing the degree of isolation between the respective B_0 and B_1 components. Linear polarisation, which has zero SAM per photon, generates a B_1 field with a π phase modulation, resulting in the optical vortex component being of zero amplitude and hence zero OAM per photon. The ability to actively select and tune the expectation value of the OAM per photon in a highly controllable manner using polarisation optics, which is generally only used to modify the SAM expectation value has been clearly shown, this method generates structurally stable beams with high fidelity and does not require an interferometric superposition of different modes [29-30].

This work resulted in the publication *D. P. O'Dwyer, C. F. Phelan, Y. P. Rakovich, P. R. Eastham, J. G. Lunney, and J. F. Donegan, "Generation of continuously tunable fractional optical orbital angular momentum using internal conical diffraction," Optics Express* ***18*** *(16), 16480-16485 (2010).*

3.9 References

1 D. P. O'Dwyer, C. F. Phelan, Y. P. Rakovich, P. R. Eastham, J. G. Lunney, and J. F. Donegan, "Generation of continuously tunable fractional optical orbital angular momentum using internal conical diffraction," Optics Express **18** (16), 16480-16485 (2010).

2 R. W. Ditchburn, *Light*. (Academic Press, London, 1975).

3 J. D. Jackson, Classical Electrodynamics (1975).

4 M. V. Berry, "Optical currents," Journal of Optics A. **11** (9), 094001 (2009).

5 R. A. Beth, "Mechanical Detection and Measurement of the Angular Momentum of Light," Physical Review **50** (2), 115 (1936).

6 J. M. Vaughan and D. V. Willetts, "Temporal and interference fringe analysis of TEM01* laser modes," Journal of the Optical Society of America A **73** (8), 1018-1021 (1983).

7 L. Allen, S. M. Barnett, and M.J. Padgett, *Optical angular momentum*. (Bristol: Institute of physics publishing, 2003).

8 M. V. Berry, "Paraxial beams of spinning light," SPIE Optical Engineering Press **3487**, 6-13 (1998).

9 M. Padgett, J. Arlt, N. Simpson, and L. Allen, "An experiment to observe the intensity and phase structure of Laguerre--Gaussian laser modes," American Journal of Physics **64** (1), 77-82 (1996).

10 J. F. Nye and M. V. Berry, "Dislocations in Wave Trains," Proceedings of the Royal Society of London. A. Mathematical and Physical Sciences **336** (1605), 165-190 (1974).

11 N. B. Simpson, K. Dholakia, L. Allen, and M. J. Padgett, "Mechanical equivalence of spin and orbital angular momentum of light: an optical spanner," Optics Letters **22** (1), 52-54 (1997).

12 J. Courtial, K. Dholakia, D. A. Robertson, L. Allen, and M. J. Padgett, "Measurement of the Rotational Frequency Shift Imparted to a Rotating Light Beam Possessing Orbital Angular Momentum," Physical Review Letters **80** (15), 3217 (1998).

13 A. Vaziri, J. Pan, T. Jennewein, G. Weihs, and A. Zeilinger, "Concentration of Higher Dimensional Entanglement: Qutrits of Photon Orbital Angular Momentum," Physical Review Letters **91**, 227902 (2003).

14 S. Franke-Arnold;, S. Barnett;, E. Yao, J. Leach;, J. Courtail;, and M. Padgett., "Uncertainty principle for the angular postion and angular momentum," New J. Phys **6**, 103 (2004).

15 A.V. Carpentier, H. Michinel, J. R. Salgueiro, and D. Olivieri, "Making optical vortices with computer-generated holograms," American Journal of Physics **76** (10), 916-921 (2008).

16 C. Rotschild, S. Zommer, S. Moed, O. Hershcovitz, and S. G. Lipson, "Adjustable Spiral Phase Plate," Applied Optics **43** (12), 2397-2399 (2004).

17 S. S. R. Oemrawsingh, J. A. W. van Houwelingen, E. R. Eliel, J. P. Woerdman, E. J. K. Verstegen, J. G. Kloosterboer, and G. W. t Hooft, "Production and Characterization of Spiral Phase Plates for Optical Wavelengths," Applied Optics **43** (3), 688-694 (2004).

18 E Karimi, B Piccirillo, E Nagali, L Marrucci, and E Santamato, "Efficient generation and sorting of orbital angular momentum eignmodes of light by thermally tuned q-plates," Applied Optics **94** (23), 231124 (2009).

19 J. Arlt, K. Dholakia, L. Allen, and M. J. Padgett, "The production of multiringed Laguerre–Gaussian modes by computer-generated holograms," Journal of Modern Optics **45** (6), 1231 - 1237 (1998).

20 J. Arlt, R. Kuhn, and K. Dholakia, "Spatial transformation of Laguerre–Gaussian laser modes," Journal of Modern Optics **48** (5), 783 - 787 (2001).

21 N. R. Heckenberg, R. McDuff, C. P. Smith, and A. G. White, "Generation of optical phase singularities by computer-generated holograms," Optics Letters **17** (3), 221-223 (1992).

22 E. Nagali, F. Sciarrino, F. De Martini, B. Piccirillo, E. Karimi, L. Marrucci, and E. Santamato, "Polarization control of single

photon quantum orbital angular momentum states," Optics Express **17** (21), 18745-18759 (2009).

23 L. Marrucci, C. Manzo, and D. Paparo, "Optical Spin-to-Orbital Angular Momentum Conversion in Inhomogeneous Anisotropic Media," Physical Review Letters **96** (16), 163905 (2006).

24 D.L. Andrews, *Structured light and its applications.* (Acdemic Press, 2008).

25 G. Nienhuis, "Angular Momentum and Vortices in Optics", in *Structured Light and Its Applications*, edited by L. Andrews David (Academic Press, Burlington, 2008), pp. 19-62.

26 A. T. O'Neil, I. MacVicar, L. Allen, and M. J. Padgett, "Intrinsic and Extrinsic Nature of the Orbital Angular Momentum of a Light Beam," Physical Review Letters **88** (5), 053601 (2002).

27 S. S. R. Oemrawsingh, E. R. Eliel, G. Nienhuis, and J. P. Woerdman, "Intrinsic orbital angular momentum of paraxial beams with off-axis imprinted vortices," Journal of the Optical Society of America A **21** (11), 2089-2096 (2004).

28 L. Allen, J. Courtial, and M. J. Padgett, "Matrix formulation for the propagation of light beams with orbital and spin angular momenta," Physical Review E **60** (6), 7497 (1999).

29 J. Leach and et al., "Observation of the vortex structure of a non-integer vortex beam," New Journal of Physics **6** (1), 71 (2004).

30 J. B. Götte, K. O'Holleran, D. Preece, F. Flossmann, S. Franke-Arnold, S. M. Barnett, and M. J. Padgett, "Light beams with fractional orbital angular momentum and their vortex structure," Optics Express **16** (2), 993-1006 (2008).

31 S. Orlov, K. Regelskis, V. Smilgevicius, and A. Stabinis, "Propagation of Bessel beams carrying optical vortices," Optics Communications **209** (1-3), 155-165 (2002).

32 M. V. Berry, M. R. Jeffrey, and M. J. Mansuripur, "Orbital and spin angular momentum in conical diffraction," Journal of the Optical Society of America A **7** (11), 685-690 (2005).

33 M. Harris, C. A. Hill, and J. M. Vaughan, "Optical helices and spiral interference fringes," Optics Communications **106** (4-6), 161-166 (1994).

34 N. R. Heckenberg, R. McDuff, C. P. Smith, H. Rubinsztein-Dunlop, and M. J. Wegener, "Laser beams with phase singularities," Optical and Quantum Electronics **24** (9), S951-S962 (1992).

35 J. Durnin, "Exact solutions for nondiffracting beams. I. The scalar theory," Journal of the Optical Society of America A **4** (4), 651-654 (1987).

36 J. Durnin, J. Miceli, and J. H. Eberly, "Diffraction-free beams," Physical Review Letters **58** (15), 1499 (1987).

37 K. Volke-Sepulveda, V. Garcés-Chávez, S. Chávez-Cerda1, J. Arlt, and K. Dholakia, "Orbital angular momentum of a high-order Bessel light beam," Journal of Optics B: Quantum and Semiclassical Optics **4** (2), S82 (2002).

38 B. Shao, S. C. Esener, J. M. Nascimento, M. W. Berns, E. L. Botvinick, and M. Ozkan, "Size tunable three-dimensional annular laser trap based on axicons," Optics Letters **31** (22), 3375-3377 (2006).

39 C. S. R. Arimoto, T. Tanaka, and S. Kawata, "Imaging properties of axicon in a scanning optical system," Optical Society of America **31** (31), 6653-6658 (1992).

40 R. Arimoto, C. Saloma, T. Tanaka, and S. Kawata, "Imaging properties of axicon in a scanning optical system," Optical Society of America **31** (31), 6653-6658 (1992).

41 J Durnin, J. J. Miceli, and J. H. Eberly, "Diffraction-free beams," Physical Review Letters **58** (15), 1499 (1987).

42 J. Durnin, "Exact solutions for nondiffracting beams. I. The scalar theory," Journal of the Optical. Society of America **4** (4), 651 (1987).

43 J. Arlt and K. Dholakia, "Generation of high-order Bessel beams by use of an axicon," Optics Communications **177** (1-6), 297-301 (2000).

44 X. F. Li, R. J. Winfield, S. O'Brien, and G. M. Crean, "Application of Bessel beams to 2D microfabrication," Applied Surface Science **255** (10), 5146-5149 (2009).

45 W. C. Soares, D. P. Caetano, and J. M. Hickmann, "Hermite-Bessel beams and the geometrical representation of nondiffracting beams with orbital angular momentum," Optics Express **14** (11), 4577-4582 (2006).

46 M. V. Berry, M. J. Jeffrey, and M. Mansuripur, "Orbital and spin angular momentum in conical diffraction," Journal of Optics A. (11), 685 (2005).

47 T. A. King, W. Hogervorst, N. S. Kazak, N. A. Khilo, and A. A. Ryzhevich, "Formation of higher-order Bessel light beams in biaxial crystals," Optics Communications **187** (4-6), 407-414 (2001).

48 W.M. Lee, X.-C. Yuan, K. Dholakia, Experimental observation of optical vortex evolution in a Gaussian beam with an embedded fractional phase step, Optics Communications, Volume 239, Issues 1-3, 1 September 2004, Pages 129-135, ISSN 0030-4018, DOI: 10.1016/j.optcom.2004.05.035.

49 M V Berry, "Optical vortices evolving from helicoidal integer and fractional phase steps" Journal of Optics A: Pure and Applied Optics, **6** (2), 1464-4258 (2004).

50 M. C. Pujol, M. Rico, C. Zaldo, R. Solé, V. Nikolov, X. Solans, M. Aguiló, and F. Díaz, "Crystalline structure and optical spectroscopy of Er3+-doped $KGd(WO_4)_2$ single crystals," Applied Physics B: Lasers and Optics **68** (2), 187-197 (1999).

51 V. G. Denisenko, A. Minovich, A. S. Desyatnikov, W. Krolikowski, M. S. Soskin, and Y. S. Kivshar, "Mapping phases of singular scalar light fields," Optics Letters **33** (1), 89-91 (2008).

52 M.V. Berry, R. Bhandari, and S. Klein, "Black plastic sandwiches demonstrating biaxial optical anisotropy," European Journal of Physics **20** (1), 1 (1999).

Chapter 4

CASCADE CONICAL DIFFRACTION

4.1 Abstract

Crystal of identical length when placed in series and with the cones of ICD anti-parallel enables the reformation of the initial Gaussian beam. At intermediate angles the optical power is shared between the Gaussian spot and the ring. The ability to tune the intensity between the cone of ICD and the incident Gaussian beam is theoretically derived and shown experimentally.

Right-circularly polarised light upon ICD is converted into a first-order beam has an optical vortex of charge -1. Upon propagation of the first-order beam through a second biaxial crystal, a process which is termed cascade conical refraction, the generated beam is a superposition of orthogonally polarised fields of charge 0 and -1 or 0 and -2. This spin to orbital angular momentum conversion provides a new method for the generation and annihilation of optical vortices in an all-optical arrangement that is solely dependent on the incident polarisation and vortex handedness.

This work resulted in the publication: *D. O'Dwyer, C. Phelan, Y. Rakovich, P. Eastham, J. Lunney, and J. Donegan, "The creation and annihilation of optical vortices using cascade conical diffraction," Opt. Express 19, 2580-2588 (2011).*

4.2 Introduction

Cascade ICD is the propagation of light through successive biaxial crystals. The intensity distribution of the generated conical beam after passage through successive crystals directly depends on these two factors. The quality factor ρ_0 is directly dependent upon the combined crystal lengths. ICD forms a slant cone of light; the direction γ_c defines the orientation of the rings moving from tangential to radial polarisation as shown in Fig. 4-1.

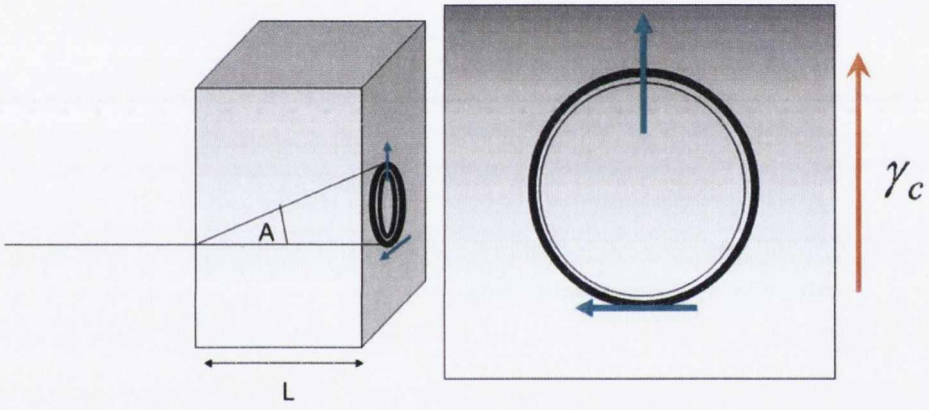

Figure 4-1: Crystal orientation γ_c showing the orientation of the optic axis and the slant cone of ICD of angle A.

In the cascade regime, the relative orientation between the successive crystals and their relative length directly affects the generated intensity profile. Of late Berry has expanded his initial work on conical diffraction, for the general case of propagation of light though n-cascaded crystals of arbitrary length and relative orientations [1]. The main consequence of cascade ICD for crystals with parallel axes (γ_c) is the summation of the respective R_0 values with the successive crystals acting as a single crystal. As the optic axes of the crystals are rotated with respect to each other, the generated intensity profile consists of two main features, the outer ring, which has the sum of the

R0 values, and the inner ring with the difference of the R_0 values of the two crystals. In this chapter only biaxial crystals of similar lengths are considered, in which $R_{01} \approx R_{02}$, hence issues and details arising from the use of crystals with differing lengths are not dealt with here. The sister thesis to this project by Phelan provides a more general investigation of cascade ICD focusing on beam shaping and cascade ICD using biaxial crystals of differing length.

This chapter expands on the initial work of Berry as outlined in chapter 2, with two specific cases being treated as per the notation of Phelan. Firstly, the work of the previous chapter is expanded to investigate the transformation of an optical vortex upon an ICD process. Such beams may find applications in quantum information processing and in studies of the propagation of optical singularities [2-7].

Secondly, the transformation of a Gaussian beam upon a cascade ICD process using two biaxial media, with no intermediate wave plates, of similar length is investigated, as the relative orientation between the crystal axes is rotated through 180°. This concept has recently been used in a conically diffracting laser where a biaxial crystal is used in the laser cavity[8-12] and will be used in the next chapter in the conically diffracting optical trap.

4.3 Cascade conical diffraction

The explanation of ICD as put forth in Chapter 2 where one considers the double refraction of a ray propagating slightly off axis from the optic axis provides the simplest means to describe the cascade process. A ray incident upon the optic axis of BC1 defines a cone of light within the crystal, around which off axis rays doubly refract. The emerging cylinder of light of radius R_{01}, when directed along the optic axis of a second crystal of same biaxality (BC2), defines a new range of cones of ICD within the crystal for each point on the incident ring. The emerging cascade beam profile consists of the sum of all the cones of ICD for each

point on the generating ring, Figure 4-2. The resulting cascade conically refracted ray consists of a new geometric ring radius formed from the sum of R_{01} and R_{02} and a central feature that depends upon the difference of the radii.

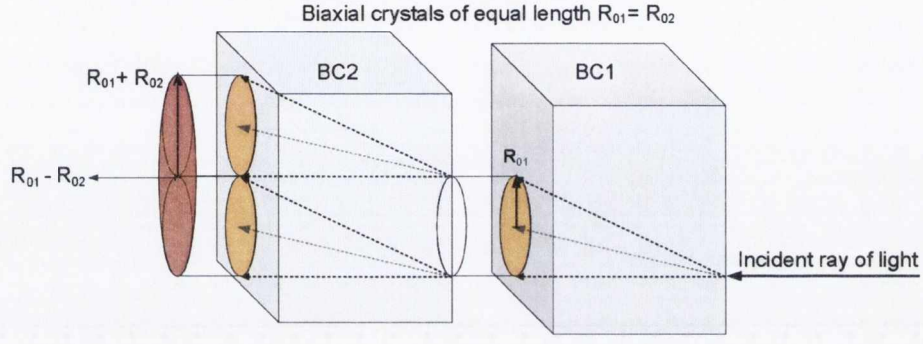

Figure 4-2: Cascade conical refraction for crystals of equal length. The incident ray defines the cone of ICD, which upon a successive ICD process defines a rage of cones inside the second crystal (BC2) each of which defines their own cones of ICD.

Next if the propagation of rays slightly off axis is considered, the intensity profile generated from BC1 consists of a double ring of light with all points on the ring linearly polarised with a π rotation of polarisation around the circuit of the ring. When the crystals are aligned parallel to each other, the direction of propagation of the linear polarised light corresponds to that of the proceeding crystal and the orientation of the linear polarisations are directly transposed onto the new geometric ring radius, Figure 4-3. When the two crstalsa re set at 180° with respect to one another, the coe formed by the first crystal is reversed by the second crystal refroming the intial Gaussian spot.

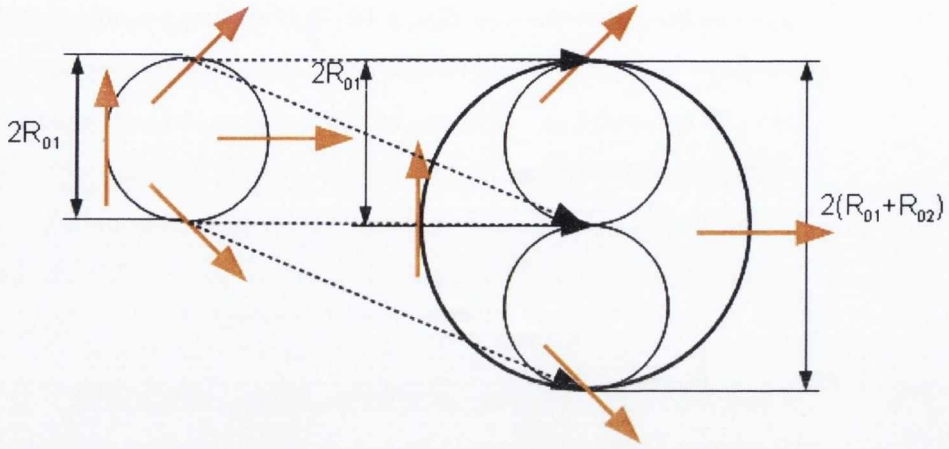

Figure 4-3: Cascade refraction schematic for crystals of same length i.e. R_{01} = R_{02}. All points on the ring R_{01} are doubly refracted.

4.3.1. Basic Theory of Cascade ICD

The general equation for the transformation of a paraxial beam of light upon ICD as a function of the Fourier transform of the field **a**(**P**) is given by:

$$\mathbf{E}(\mathbf{R},z)=\frac{k}{2\pi}\iint dP e^{-ik\mathbf{P}\cdot\mathbf{r}}e^{ikP^2z}[\cos(kPR_0)\mathbf{I}-i\sin(kPR_0)\mathbf{M}(\theta_P)]\mathbf{a}(\mathbf{P}) \qquad (4.1)$$

$$\mathbf{I}=\begin{pmatrix}1 & 0\\ 0 & 1\end{pmatrix} \qquad (4.2)$$

$$\mathbf{M}(\theta_P)=\begin{pmatrix}\cos\theta_P & \sin\theta_P\\ \sin\theta_P & -\cos\theta_P\end{pmatrix} \qquad (4.3)$$

Here R is the transverse cone-centred position, kP= k (Px , Py) = kP(cosθ_P ,sin θ_P) is the transverse wave vector, I is the identity matrix, and k = n2k0 is the crystal wave-number. R0 is the radius of the cylindrical beam emerging from the crystal. When the input beam is focused on the entrance face of the crystal the variable Z in Eq. (1) which describes the propagation distance is defined as Z = L + (z-L)n2,

where L is the length of the crystal and z is the distance from the entrance face. The components of a(P) are Fourier representations of the Cartesian components of the field incident on the entrance face. For the case of a Gaussian beam which is focused to form a beam waist at some other position, a(P) may be taken to be the field at the waist and z measured from its location. In the alternative basis of

circularly-polarised fields, with Jones vectors (1, ±i)/ 2 , the matrix M(θp) is replaced by

$$\mathbf{M}(\theta_P)=\begin{pmatrix} 0 & e^{i\theta_P} \\ e^{-i\theta_P} & 0 \end{pmatrix} \tag{4.4}$$

From Eqs. (4.1) and (4.4) it can be see that a circularly-polarised beam becomes a superposition of a component of the same circular polarisation, and a component with the opposite polarisation and an azimuthal phase factor. This factor results in an optical vortex of the same charge as the incident helicity; +1 for left-circular and -1 for right-circular polarisation. More explicitly, conical diffraction of a uniform left-(right-) polarised beam generates a superposition of two Bessel-like beams of zero (B_0) and first order (B_1)

$$\mathbf{E}(\mathbf{R},z)=B_0(R,R_0,Z)\mathbf{e}^{+(-)}+B_1(R,R_0,Z)\mathbf{e}^{-(+)} \tag{4.5}$$

$$B_0(\mathbf{R},R_0,Z)=k\int_0^\infty P\cos(kPR_0)a(P)J_0(kPR)e^{-\frac{1}{2}kP^2Z}dP \tag{4.6}$$

$$B_1(\mathbf{R},R_0,Z)=k\int_0^\infty P\sin(kPR_0)a(P)J_1(kPR)e^{-\frac{1}{2}kP^2Z}dP \tag{4.7}$$

where e-(+) denotes right- (left-) circular polarisation, and we have assumed that the incident beam is circularly symmetric. The individual profiles B0 and B1 satisfy the paraxial wave equation and have been shown experimentally to agree with theory [9]. In cascade conical diffraction, a beam propagates through a series of biaxial crystals.

Additionally, by manipulating the polarization state between the crystals in the cascade, a wide variety of beams of varying vorticity can be generated. In our experiments, we consider a two-crystal cascade whose optical axes are aligned, in which only one of the circular components after the first crystal is transmitted into the second, which we assume to be of equal length for simplicity. Suppose first that only the circularly polarised B_1 beam is incident on the second crystal. If the beam into the first crystal is right-circular then B_1 is left-circularly polarised, and can be isolated with a left-circular polarizer. Its Fourier representation is

From the above equations we can infer that under conical diffraction the Fourier transform of the incident beam **a**(**P**) is transformed into,

$$e^{-\frac{1}{2}ikP^2z}[\cos(kPR_0)\mathbf{I} - i\sin(kPR_0)\mathbf{M}(\theta_P)]\mathbf{a}(P) \qquad (4.8)$$

If Eq.(4.8) is set as the incident beam the corresponding Fourier transform can be generated through successive biaxial crystals by matrix multiplication. Repeating this process for each successive ICD process provides the basic method for the derivations that are obtained in this chapter. The electric field generated in superpostion using multiple crystals is denoted by (B_{cl}), generated from crystal number (c) in the cascade and described by a Bessel function of order (l). We consider biaxial crystals of similar length where the difference in crystal length results in a $\Delta\rho_0 << 1$.

4.4 Addition and subtraction of an optical vortex

The previous chapter demonstrated that internal conical diffraction (ICD) using a single biaxial crystal provides an efficient means for the conversion of a circularly polarised Gaussian mode ($\sigma = \pm 1\hbar$) into a superposition of high quality Bessel beams of zero order with $\ell = 0\hbar$ and first order with $\ell = \pm 1\hbar$, with a net $\pm\frac{1}{2}\hbar$ OAM per photon [13-16]. These OAM states have orthogonal polarisations and are easily separable enabling polarisation switching between either mode. Such is the control that the generated OAM can be continuously tuned between 0 and $\pm 1\hbar$ per photon using elliptically polarised light [17]. The ability to transform a zero order non-diverging Bessel beam into a first and higher order Bessel beams under the conditions of ICD was theoretically and experimentally address by King et al. [16]. This work required the use of an extra conical lens known as an axicon to generate the non-diverging Bessel beams. In this section the SAM to OAM conversion process is examined using a cascaded pair of biaxial crystals.

4.4.1. Theory

In the following only a two crystal cascade is considered, with the crystals assumed to be of equal length. If we have right circularly polarised light incident on the first crystal then the left circularly polarised B_1 field with a right-handed vortex can be isolated with a circular polariser, with a Fourier trasnform of the form,

$$\begin{aligned} \mathbf{a}(\mathbf{P}) &= -ie^{-\frac{1}{2}ikP^2Z}\sin(kPR_0)\mathbf{M}(\theta_p)a_{in}(P)\mathbf{e}^- \\ &= -ie^{-\frac{1}{2}ikP^2Z}\sin(kPR_0)e^{-i\theta_p}\mathbf{e}^+ \end{aligned} \tag{4.9}$$

where $a_{in}(P)$ is the Fourier representation of the radial profile of the beam that was incident on the first crystal. Substituting Eq. (4.9) into

Eq.(4.1) and performing the Fourier transformation back to real space gives the final field

$$\mathbf{E}(R,\theta,Z)=B_{12}e^{-i\theta}\mathbf{e}^{+}+B_{02}\mathbf{e}^{-}, \tag{4.10}$$

$$B_{02}=\frac{k}{2}\int_0^{\infty}P\left(\cos\left(2kPR_0\right)-1\right)a_{in}(P)J_0\left(kPR_0\right)e^{-\frac{1}{2}ikP^2Z_2}dP, \tag{4.11}$$

$$B_{12}=\frac{k}{2}\int_0^{\infty}P\left(\sin\left(2kPR_0\right)\right)a_{in}(P)J_1\left(kPR_0\right)e^{-\frac{1}{2}ikP^2Z_2}dP, \tag{4.12}$$

Here Z2=2L+(z-2L)n2 where 2L is the total length of the crystals in the cascade. In labelling the output beam components the first subscript refers to the order of the Bessel function occurring in the description of that field component and the second subscript refers to the number of crystals used. It can be seen that the output from the second crystal is a superposition of a left-circular zero-order Bessel like beam and a right-circular first-order beam. Thus for the part of the output beam the vortex present in the input has been annihilated by the action of the second crystal. If, after isolating the B1 beam, we right-circularly polarize it, its Fourier transform is

$$\mathbf{a}(\mathbf{P})=-ie^{-\frac{1}{2}ikZP^2}\sin\left(kPR_0\right)e^{-i\theta_P}a_{in}(P)\mathbf{e}^{-}, \tag{4.13}$$

and the field emerging from the second crystal is

$$\mathrm{E}(\mathbf{R},\theta,Z)=B_{12}e^{-i\theta}\mathrm{e}^{-}+B_{22}e^{-2i\theta}\mathrm{e}^{+} \tag{4.14}$$

$$B_{22}=\frac{k}{2}\int_0^{\infty}P\left(1-\cos\left(2kPR_0\right)\right)a_{in}(P)J_2\left(kPR_0\right)e^{-\frac{1}{2}ikP^2Z_2}dP, \tag{4.15}$$

In this case the vortex generated by the second crystal adds to that created by the first, resulting in a left-polarised component containing a vortex of charge two.

The beam from a general cascade can be constructed from Eq.(4.1). After each crystal the field will be a superposition of beams with Fourier representations of the form

$$\mathbf{a}(\mathbf{P}) = a(P)e^{in\theta_P}\mathbf{e}^{-(+)}, \tag{4.16}$$

corresponding to the real-space beams

$$\mathbf{E}(\mathbf{R},\theta,Z) = i^n e^{in\theta_P}\mathbf{e}^{+(-)}k\int_0^\infty PJ_n(kPR)a(P)dP, \tag{4.17}$$

A subsequent conical diffraction stage transforms such a beam into

$$e^{-i/2}\left\{\cos(kPR_0)a(P)e^{in\theta_P}\mathbf{e}^{+(-)} - i\sin(kPR_0)a(P)e^{in\theta_P}\mathbf{e}^{+(-)}e^{i(n+(-)1)\theta_P}\right\}, \tag{4.18}$$

which is again a superposition of components of the form of Eq. (4.9), with new radial profile a(P)', vorticities n', and polarisations. The output beam from a cascade is obtained by iterating the transformation of Eq. (4.13) for each stage in the cascade, and Fourier transforming the final Fourier components using Eq. (4.10). Finally, in Figure 4-4, a pictorial representation of the cascade process in which the various states in the cascade conical refraction process generated can be used to manipulate and actively select a beam with a specific total zero AM per photon.

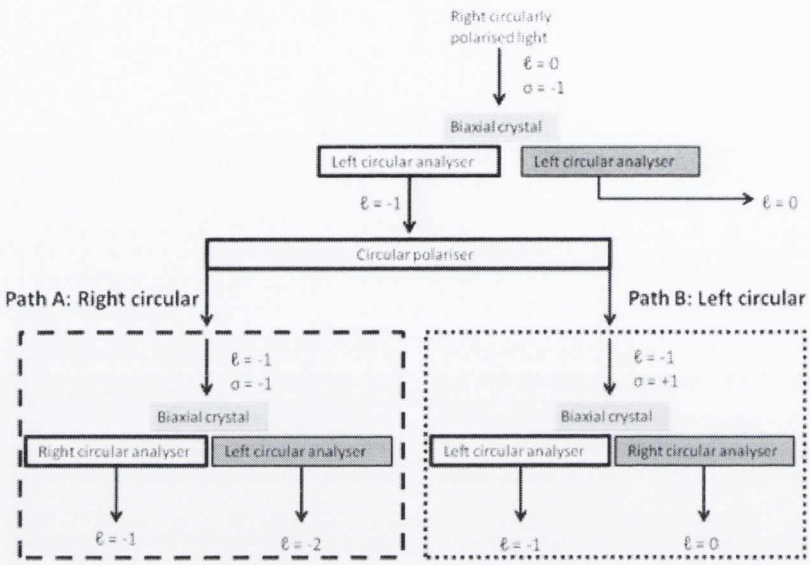

Figure 4-4: Schematic diagram of the cascade conical refraction process.

4.4.2. Experimental procedure and results

The experimental setup for transformation of circularly polarised light into an optical vortex using a pair of cascaded biaxial crystals is presented in Figure 4-5. A 10 mW HeNe Gaussian laser mode at 632.8mn is right-circularly polarised using a λ/4 plate (P1), focused to a beam waist size w of 41 μm at the 1/e2 point using a 5 cm lens (L1), and propagated along the optic axis of the biaxial crystal. The first crystal used had a length L = .0209 mm resulting in R_0= $4.13x10^{-4}$ m with an equivalent Bessel cone angle of .0196 rad. The SAM to OAM conversion efficiency was calculated by Berry [15] and is directly correlated to the strength of the crystal; this is quantified as the conical quality term ρ_o = (AL/w), and for the 1st crystal ρ_o = 9.8. The transformation of circularly polarised light upon ICD results in an equal division of the optical intensity between the B_0 and B_1 components as they are orthogonally polarised at all points around R_0 [17]. When ρ_0 >>1 the circularly polarised

light with $\sigma = \pm 1\hbar$ is converted into a superposition of OAM states with $\ell = 0$ and $\ell = \pm 1\hbar$ giving a net OAM of $\ell = \pm \frac{1}{2}\hbar$ per photon. For the cascade element in Figure 4-5 the isolated field from the previous crystal is re-circularly polarised using another quarter-wave plate and propagates along the optic axis of the 2nd biaxial crystal. The second element is 21.1mm in length with a R_0 value of 4.15×10^{-4}m giving a R_0 value of 8.28×10^{-4}m and a net $\rho_o = 15.92$ for the two crystal cascade process.

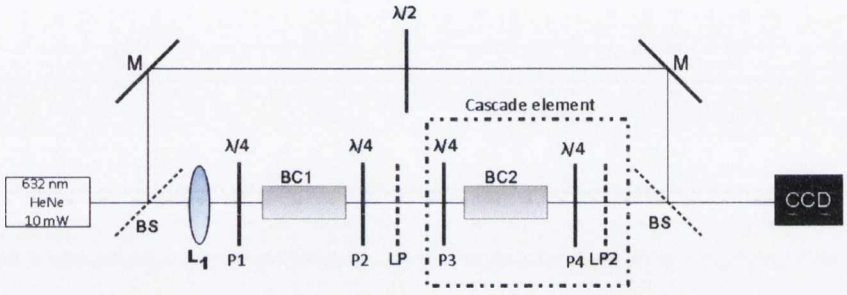

Figure 4-5: Optical setup for cascade conical diffraction, including Mach-Zehnder interferometer. Cascade element is removed to enable the imaging of the profiles from the 1st crystal. BS - beam splitters, M - Mirrors, P1/2/3/4 are λ/4 plates, LP are linear polarisers. λ/2 plate is used to rotate the Gaussian reference arm polarisation to match the polarisation of the conical field.

A Mach-Zehnder interferometer is used to examine the phase distribution of the generated conical beams and reveal the presence and charge of any optical vortices present. A Gaussian reference arm has its polarisation rotated with a λ/2 plate to match the polarisation of the conical beam component to be examined. A helical wave when collinearly interfered with a Gaussian beam with a different radius of curvature reveals a fringe interference pattern in the form of a continuous spiral, the number of which reveal the charge of the vortex present. Introducing a wedge between the Gaussian and conical beam

reveals a fringe interference pattern consisting of a series of parallel lines. The presence of an extra fringe above the singularity reveals the presence of a 2π phase step around the beam axis, the number of which indicates the charge of the optical vortex present [18]. The intensity patterns were recorded on a standard CCD camera in the far-field region of the conically diffracted beam 39 cm away from the focal image plane [13]. Upon exiting the 1st crystal the orthogonal fields are separated with a λ/4 plate (P2) and linear polariser (LP) combination. When the P2 fast axis is parallel to P1, the zero order B_0 field is selected and when it is orthogonal to P1 the 1st order field B_1 is selected.

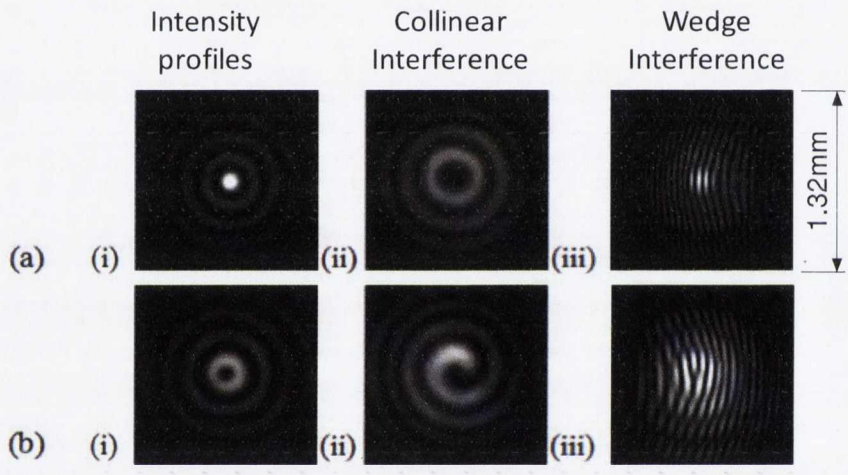

Figure 4-6: Far-field intensity patterns of separated conically diffracting beam described by a Bessel function after first biaxial crystal. (a) (i) zero order conically diffracting Bessel beam (ii) collinear interference pattern with a Gaussian beam (iii) Wedge interference pattern. (b) 1st order diffracting Bessel beam (ii) collinear interference pattern with a Gaussian beam (iii) wedge interference pattern showing 1st order edge dislocation. All images are 1.32 mm x 1.32 mm in size.

The resultant intensity and interference profiles are presented in Figure 4-6 (a) for the zero order B_{10} component and Figure 4-6 (b) for the first order B_{11} component after the first biaxial crystal with the cascade element is removed. Figure 4-6 (a) shows from left to right a zero order Bessel beam intensity profile, Figure 4-6 (a-i) the interference fringe patterns and Figure 4-6 (a-ii, iii) indicates the absence of an optical vortex. Figure 4-6 (b) shows from left to right the first order Bessel beam intensity profile, Figure 4-6 (b-i), the interference fringe patterns and Figure 4-6 (b-ii) show a single spiralling fringe. Figure 4-6 (b-ii) shows the presence of a single extra fringe positioned above the central singularity indicates the presence of an optical vortex of charge 1.

The linearly polarised first order field from Figure 4-6 (b-i) is re-circularly polarised and re-conically diffracted by inserting the cascade element in the optical setup as per Figure 4-5. The right handed optical vortex component of Figure 4-6 is either right-circularly polarised by setting the wave-plate fast axis of P3 parallel to P1(Path A) or left-circularly polarised by setting the fast axis orthogonal to P1(Path B).

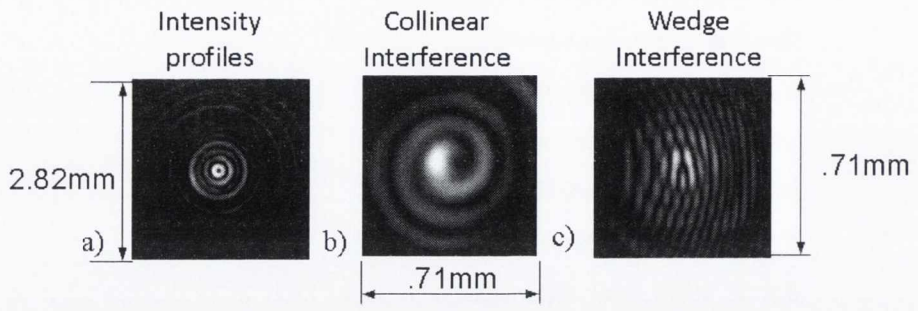

Figure 4-7: ℓ = -1 component of Path A and Path B from Figure 4-4.(a) Intensity profile (b) Collinear interference with Gaussian (iii) Wedge interference with Gaussian.

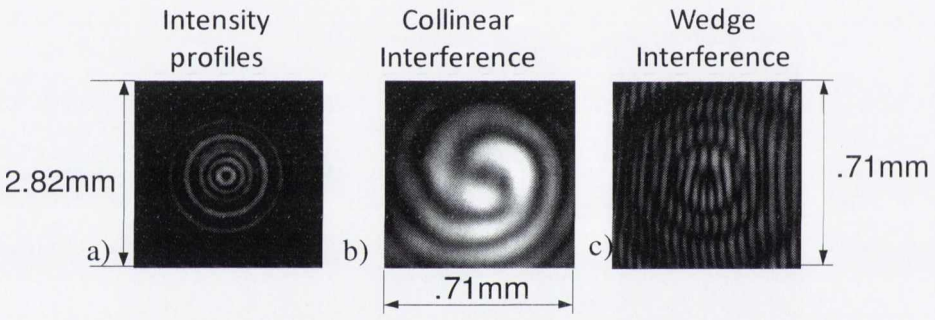

Figure 4-8: ℓ = -2 component of Path B from Figure 4-4 (a) Intensity profile (b) Collinear interference with Gaussian (iii).

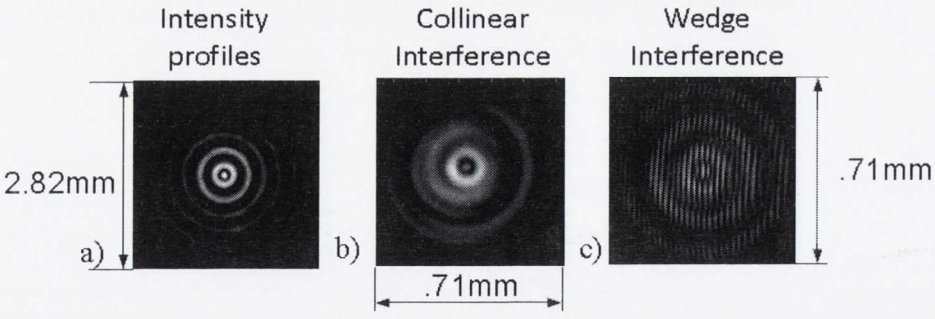

Figure 4-9: ℓ = 0 component of Path A from Figure 4-4. (a) Intensity profile (b) Collinear interference with Gaussian (iii) Wedge interference with Gaussian.

The field common to both paths in Figure 4-4 is the first order field (B_{11}) and is selected by setting the fast axes of P3 and P4 parallel to each other. The intensity and interference profiles generated from the cascade process are presented in Figure 4-7. This field component retains the vorticity of the incident beam as is evident in the interference images from Figure 4-7 (b,c). The second order field (B_{12}) is generated by following Path A from Figure 4-4. The incident light is right circularly polarised upon setting the fast axis of P3 parallel to P1 and isolated by setting the fast axes of P3 and P4 orthogonal. The intensity profile generated from the cascade process is presented in Figure 4-8(a). The circular polarisation incident upon the crystal is converted into a further optical vortex, increasing the topological order of the vortex present. This is evident in the interference measurement in Figure 4-8(b,c). The collinear interference measurement Figure 4-8(b) shows a double twist spiral of same handedness as the B_{11} field from (b). The wedge interference pattern Figure 4-8(c) reveals the presence of two extra fringes above the singularity indicating the presence of two 2π phase steps around the beam axis. The zero order field (B_{10}) generated from following Path B from Figure 4-4 is presented in Figure 4-9(a). The incident light is left circularly polarised upon setting the fast axis of P3 perpendicular to P1 and the resulting field is isolated by setting the fast axes of P3 perpendicular to P4. The left circular polarised light results in the absence of an optical vortex as the collinear Figure 4-9(b) and wedge Figure 4-9(c) interference patterns show.

The radial intensity profiles of Figure 4-7(a), Figure 4-8(a) and Figure 4-9(a) are compared with their theoretical intensity profiles in Figure 4-10, Figure 4-10 and Figure 4-10. Any slight misalignment of the beam incident on the optic axis of the second crystal will result in the formation of additional interference effects in the outer rings and thus we conclude that there is a high level of correlation between the theoretical and experimental intensity profiles. The cascade regime can

be reduced down to a single element wherein an incident beam with $\ell\hbar$ can be transformed into either a superposition of $\ell\hbar$ and $(\ell+1)\hbar$ or $\ell\hbar$ and $(\ell-1)\hbar$ per photon upon selection of the appropriate handedness of the polarisation to the handedness of the vortex. These polarisation controlled and separable beams could prove useful for the field of quantum information where different OAM states must be generated, manipulated and actively selected using polarisation optics forming the basis of an OAM optical circuit. Coupled with the previous work on the tunability of the OAM using elliptically polarised light, ICD provides a flexible method for the generation and control of the OAM per photon with high fidelity. Further investigation into this using ICD will require the generation of two photon entangled states using parametric down conversion [2-4,19].

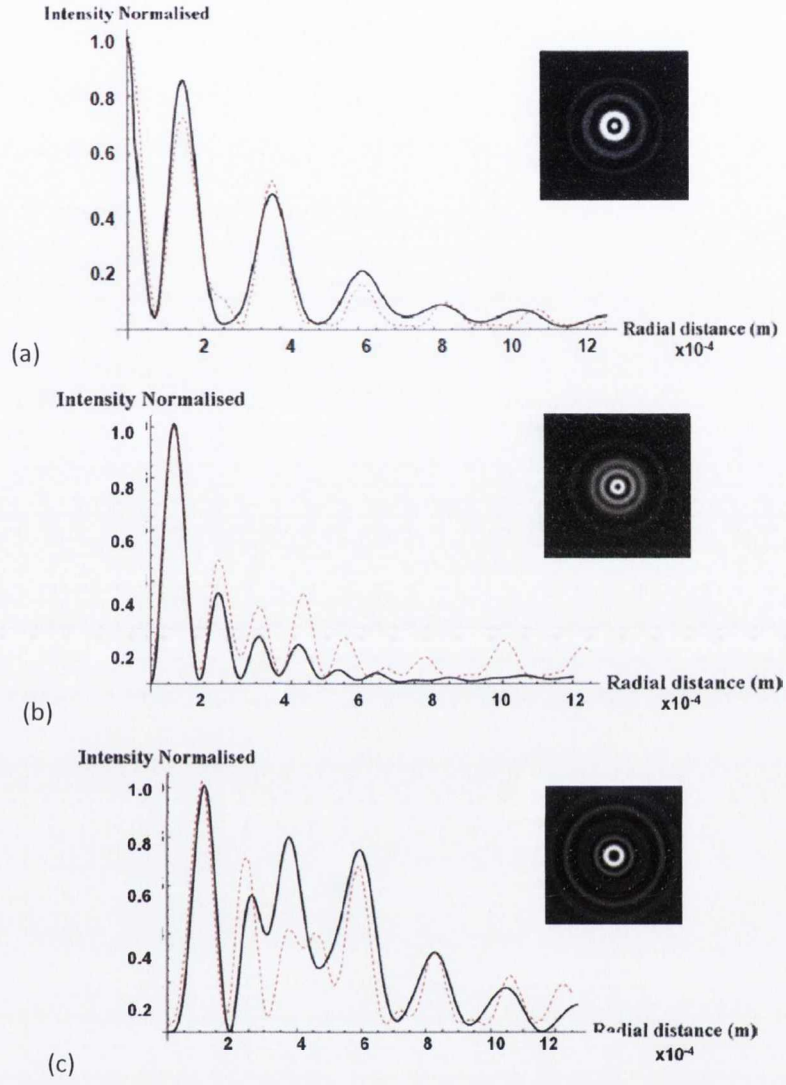

Figure 4-10: Radial intensity profiles of the experimental Figure 4-9 conical beams (red) (a) zero order B_{10} (b) first order B_{11} (c) second order B_{12} compared to theory (black). Theoritical intensity profile inset.

4.5 Rotation of biaxial crystals

Cascade ICD requires the propagation of conically diffracted light through subsequent biaxial crystals, with each crystal performing successive ICD transformations upon the incident beam. The relative angle between the crystals is given by ($\Delta\gamma$), however it is mathematically easier to keep the crystal optic axes aligned parallel to each other and rotate the incident beam through the angle α;

$$\mathbf{E}(\mathbf{R},z)=\mathbf{E}(R,\varphi,z)\rightarrow\mathbf{E}(R,\varphi-\alpha,z) \tag{4.19}$$

The polarisation vectors on the ring are rotated via the matrix,

$$\mathbf{R}(\alpha)=\begin{pmatrix}\cos\alpha & -\sin\alpha\\ \sin\alpha & \cos\alpha\end{pmatrix} \tag{4.20}$$

such that the new E field is described by the following set of rotations:

$$\mathbf{E}(\mathbf{R},z)=\mathbf{E}(R,\varphi,z)\rightarrow\mathbf{R}(\alpha)\mathbf{E}(R,\varphi-\alpha,z) \tag{4.21}$$

The beam incident on the first crystal is circularly symmetric and uniformly polarised. For the propagation of a beam through the 2nd biaxial crystal with geometric ring radius R_{02} the Fourier transform of the field after conical diffraction is,

$$\begin{aligned}&e^{ikP^2z}[\cos(kPR_{02})\mathbf{I}-i\sin(kPR_{02})\mathbf{M}(\theta)]\\&\times[\cos(kPR_{01})\mathbf{R}(\alpha)-i\sin(kPR_{01})\mathbf{M}(\theta)]a(P)\begin{pmatrix}e_x\\e_y\end{pmatrix}\end{aligned} \tag{4.22}$$

Thus the Fourier transform of the conically diffracted field upon rotation through angle α is given by

$$e^{-\frac{1}{2}ikP^2z}[\cos(kPR_1)\mathbf{R}(\alpha)-i\sin(kPR_1)\mathbf{M}(\theta)a(P)]\begin{pmatrix}e_x\\e_y\end{pmatrix} \tag{4.23}$$

In position space, this can be written and simplified to be;

$$\mathbf{E}(\mathbf{r},z)=(-in\mathbf{I}+B_{02}\mathbf{I}+B_{12}\mathbf{M}(\theta))+\mathbf{R}(\alpha)(in\mathbf{I}+B_{02}\mathbf{I}+B_{12}\mathbf{M}(\theta))\}\begin{pmatrix}e_x\\e_y\end{pmatrix}, \quad (4.24)$$

where

$$B_{02}\equiv B_{01}(2R_0,2z), \quad (4.25)$$

$$B_{12}\equiv B_{11}(2R_0,2z), \quad (4.26)$$

$$I_{in}=\int_0^\infty a(P)e^{ikP^2z}J_0P(kPR)dp. \quad (4.27)$$

The emergent-cascaded field is described by Eq.(4.24), defined by the relative rotation of the polarisation vectors by α. The resultant geometric ring radius R_0 is simply twice the first crystals ring radii, with a doubling of the optical path extension (Z). The first terms in (4.24) describe the superposition of the fields generated from the first crystal ($B_{02}\mathbf{I}+B_{12}\mathbf{M}(\theta)$), with twice the cone angle and ring radius as per equation (4.25) and (4.26). The second terms describe the electric field component due to the rotation of the crystal through (α) composed of the field generated from the first crystal, again with twice the cone angle and ring radius. Most notably both terms contain components of opposite signs that describe the initial generating field (I_{in}). When $\alpha = 0^0$ the rotational component is zero and the incident beam term ($-I_{in}$) is of zero amplitude. The resultant intensity profile at the beam waist is double the radius of the FIP from the first crystal. When $\alpha = 180^0$ the rotational component is at its maximum amplitude, and consequently the ($B_{02}\mathbf{I}+B_{12}\mathbf{M}(\theta)$) terms cancel between the two components leaving the original Gaussian beam. As (α) is varied from 0° to 180° degrees the distribution of intensity between the components varies as denoted by Eq.(4.28), where I_0 is the intensity of the incident beam.

$$I_{in}(\alpha)=\sin\left(\alpha/2\right)I_0 \quad (4.28)$$

If the incident beam is a circularly polarised Gaussian beam, the generated ring profiles are again composed of a superposition of orthogonally polarised zero- and first-order Bessel fields with a total OAM of $\ell = \frac{1}{2}\hbar$ per photon. The (I_{in}) component therefore describes the incident Gaussian beam with $\sigma = 1\hbar$ per photon. Varying the angle of the cascade process and therefore the intensity in each component consequently varies the total AM of the final field between both extremes.

4.5.1. Experimental procedure

The crystals used in the following cascade experiments are 20.98mm and 21.1mm in length. The resulting geometric ring radii at 532nm are 4.28 $x10^{-4}$ m and 4.31 $x10^{-4}$ m respectively, giving a combined R_0 = 8.59 $x10^{-4}$ m. The experimental setup is presented in Figure 4-11, where the second biaxial crystal BC2 is mounted so that it can be rotated about its optic axis without misalignment. The focusing lens L_1 is a 17cm lens forming a $1/e^2$ half width beam waist of 76 μm giving a ρ_0 value of 11.1. Taking into account the increased optical path length of the crystal (1.54cm) the FIP lies 20cm away from the L_1 lens. Initially the second biaxial crystal BC2 is removed and the FIP of the first crystal is imaged upon the CCD as the crystal is rotated through 360°. Using linear polarised light by removing the wave plate P1 enables the tracking of the FIP as the crystal is rotated. The polarisation is orientated such that the position of zero intensity on the ring is the position of tangential polarisation signifying the $\theta = 0°$ point. Secondly, BC2 is inserted and orientated such that the optic axes are parallel and $\Delta\gamma=0$, the crystals are aligned when the classic double ringed structure of the FIP is formed with no features or intensity at the centre of the ring. Intensity profiles are recorded on the CCD as BC1 is rotated through 180° degrees.

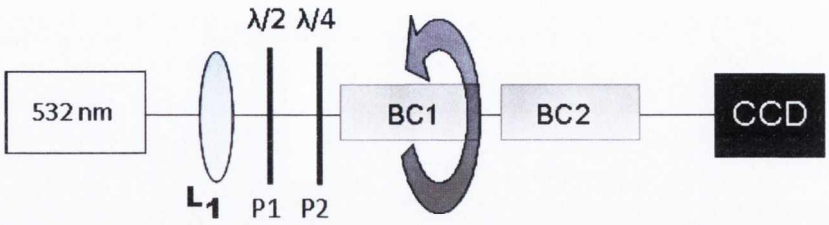

Figure 4-11: Experimental setup for cascade ICD where L_1 is a 17cm PCX lens and BC1 and BC2 are biaxial media. BC1 is mounted such that it can be rotated about its optic axis without misalignment.

4.5.2. Results and discussion

Figure 4-12 shows the intensity profiles of the FIP as BC1 is rotated through 360°. The ring of radius R_{01} rotates through a radius of $2R_{01}$. The intensity profile of the FIP of cascade ICD as BC1 is rotated through 180° is presented in Figure 4-13. When the crystals are aligned in parallel, the FIP of the cascade forms the classic double ring structure of 1.75mm in diameter. As the BC1 is rotated the Gaussian spot increases in intensity as the ring decreases in intensity. The Gaussian spot in the cascade ICP traces out the path of the Poggendorff ring from Figure 4-12 when α = 0°. The Gaussian beam is of zero amplitude when $\Delta\gamma$ is zero. The corresponding position of the Gaussian is the position of zero amplitude of α = 0° from Figure 4-12.

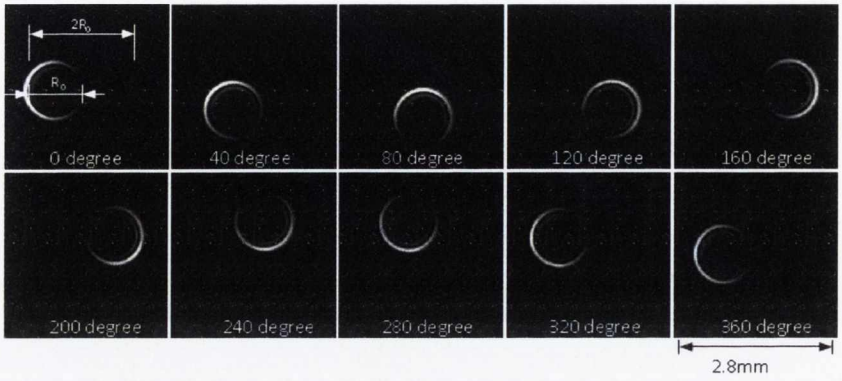

Figure 4-12: Intensity profiles of FIP of single 2.1cm a biaxial crystal when rotated through 360°.Linearly polarised light is used to show the rotation of the polarisation as the crystal is rotated.

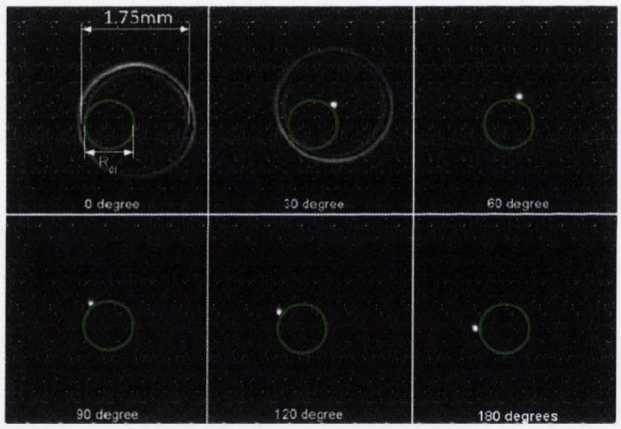

Figure 4-13: Experimental images of FIP of cascade ICD as BC1 is rotated through 180 degrees.

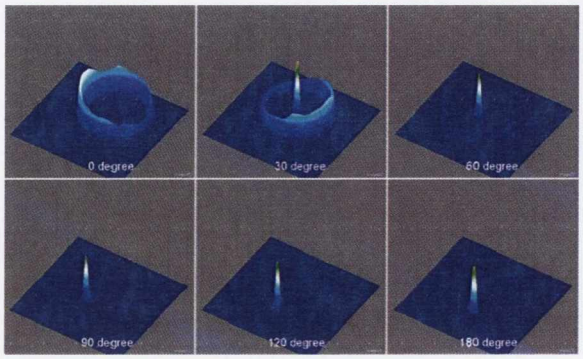

Figure 4-14: 3D intensity plots of FIP of Figure 4-13.

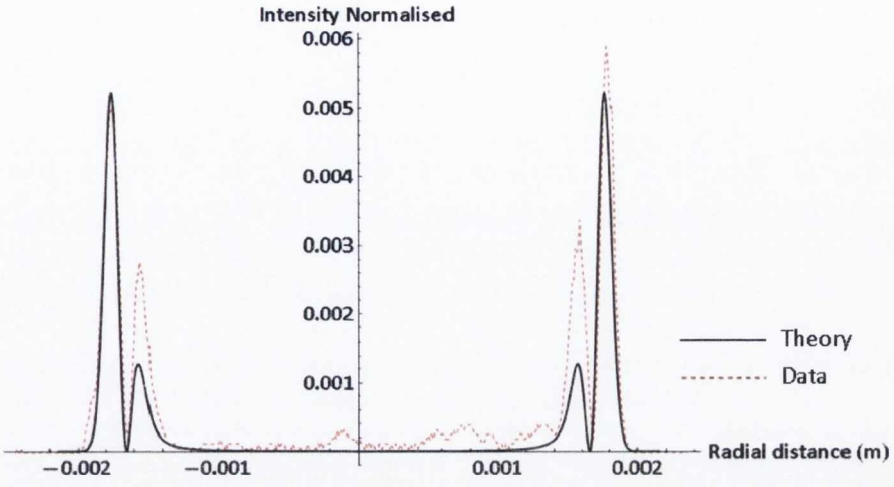

Figure 4-15: Line intensity plots for Figure 4-13 when $\Delta\gamma = 0°$. Theoretical (black) and experimental (red-dashed)

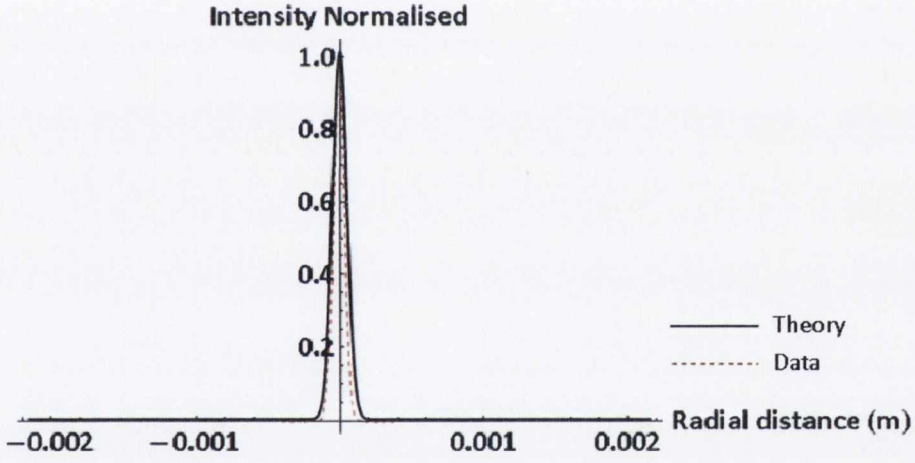

Figure 4-16: Line intensity plots for Figure 4-13 when $\Delta\gamma = 180°$. Theoretical (black) and experimental (red-dashed).

The radial intensity profiles of Figure 4-13 are shown in Figure 4-15 for $\Delta\gamma$ = 0° and in Figure 4-16 for $\Delta\gamma$ = 180°. There is a close correlation between the experimental and theoretical results particularly in Figure 4-15 were $\Delta\gamma$ = 0° and the Gaussian beam with the incident beam waist (w) 76 μm of is reformed Figure 4-16.

4.6 Conclusions

Using internal conical diffraction in a two biaxial crystal cascade together with some simple polarisation optics we have demonstrated the generation of optical vortices with topological charge of ±1 and ±2. We have also demonstrated raising and lowering of the order of an optical vortex, including the annihilation of an optical vortex of charge ±1. In principle, our two crystal experiment can be extended to n biaxial crystals to generate optical vortices with a maximum charge n, though there is 50% power loss for each successive cascade element added. Earlier work by King involved the manipulation of the charge of vortices using an axicon to transform a Gaussian beam into a non-diverging zero order Bessel beam before an ICD process. Our work achieves the same goal but demonstrates the direct transformation of a simple Gaussian laser beam.

A recent approach to the creation of beams with tunable OAM is to tune the SAM and then convert SAM to OAM, taking advantage of the ability to tune the SAM of light using standard optical components, which manipulate polarisation. The device that draws the biggest comparison to ICD is a device named "Q-plates". Recent publications on the conversion of SAM into OAM using Q-plates show the interest in such polarisation controlled devices in the fields of quantum optics and quantum communications [20-21]. Q-plates allow circularly polarised light with $\sigma = +1\hbar$ to be converted into a beam with $\ell = +2\hbar$ with a very high efficiency (up to ≈ 98%), but suffer from low beam mode quality [20]. It should be noted that the measure of efficiency in this sense refers to

the conversion of the incident SAM into OAM. It is also equally viable to attribute very high efficiency to a conically diffracted beam in the conversion of a circularly polarised Gaussian into Bessel beams of differing orders, with very high beam fidelity due in large part to the quality of the biaxial crystals available. The work performed in this thesis demonstrates a greater flexibility in the manipulation of the total OAM per photon over that presently published on "Q-plates". Over the previous two chapters the ability to transform and manipulate in a controlled manner the OAM to an integer or non-integer value of ħ per photon has been clearly demonstrated both theoretically and experimentally.

Cascade ICD using a pair of biaxial slabs of similar length with their crystallographic axes aligned parallel forms a beam with a new geometric ring radius of the combined R_0 values. Rotating one crystal 180° with respect to the other, reforms the initial Gaussian beam with its polarisation intact, effectively cancelling the ICD effect. The Gaussian beam reforms along the direction corresponding to the point $\theta = 0°$ when the crystals are parallel. Rotating one crystals through 180° rotates the Gaussian spot from the point of zero amplitude around the path of the Poggendorff ring of the first crystal with the intensity distribution between the rings varying as defined by Eq. (4.28). This ability to select the power ratio between the central Gaussian spot and the larger outer ring is exploited in the next chapter to generate a conically diffracting optical trap. The variations of power also varies the total AM in the cascaded beam between a pure OAM state of ½ ħ per photon and a pure SAM state of 1 ħ per photon, providing another means for the tuning of the total AM per photon.

4.7 References

1 M. V. Berry, "Conical diffraction from an N -crystal cascade," Journal of Optics **12** (7), 075704 (2010).

2 A. Vaziri, J. Pan, T. Jennewein, G. Weihs, and A. Zeilinger, "Concentration of Higher Dimensional Entanglement: Qutrits of Photon Orbital Angular Momentum," Physical Review Letters **91**, 227902 (2003).

3 S. S. R. Oemrawsingh, X. Ma, D. Voigt, A. Aiello, E. R. Eliel, G. W. tnbspHooft, and J. P. Woerdman, "Experimental Demonstration of Fractional Orbital Angular Momentum Entanglement of Two Photons," Physical Review Letters **95** (24), 240501 (2005).

4 L. Chen and W. She, "Increasing Shannon dimensionality by hyperentanglement of spin and fractional orbital angular momentum," Optics Letters **34** (12), 1855-1857 (2009).

5 G-H. Kim, HH. J. Lee, Jong-Uk Kim, and H. Suk, "Propagation dynamics of optical vortices with anisotropic phase profiles," Journal of the Optical Society of America **20** (2), 351-359 (2003).

6 J.C. Gutiérrez-Vega and C. López-Mariscal, "Nondiffracting vortex beams with continuous orbital angular momentum order dependence," Journal of Applied Optics A **10** (1), 015009 (2008).

7 S. M. Baumann, D. M. Kalb, L. H. MacMillan, and E. J. Galvez, "Propagation dynamics of optical vortices due to Gouy phase," Optics Express **17** (12), 9818-9827 (2009).

8 A. Abdolvand, K. G. Wilcox, T. K. Kalkandjiev, and E. U. Rafailov, "Conical refraction Nd:$KGd(WO_4)_2$ laser," Optics Express **18** (3), 2753-2759 (2010).

9 J. Hellström, H. Henricsson, V. Pasiskevicius, . U. Bünting, and D. Haussmann, "Polarisation-tunable Yb:KGW laser based on internal conical refraction," Optics Letters **32** (19), 2783-2786 (2007).

10 V. Peet, "Improving directivity of laser beams byemploying the effect of conical refractionin biaxial crystals," Optics Express **18** (19), 19566-19573 (2010).

11 A. J. Schell and N. Bloembergen, "Laser studies of internal conical diffraction. I. Quantitative comparison of experimental and theoretical conical intensity distribution in aragonite," Journal of the Optical Society of America A **68** (8), 1093 (1978).

12 A. J. Schell and N. Bloembergen, "Laser studies of internal conical diffraction. II. Intensity patterns in an optically active crystal, andagr;-iodic acid," **68** (8), 1098 (1978).

13 C. F. Phelan, D. P. O'Dwyer, Y. P. Rakovich, J. F. Donegan, and J. G. Lunney, "Conical diffraction and Bessel beam formation with a high optical quality biaxial crystal," Optics Express **17** (15), 12891-12899 (2009).

14 M. V. Berry, M. J. Jeffrey, and M. Mansuripur, "Orbital and spin angular momentum in conical diffraction," Journal of Optics A. (11), 685 (2005).

15 V. Peet, "Biaxial crystal as a versatile mode converter," Journal of Optics **12** (9), 095706 (2010).

16 T. A. King, W. Hogervorst, N. S. Kazak, N. A. Khilo, and A. A. Ryzhevich, "Formation of higher-order Bessel light beams in biaxial crystals," Optics Communications **187** (4-6), 407-414 (2001).

17 D. P. O'Dwyer, C. F. Phelan, Y. P. Rakovich, P. R. Eastham, J. G. Lunney, and J. F. Donegan, "Generation of continuously tunable fractional optical orbital angular momentum using internal conical diffraction," Optics Express **18** (16), 16480-16485 (2010).

18 S. Franke-Arnold, L Allen, and M. Padgett, "Advances in optical angular momentum," Laser and Photonics Review **2** (4), 299-313 (2008).

19 Li-P. Deng, H. Wang, and K. Wang, "Quantum CNOT gates with orbital angular momentum and polarisation of single-photon

quantum logic," Journal of the Optical Society of America B: Optical Physics **24** (9), 2517-2520 (2007).

20 E Karimi, B Piccirillo, E Nagali, L Marrucci, and E Santamato, "Efficient generation and sorting of orbital angular momentum eignmodes of light by thermally tuned Q-plates," Applied Optics **94** (23), 231124 (2009).

21 S. Straupe and S. Kulik, "Quantum optics: The quest for higher dimensionality," Nature Photon **4** (9), 585-586 (2010).

Chapter 5

CONICALLY DIFFRACTING OPTICAL TRAP

5.1 Abstract

Conical diffraction of linearly polarised light in a biaxial crystal produces a beam with a crescent-shaped intensity profile. Rotation of the plane of polarisation produces the unique effect of spatially moving the crescent-shaped beam around a ring. We use this effect to trap microspheres and white blood cells and to position them at any angular position on the ring. Continuous motion around the circle is also demonstrated. This crescent beam does not require an interferometeric arrangement to form it, nor does it carry optical angular momentum. The ability to spatially locate a beam and an associated trapped object simply by varying the polarisation of light suggests that this optical process should find application in the manipulation and actuation of micro- and nano-scale physical and biological objects.

This work resulted in the publication: *D. O'Dwyer, C. Phelan, K. Ballantine, Y. Rakovich, J. Lunney, and J. Donegan, "Conical diffraction of linearly polarised light controls the angular position of a microscopic object," Opt. Express 18, 27319-27326 (2010).*

5.2 Introduction

The seminal work by Arthur Ashkin, in which he demonstrated the first controlled manipulation of microscopic particles using a laser beam, has lead to revolution in the manipulation of micron and submicron particles some 20 years after its initial demonstration[1]. This new optical tool most often referred to as an optical tweezers has proved to be most invaluable in cellular biology and cold atom trapping. An experiment which exemplifies the sensitivity and accuracy obtainable using an optical trap is the direct observation of base pair stepping in RNA polymerase with a spatial resolution down to one Angstrom[2]. Optical tweezers have been used to trap dielectric spheres [3], viruses, bacteria, living cells [4], small metal particles [5] and strands of DNA [6].

Optical trapping arises due to the interaction of the linear momentum of light with matter. Light scattering off the surface of an object transfers momentum from the photon to the object, a process that is termed radiation pressure. Ashkin demonstrated that if a latex bead of several micrometers in diameter comes into the path of a focused laser beam the radiation pressure accelerates the particle in the direction of beam propagation but more importantly, he observed that the beads are pulled towards the high intensity point at the focus of the beam. The focusing of light generates a radial gradient of intensity, due to the difference in refractive indices between the particle and the medium and the particle is either attracted or repelled from the region of high intensity[7]. Ashkin also theorised and demonstrated atom cooling where a neutral atom could have the trapping light tuned to a specific optical transition of the atom[8-9]. Direct absorption of the photons is followed by a spontaneous emission event cooling the atom and reducing the average thermal velocity of the atom.

Ashkin also reported the first single beam gradient trap, for trapping in three dimensions with a single beam [10]. This requires a very steep

optical gradient and so requires the use of a high numerical aperture (NA) objective lens, which generates a near diffraction limited beam waist. This compensates for the radiation pressure pushing the particle in the beam direction. The 3D confinement of particles enables a particle to be suspended within the beam path regardless of the direction of the beam direction. The forces acting upon a trapped particle as a result of radiation pressure can be described in terms of either Mie or Rayleigh scattering. Particles smaller than the interacting wavelength, are in the Rayleigh regime and the particle acts like a dipole. The forces on the dipole are divided into a scattering component in the direction of the light and the gradient component pointing the direction of the intensity gradient of the light [11-12]. This type of trapping geometry is not examined in this thesis. The details of the different trapping theories will not be discussed here in detail but the reader is directed toward [13] for Mie and [14] for Rayleigh scattering.

The interaction of the angular momentum of light can under the correct conditions induce a rotation of a particle interacting with the trap. The controlled trapping and rotation of micron-sized particles is often referred to as an optical spanner [15]. Spin angular momentum (SAM) can be used to rotate transparent birefringent particles. The particles act like microscopic wave-plates changing the polarisation and imparting a torque to the particle. A beam with orbital angular momentum (OAM) possesses an azimuthal component to the Poynting vector. When such a beam is either absorbed by or scattered off a particle it imparts a lateral momentum component that causes the particle to rotate. Alternatively, particles may also be rotated or moved in a circle by using asymmetric intensity patterns shifting the equilibrium position of the trapped particle. This enables the controlled rotation of a particle as opposed to the continuous rotation that angular momentum transfer provided. Examples include rectangular apertures[16], Hermite-Gauss/Bessel modes [17] or SLM[18]. Another method for the generation of

a spatially structured light beam is via interferometry [19]. In this case a Laguerre Gaussian (LG) beam, with ℓ = 2 or 3, was interfered with a Gaussian beam to produce a beam with 2 or 3 lobes. Adjusting the relative optical phase between the LG and the Gaussian beams leads to azimuthal rotation of the lobed intensity profile. An object trapped in one of the lobes is dragged along and thus circulates around the beam axis. A clear advantage of this scheme over approaches requiring the transfer of orbital angular momentum is that absorption of the light is not required. The ability to control the rotation of microscopic particles adds a new degree of freedom to the trapping regime. This ability has been exploited to accurately position irregular shaped particles, generate flow chambers and provide insights into picoliter viscometry in cells[20] or to optically drive micro machines such as micro pumps and micro stirrers [21-22].

In this chapter, various optical trapping geometries whose foundation is laid out in the previous chapters are explored. The basic arrangement is the formation of a simple ring shaped trap from a single biaxial crystal, whose mode of momentum (both linear and angular) transfer is determined by the careful selection of the incident polarisation and beam profile. In conical diffraction, circular incident polarisation generates a circularly symmetric intensity profile with 0, 1 or ½ $\hbar$ OAM per photon, which can be transferred to the particles setting the particles in continuous motion. Linear incident polarisation generates a crescent shaped intensity profile, with the position of the maximum intensity determined by the orientation of the linear polariser. A particle will then be opticaly confined in this region and can be simply and accurately positioned on a circle by controlling the plane of polarisation of the input beam. Setting the linear polarisation in continuous rotation, the particle will be set into circular motion, mimicking the rotation due to OAM transfer except that no scattering or

absorption off a particle is required. Using cascade conical diffraction more a compound optical trap is demonstrated.

5.3 Principles of optical trapping-ray optics

For dielectric spheres whose diameter is large compared to the wavelength of light a simple geometric ray optics approach can be used to describe the interaction of light refracting. A single beam gradient optical trap is formed by tightly focusing a laser beam with an objective lens of high numerical aperture (NA). A dielectric particle near the focus will experience a force due to the transfer of momentum from the scattering and reflection effects.

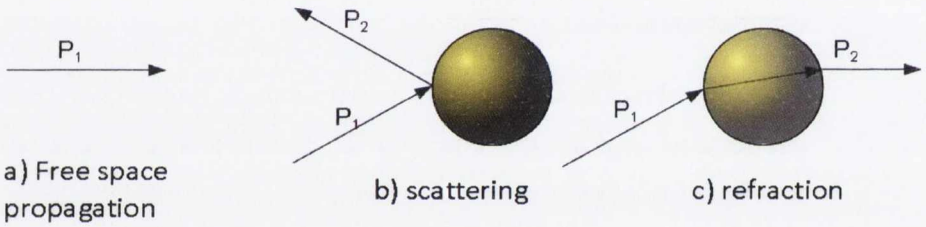

Figure 5-1: (a) Momentum is invariant under free space propagation. (b) Momentum changes upon scattering off surface. (c) Momentum is also changed upon refraction.

The resulting optical force can be decomposed into two components: a scattering force (F_s) in the direction of light propagation and a gradient force (F_g), in the direction of the spatial light gradient. Incident light impinges on the particle from one direction, but can be scattered in a variety of directions, while some of the incident light may also be absorbed. As a result, there is a net momentum transfer from the incident photons to the particle. In most regimes, where the light is not tightly focused the scattering force dominates over the gradient force F_g as the electric field gradient across a particle is negligible.

However, if there is a steep intensity gradient (i.e., near the focus of a laser), the second component of the optical force, the gradient force, must be considered. The gradient force is proportional to the optical intensity gradient at the focus. For stable trapping in all three dimensions, the axial gradient component of the force pulling the particle towards the focal region must exceed the scattering component, the force pushing it away from the focus. This condition necessitates a very steep gradient in the light, produced by sharply focusing the trapping laser beam to a diffraction-limited spot using an objective of high NA. As a result of this balance between the gradient force and the scattering force, the axial equilibrium position of a trapped particle has been shown to be located slightly beyond (i.e., down-beam from) the focal point[14]. For small displacements, the gradient restoring force is simply proportional to the offset from the equilibrium position, i.e., the optical trap acts as a spring whose characteristic stiffness is proportional to the light intensity. The force on the sphere, given by the rate of momentum change, is proportional to the light intensity. When the index of refraction of the particle is greater than that of the surrounding medium, light is refracted towards the normal and resulting optical force is in the direction of higher intensity gradient. Conversely, for an index lower than that of the medium, light is refracted away from the normal imparting a force in the opposite direction to the intensity gradient [23].

The system is orientated such that light is propagating in the +z direction and the focus lies in the x-y plane. The scattering force in this system always imparts a force in the +z direction to the particle. The lateral gradient force lies in the x-y plane. A particle interacts with a beam of light such that the there is a gradient of intensity across the surface of the sphere so that there will be a greater momentum transfer on the side of greater intensity. The rays F_{g1} and F_{g2} from Figure 5-2(a) depict the differing magnitude of momentum transfer across the sphere

resulting in a greater net momentum transfer for ΔF_{g2} in the direction of the gradient, pulling the particle towards the point of highest intensity.

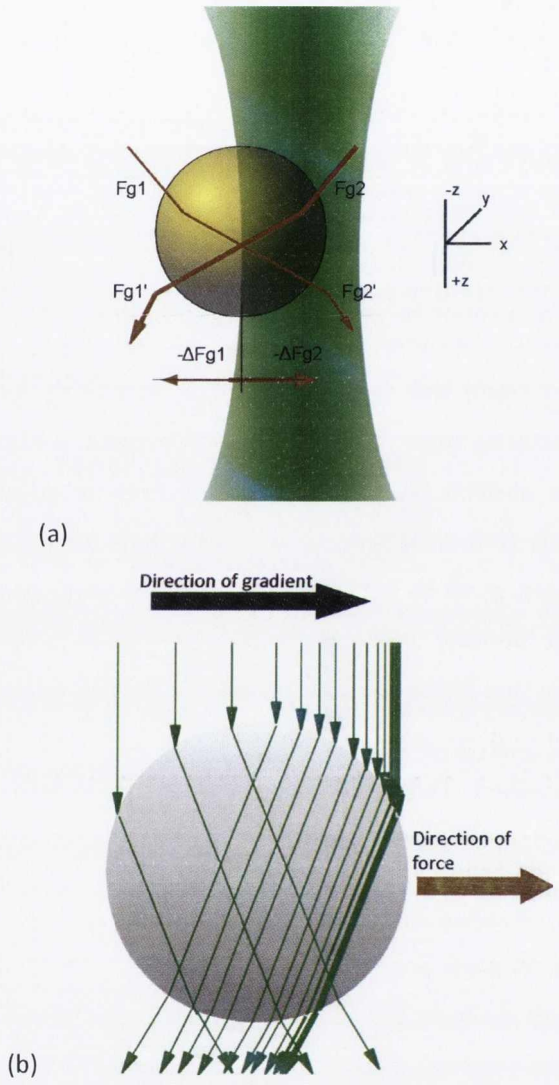

Figure 5-2: Gradient force acting on particle. (a) Lateral displacement of particle in x-y plane form the centre point of Gaussian peak intensity. The net force $-\Delta F_{g2}$ pulls particle towards the point of peak intensity. (b) Along the direction of the optical gradient, more rays are refracted through the sphere pulling the sphere towards the point of highest intensity.

The restoring force along the ±z direction is called the axial gradient force; this can impart a force either along or against the flow of photons. A schematic of the axial forces acting on a particle displaced below the focus is shown in Figure 5-3 and above the focus in Figure 5-4. These figures do not take into account the fact that part of the incoming light is partially reflected rather than refracted providing the scattering force. The vector sum of the net change of momentum given by ΔF_{g1} and ΔF_{g2} gives a restoring force towards to beam focus.

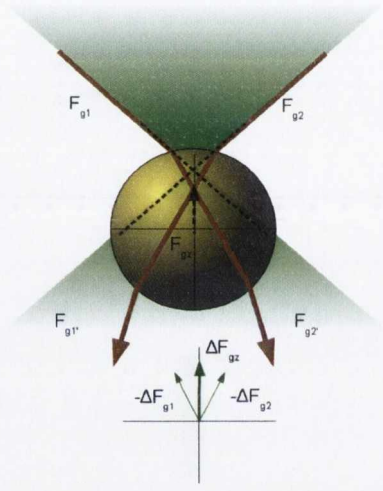

Figure 5-3: Axial gradient force acting on a particle downstream from focus, high intensity point at focus pulls particle towards focus.

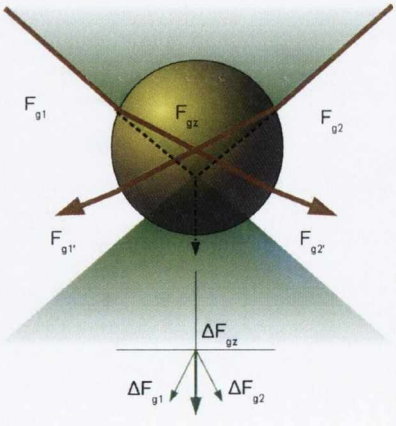

Figure 5-4: Axial gradient force acting on a particle upstream from focus. Particle is pulled down towards. Equilibrium point is just below focus

The reflected (or backscattered) component of the on-axis rays gives rise to the scattering force and exerts a force on the particle in the direction of beam propagation. The scattering force cans also be termed radiation pressure, where the photon momentum is transferred to the particle and is always in the direction of the propagation of the beam. This results in the particle being pushed downwards, away from the beam focus. An object is stably trapped if the scattering force along the +z-direction is compensated by the gradient force along the –z-direction. The greater the angle the rays of light make with the surface of the sphere the greater the lateral trapping as the optical gradient is greatly increased. The higher the NA of the objective the greater the optical gradient and stronger the restoring force, requiring a lower optical power to overcome the scattering effect. For a Gaussian beam the point of highest intensity lies at the centre of the beam axis. This results in the extreme ray contributing to the gradient force being much less intense than the centre of the beam. The equilibrium position is reached when the scattering force and gravity (which both act to push/pull the sphere downwards) is balanced by the axial gradient force (which pushes the sphere upwards).

5.3.1. Trap efficiency

The maximum force that the optical trap can exert will typically be of the order of pico-Newtons. The trapping efficiency of any optical tweezers is described in terms of the dimensionless Q parameter. This is the fraction of momentum transferred to the object from the trapping laser beam and is related to the trapping force F_{trap} via Eq. (5.1), where the trapping force F_{trap} is given by the power of the laser P, n is the ratio of the refractive index of the medium to the confined particle and c is the speed of light.

$$F_{trap} = Q\frac{nP}{c} \tag{5.1}$$

The force on a spherical particle of radius r_p can be calculated using the viscous drag exerted by moving the particle at a constant velocity in a fluid of viscosity η using the Stokes-Navier equation. The velocity at which the viscous drag exerted upon the particle overcomes the trapping force gives the escape velocity v_e:

$$F_{trap} = F_{drag} = 6\pi v_e r_p \eta \tag{5.2}$$

The critical velocity of the trapped particle scales linearly with the laser power in the optical trap. Possible values of Q range between 0 and 2. A Q value of 1 corresponds to all of the momentum being transferred to the particle. Optical tweezers configurations can be assessed experimentally to determine the Q values for trap efficiency in the lateral and axial directions. For optical forces acting on small dielectric particles Q values tend to be in the range 0.03 to 0.1 [24].

5.3.2. Annular or ring shaped optical traps

The transformation of a Gaussian or higher order mode into an annular ring shaped profile can be achieved with the use of a lens and axicon combination. A beam focused through an axicon forms an annular ring of light of radius r_a at the focus as in Figure 5-5[25].

$$r_a = (n-1)\beta f, \tag{5.3}$$

where n is the refractive index of the axicon, β is the cone angle of the axicon and f is the focal length of the lens. Like the conical refraction beam, the transverse intensity profile of the annular ring depends upon the ratio of r_a to the beam waist formed by the lens w_0. Changing the incident intensity profile to be a high order LG mode still produces an annular ring at the focus but with a corresponding OAM per photon.

Modifying the OAM of the ring requires the generation of the OAM elsewhere in the optical setup. The shape of the intensity profile around the ring can be manipulated using an interferometer as in [19] or with use of an aperture. We aim to propose the formation of a ring trap based upon ICD whose phase and intensity profile can be controlled using polarisation optics.

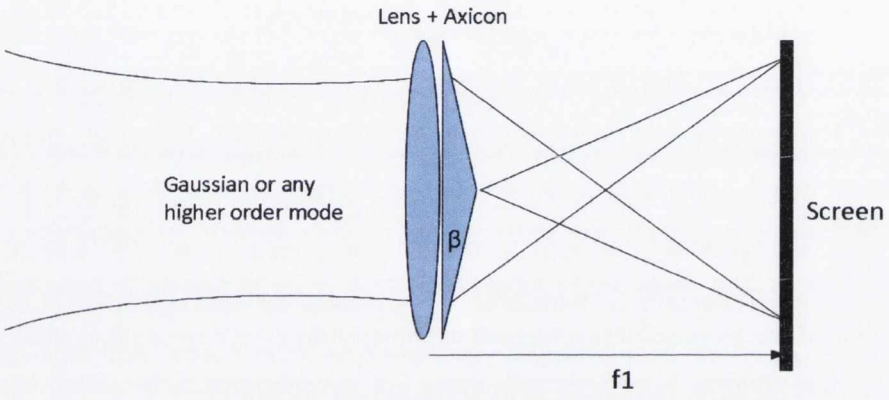

Figure 5-5: Formation of an annular ring using an axicon-lens combination. A Gaussian beam focused through an axicon will form a ring of light on the screen at a distance equal to the focal length of the lens.

Hollow ring shaped optical traps interacting with a single particle with a diameter greater than the ring provide the maximum trapping efficiency in the x-y plane. All of the intensity is contained within the rings providing the greatest angle of incidence for the refracted rays with respect to the sphere. The lack of intensity on axis however reduces the gradient along the ±z direction providing a weaker trap in these directions. This is counteracted by using a ring beam with a central axial beam to increase the trap strength along this direction. This ring and axial beam is one of the hypothetical traps put forward by Ashkin that provides an 3D optimal trapping efficiency at lowest power [26]. Annular

or ring beams have been used in optical trapping to measure the chemotaxis of sperm [27] and other biological samples, and have been proposed to be useful in cold atom trapping [25].

5.3.3. Rotation of optically trapped particles

The 3D optical confinement of a trapped particle is important for the spatial positioning of a particle relative to the surroundings, enabling the user to position the particle at any required location. The rotation of a particle within the confines of an optical trap in a controlled way can play a major role in the understanding of biological motors, light driven motors and micro-viscometry[20]. There are two distinct approaches for the rotation of particles, the manipulation of the geometry of the trapped particle to exploit an asymmetric force or the manipulation of the light interacting with the particle via either a modification of the intensity profile or with angular momentum.

5.3.4. Asymmetric trapping force

The rotation of a trapped particle can be achieved using the scattering force by either having an asymmetric intensity profile or having an anisotropic shaped particle. The controlled rotation of a particle was initially demonstrated by using an asymmetric trapping profile, thus exerting a torque on the particle [28]. A Hermite-Gauss beam, which is not azimuthally uniform in intensity, is used to rotate a trapped red blood cell. Alternatively, a micro fabricated cog or propeller will interact with a uniform intensity profile. The light is scattered of the irregular shape in different direction depending on the profile of the object. In this manner one can expect a windmill/propeller shaped object to

rotate, with the photons replacing the wind [29]. Devices like this are the main building tools for micro motors and gears, which are produced by light via two photon polymerisation and then optically driven [30]. A biological application of the asymmetrical scattering off a trapped particle is the detection of the malaria parasite in red blood cells. Healthy haemoglobin is easily distorted and when placed in a gradient trap the transfer of linear momentum rotated the particle up to hundreds of rpm. Infected blood cells are rigid and are not as easily distorted and do not rotate enabling the distinction[31].

5.4 Angular momentum transfer

A much more common approach is the transfer of AM to an absorbing or birefringent particle. The total angular momentum of light is the sum of spin and orbital components in units of ħ per photon. The mode of momentum transfer between SAM and OAM can under the right conditions differ in nature. The polarisation of an electric field is always intrinsic, such that the SAM σħ remains the same irrespective of which part of the beam a particle interacts with. This is not always the case for the OAM as the OAM per photon depends upon the axis about which the beam rotates leading to different types of rotation. Berry showed [32] that the orbital angular momentum can be considered both intrinsic and extrinsic.

5.4.1. Spin angular momentum

The microscopic equivalence of Beth's experiment for the observation of the SAM of light is the optical confinement of micron sized birefringent particles. A birefringent particle such as calcite confined in a circularly polarised beam will convert the polarisation from circular to linear and due to the conservation of momentum, a corresponding torque is exerted on the particle. Whereas in Beth's experiment the rotation was measured via the torque on a quartz string, in an optical trap, the particle spins on its axis. The rotational rate is

proportional to the incident SAM and power and rotation frequencies of a few hundred hertz have been observed [33]. SAM can also be transferred to a birefringent particle using linearly polarised light the particle can be rotated by rotating the direction of linear polarisation[34].

5.4.2. Orbital Angular Momentum

The transfer of OAM to a trapped particle requires the transverse linear momentum to rotate the particle. The OAM of light is due to an azimuthal component of the Poynting vector, when light is absorbed the lateral component exerts a torque on the particle and rotates it. The transfer of OAM to a particle may be either intrinsic or extrinsic. If the particle radius is larger than the trapping beam transverse profile the momentum transfer is said to be intrinsic and the particle rotates around its own axis, the momentum transfer is proportional to the total angular momentum ,$(\ell+\sigma)\hbar$ per photon[15], and the SAM and OAM components are indistinguishable. If the particle is smaller than the transverse profile the momentum transfer mechanism changes. The OAM transfer results in the orbiting of the particle around the path of the beam. This extrinsic transfer of AM to the particle is solely proportional to the OAM of the beam per photon[35-36]. Scattering of light off small particles induces momentum recoil. For a tightly focused annular beam with OAM, the dominant component of the scattering force lies in the direction of beam propagation. The gradient force confines the particle within the region of high intensity, but since the beam has a radially symmetric intensity profile the particle is not azimuthally constrained. As a consequence the particle is confined off the beam axis. The inclined helical phase fronts and corresponding azimuthal component to the momentum result in a tangential force when scattering off or absorbed by a particle. This induces a rotation in the plane perpendicular to the direction of the beam propagation. The

lack of azimuthal constraint results in the tangential force pushed the particle around the annulus of intensity. The necessity for a particle to be absorptive or to partially scatter the light to experience OAM transfer inhibits the usefulness of this method for the rotation of particles. A balance must be achieved such that it is transparent enough for positive tweezing to occur (attracted to intensity maxima) and yet has the ability to undergo OAM transfer.

5.4.3. Intensity shaped beam rotation

Displacing the position of the optical trap relative to the trapped particle removes the particle from its equilibrium position. If the displacement is small enough for the particle to still experience the light field and the gradient is strong enough to overcome the viscosity of the suspending, medium the particle will realign itself with the new position of the trap. This displacement of the position of the trap can be achieved mechanically by displacing the sample relative to the beam[37], or using apertures to shape the beam profile [16-17]. Digital spatial light modulators (SLM's) are used to create dynamic optical traps that can generate a spatial array of traps or have a spatial trajectory for the beam within the trapping cell [38-39]. An alternative method put forward by Paterson et al. [19] is based on the controlled rotation of the spiral interference patters of a LG mode with a Gaussian plane wave. The interference pattern forms a lobed shaped pattern whose number of lobes depends upon the topological order of the LG mode used. The position of maximum intensity maxima is adjusted by changing the relative phase difference between the two arms rotating the lobes. The relative shift in phase between the arms of the interferometer that rotates the lobes leaves the trap susceptible to vibrations also changing the optical path length of the arms. This interferomtric instabity is

something we aim to address by exploiting the polarisation dependent intensity profile of the conical beam.

5.5 Conically diffracting annular optical trap

The previous chapters have presented an array of various intensity and phase distributions present in a conically diffracted beam that depend upon the incident polarisation and relative crystal orientations. Each of these can be exploited to provide a versatile and simple optical trapping arrangement encompassing angular momentum transfer off a the surface of a low quality particle and the formation of an intensity shaped gradient mimicking the angular momentum transfer to transparent non-absorptive particles.

A conically diffracted beam generated from linearly polarised light produces a crescent shaped intensity profile around R_0 with the point of maximum intensity diametrically opposed to a point of zero intensity with an intensity gradient that varies as $\cos^2(\theta/2)$ around the beam axis.

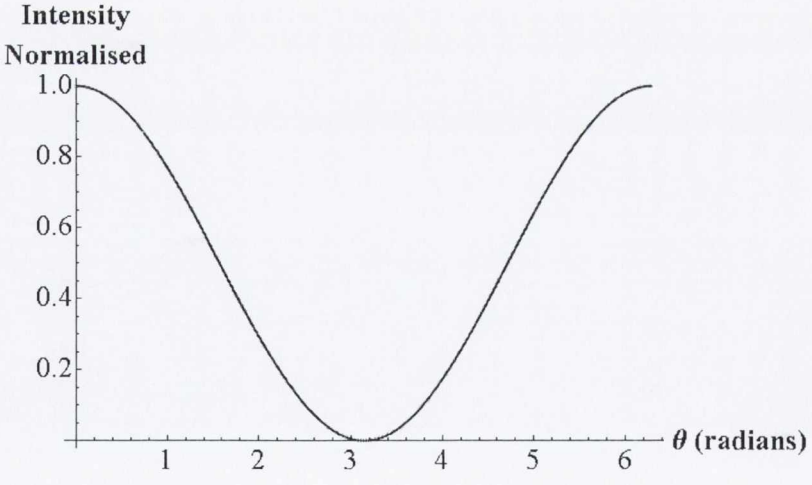

Figure 5-6: Normalised intensity around the beam axis (θ) showing a $\cos^2(\vartheta/2)$ dependence.

The position of peak intensity depends directly upon the orientation of the linearly polarised light incident upon the crystal. Rotating the orientation of the light with use of a half-wave-plate rotates the point of maximum intensity through x4 the angle of the wave-plate. Displacing the position of maximum intensity displaces the equilibrium position of a trap relative to a trapped particle. Expanding this into the cascade regime enables the rotation of the crescent beam around a central Gaussian spot with the same rotation mechanism.

5.5.1. Optical trapping setup

The general experimental setup is depicted in Figure 5-7, with the dashed box signifying the section that changes for each of the following trapping arrangements. The source is a frequency doubled Nd:YAG linearly polarised laser operating at a wavelength of 532 nm. The light is focused along the optic axis of the biaxial slab using a focusing lens L_1 (which changes depending upon the experiment). The refractive indices of the biaxial slab of $KGd(WO_4)_2$ at 532nm are n_1=2.031, n_2=2.063 and n_3=2.118, giving cone angle of A = 1.16 degrees. A second lens L_2, with a focal length (f_2) of 22 cm, is positioned at its focal length away from the FIP, collimating the beam. The beam is then directed into Leitz microscope configured into a top down illumination scheme, with internal beam-splitter replaced with a dichroic mirror, giving 99.98% reflection at 532 nm. A white light source positioned under the sample provides illumination for the C-mounted CCD camera

on top of the microscope. The objective used is a Leitz NeoPlan Flourtar x100 0.9NA infinity corrected objective with a focal length (f_3) of 1.81 mm. The radius of the ring in the trapping plane (R_t) is the geometric ring radius (R_0) times the demagnification factor, which for this system is .0082 as per Eq.(5.4),

$$R_t = \frac{f_3}{f_2} R_0. \tag{5.4}$$

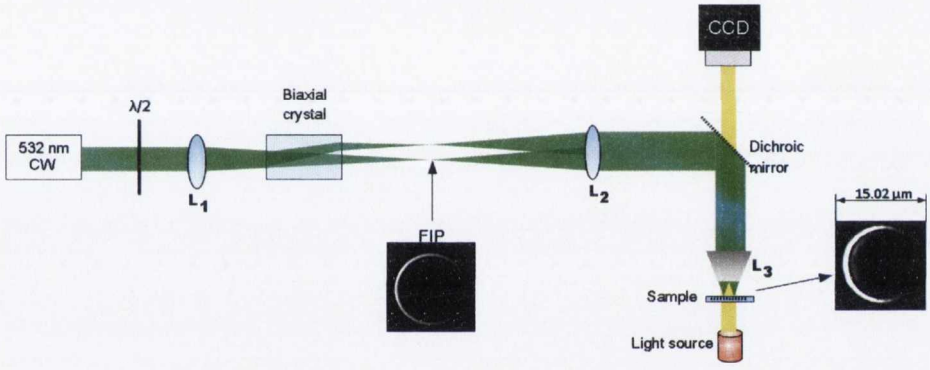

Figure 5-7: Standard top down conical diffracting optical trap. Source is a 532nm Nd:YAG linearly polarised laser. L_1 = 10cm focusing lens, L_2 = 22cm collimating lens, L_3 x100 infinity corrected objective imaging lens. Dashed line signifies the adjustable conical setup.

The two different types of latex spheres used in the following experiments are either Melamine Formaldehyde (MF) with a refractive index of 1.68 giving an *n* value relative to the refractive index of water of 1.24 or Polystyrene with a refractive index of 1.55 giving a *n* value of 1.15. The particles are suspended in a Millipore water solution and have diameters of 2.8 and 5.3 µm. A sample is prepared by sealing a drop (approx 80 µL) of solution between two microscope cover slips with a

1mm spacer and Vaseline to prevent leakage. A microscope slide acts as a base plate to make changing of the sample easier and to provide rigidity to the sample.

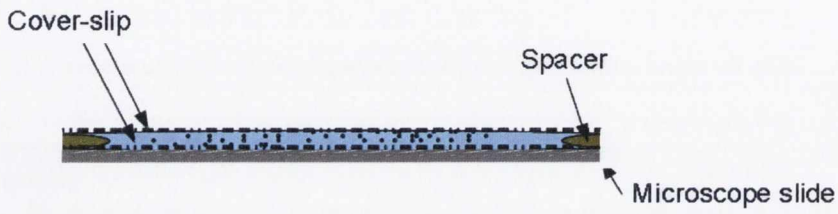

Figure 5-8: Sample holder. Approximately 80μL of particle solution is sealed between two 0.18mm glass cover sips.

5.6 Single crystal trap

The following set of experiments present a conically diffracting optical trap using a single biaxial crystal 3cm in length. The geometric ring radius $R_0 = 6.13 \times 10^{-4}$ m forms an R_t of 5.25 μm in the focal plane of the objective. The L_1 lens used is a 10cm DCX lens focussing the light to a $1/e^2$ beam waist size of 80μm. This gives a ρ_0 value of 7.7 and a FIP position 11.54 cm away from L_1 due to the increased optical path length of 1.54cm.

5.6.1. Circular polarisation

The optical arrangement for the formation of a circularly symmetric conical trap is shown in Figure 5-9. As in previous experiments a half wave-plate P1 is used to set the linear polarised light at 45 degrees to the quarter wave-plate fast axis. The conical diffraction

of circularly polarised Gaussian beam generates a circularly symmetric intensity profile with two orthogonally polarised states of 0 and 1ħ OAM per photon in superposition, with a net OAM of ½ħ OAM per photon. As before, the isolation of the zero- and first-order beam profiles requires a wave-plate and polariser combination (P2 & P3) and is only inserted into the beam path if required. The arrangement for the isolation of the respective fields is outlined in of Section 2.1.2.

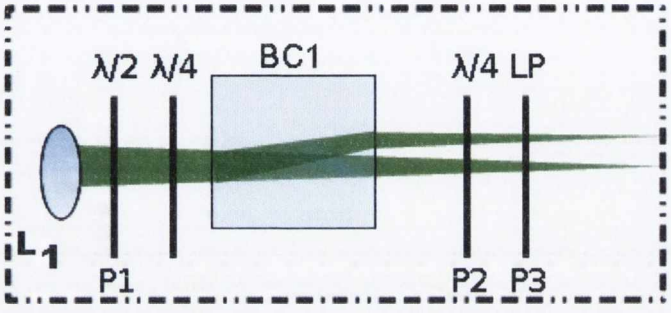

Figure 5-9: Experimental setup for single crystal arrangement with circularly polarised incident light. The polarisers P2 and P3 are only required when the zero and first order beams need to be isolated.

Figure 5-10(a) shows the circularly symmetric intensity profile imaged on the optical bench. Figure 5-10(b) shows 5.3 μm PS particles trapped around the circumference of the ring, with a minimum trapping power of 7mW in the trapping plane required for trap the particles. Figure 5-10(c) show 2.8 μm MF particles trapped around the circumference of the ring, with a minimum trapping power of 14mW in the trapping plane required for the.

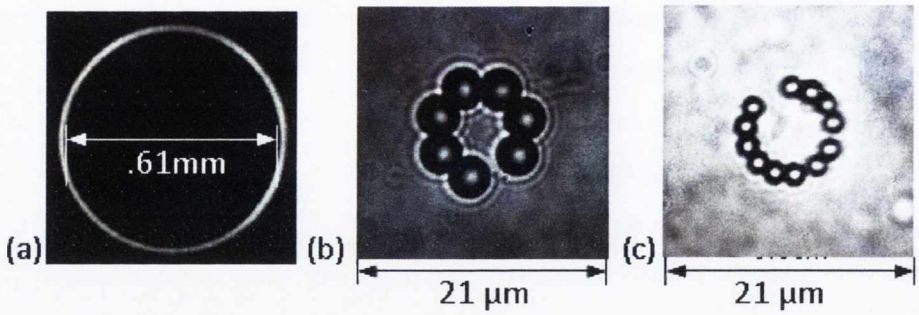

Figure 5-10: (a) Image of the conical beam on the optical bench. (b) 5.3 µm Polystyrene spheres trapped around the circumference of the ring (c) 2.8 µm Melamine Formalhyde trapped around the circumference of the ring.

The circulation of particles due to OAM transfer requires the particle to be either weakly absorptive or provide strong enough scattering, and therefore the above transparent particles are not suitable. To this end, calcite fragments of approximately 5 µm long were prepared from a sample of finely ground calcite.

Figure 5-11 shows a sequence of images of a rough 5 µm calcite fragment of the orbiting around the beam axis of the conical ring trap having ½ ħ OAM per photon. At 160 mW optical power the calcite fragment rotated at 0.32 Hz when illuminated by the conical beam ½ ħ OAM per photon. Isolating the first order beam with 1ħ OAM per photon at a loss of half the optical power to 80mW the particle rotated at a steady 0.34Hz, twice the rate for a given power of the full conical beam. No circulation is observed for the calcite particle when it is confined in the isolated zero order profile, as no OAM is present. This circulation rate is exceptionally low; rotation rates of hundreds of hertz would have been expected for such a high incident power. Such a large discrepancy in rotational frequency between the expected and observed values leaves the demonstration of the OAM transfer to the calcite

particles as inconclusive. The average circulation speeds for the calcite did correspond to the magnitude of the OAM in the incident beam indicating that some (albeit very inefficient) OAM transfer did take place.

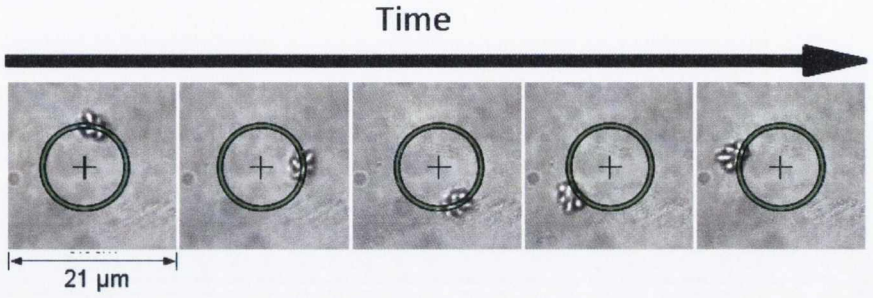

Figure 5-11: Selection of frames of a calcite fragment circulating around a ring 10 μm in diameter due to the transfer of OAM from the conical first order beam. Particle circulates at about 0.2Hz 60mW.

5.6.2. Linearly polarised incident light

The conical diffraction of linear polarised light forms a $\sin^2(\theta/2)$ gradient of intensity around the beam axis, Figure 5-12. The position of maximum intensity on the ring corresponds to the orientation of the plane of polarisation of the generating field, with the point of zero intensity on the diametrically opposite point on the ring corresponding to the point of orthogonal polarisation. Rotating the plane of the linear polarisation through $\pi/2$ rotates the position of maximum intensity on the ring through π around the beam axis. The polarisation incident on the biaxial crystal is changed with use of a $\lambda/2$ plate, the angle of the wave-plate fast axis (α) and thus the position of the intensity maxima/minima around R_0 is changed by rotating the wave-plate via a mechanically driven rotating mount positioned before the crystal.

(a)  (b) 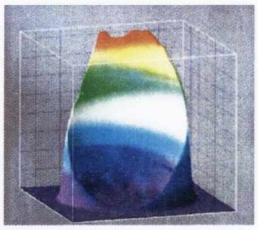

Figure 5-12: (a) Linearly intensity profile in conical refraction (b) 3D plot of intensity of intensity showing gradient around the ring.

As the wave-plate is rotated through α, the maxima/minima rotate through 4α. Figure 5-13 demonstrates the angular positioning of a 5.3 μm PS particle on the ring with the particle position corresponding to the angle of the fast axis of the half-wave-plate. Continuous rotation of the wave-plate sets the position of maximum intensity into continuous rotation dragging the particle around the path of the beam. The maximum circulation speed for the 5.3 μm for a given power enables the determination of the escape velocity (v_e) and hence the determination of the maximum trapping force along the direction of the gradient. For a known trap diameter of 10.5 μm, the maximum trapping force is determined using Eq. (5.2). Stable rotation is defined as the particle smoothly rotating with the trap, if the trap rotates faster than the restoring force of the gradient acting upon the particle the particle will leave the trap and no longer circulate. A maximum circulation frequency of 1.2 Hz was achieved for 118mW in the trapping plane. The maximum trapping force radially out from the centre of the ring is determined by the linear translation of the trap at a constant velocity for a given power. A maximum value of the trapping force of 2pN is experienced in the radial direction with a corresponding trapping force of ≈ 1pN for circular motion. Figure 5-14 shows the linear relationship between the optical power in the trapping plane and the maximum trapping force exerted and maximum speed on the particle.

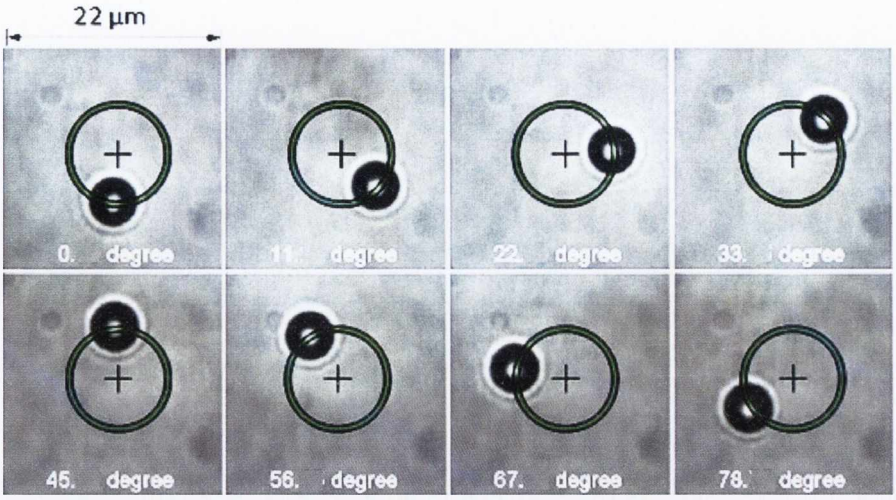

Figure 5-13: Sequence of images for the angular positioning of a 5.3 µm Polystyrene particle on a ring.

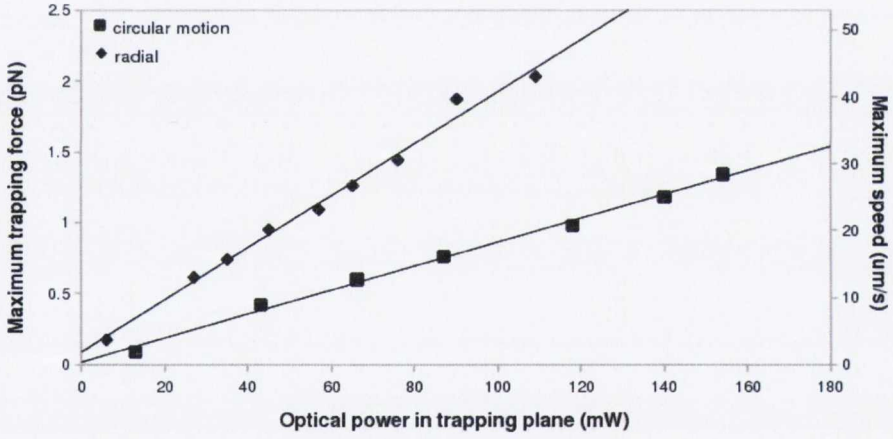

Figure 5-14: Dependence of maximum trapping force and speed versus optical power.

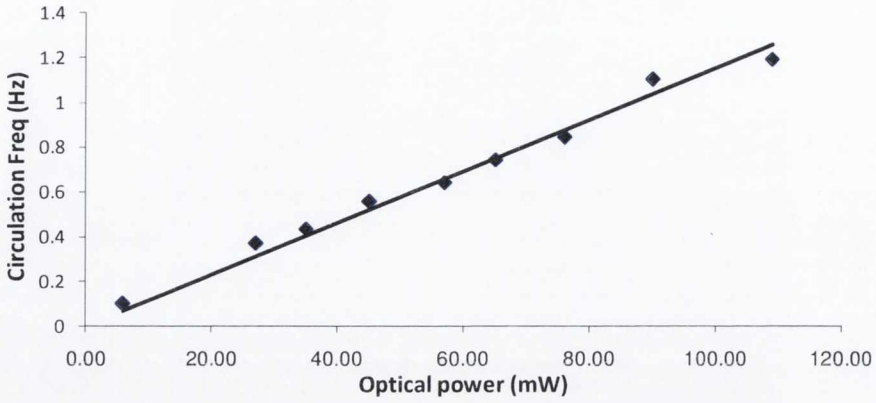

Figure 5-15: Linear regression plot (solid black line) maximum circulation frequency of particles as a function of optical power in trapping plane.

Figure 5-16 (a) shows a sequence of frames from the continuous rotation of a cluster of 5.3 μm MF stuck together. The outer three particles rotate around the centre particle which is not interacting with the trap (i.e. it does not see any of the light). Figure 5-16 (b) shows the optical confinement and subsequent circulation of a Neutrophil (white blood cell). The buffer solution was just PBS phosphate buffered saline. Neutrophils are the most common type of white blood cell, comprising about 50-70% of all white blood cells. They are phagocytic, meaning that they can ingest other cells, though they do not survive the act. Neutrophils are the first immune cells to arrive at a site of infection, through a process known as *chemotaxis* and are approx 8 microns they are circular with a granulated nucleus.

5.7.1. Linear polarisation

The experimental setup for a cascade ICR with linear polarised light is presented in Figure 5-17. The intensity profile presented in Figure 5-18 showing the Gaussian plus ring with a $\sin^2(\theta/2)$ intensity gradient when BC2 is rotated 80^0 degrees with respect to BC1. As in section 5.6.2 the position of maximum intensity rotates through four times the angle of rotation of the half wave-plate fast axis.

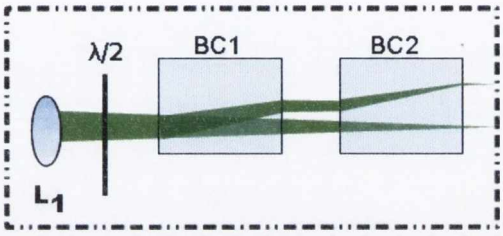

Figure 5-17: Cascade ICR with linear polarised light

Figure 5-18: FIP of cascade ICR for linear polarised light with Δγ = 80° with a ring diameter of $8.5x10^{-4}$ m.

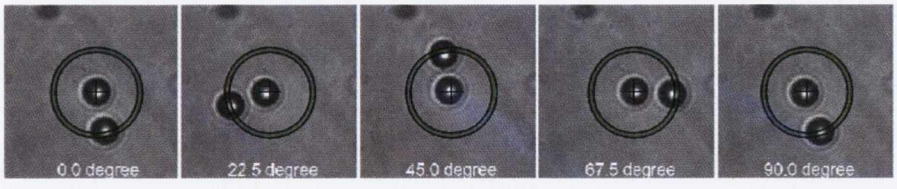

Figure 5-19: Angular positioning of 5.3 μm Polystyrene particles on a ring around a Polystyrene particle optically confined with a central Gaussian trap.

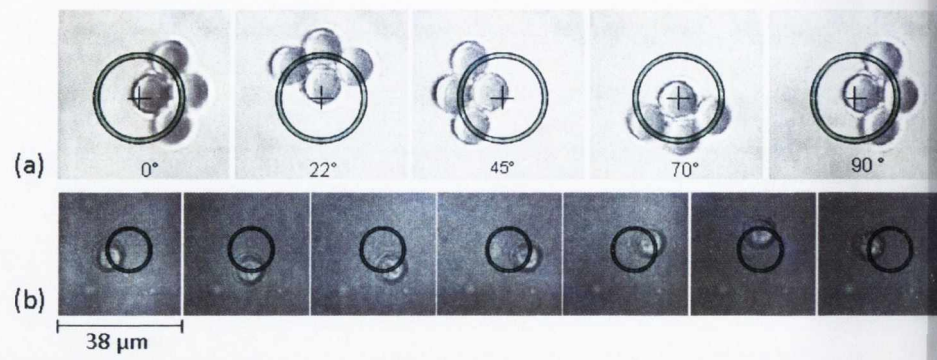

Figure 5-16: Sequence of images the continuous rotation of (a) cluster of 5 µm MF particles, (b) a white blood cell 8 µm in diameter.

5.7 Cascade trapping arrangement

The crystals used in the following cascade experiments are 20.98mm and 21.1mm in length. The resulting geometric ring radii at 532nm are 4.28 $x10^{-4}$ m and 4.31 $x10^{-4}$ m respectively, giving a combined R_0 = 8.59 $x10^{-4}$ m. The second biaxial crystal BC2 is mounted so that it can be rotated about its optic axis without misalignment. The focusing lens L_1 is replaced with a 17cm lens forming $1/e^2$ half width beam waist of 76 µm giving a ρ_0 value of 11.1. Taking into account the increased optical path length of the crystal (1.54cm) the FIP lies 20cm away from the L_1 lens. The resulting ring radius in the trapping plane is 6.2 µm, when $\Delta\gamma > 0^0$ (the angle between successive optic axis of the crystals) a Gaussian beam waist size of 1.24 µm at the $1/e^2$ point is formed. As the BC2 is rotated the central position of the trap will be displaced on a circle of diameter 3.2 µm in the trapping plane (the radius of the R_0 from the first crystal).

Figure 5-19 shows the angular positioning of a 5.3 μm PS particle on the ring of light of radius 7 μm, relative to a particle trapped in the central Gaussian spot. Comparing to section 5.6.2, the particle rotates at four times the rate of the half wave-plate. Continuous rotation of the wave-plate sets the particle into circulation around the centrally trapped particle of equal size. For small $\Delta\gamma$, less than 10^0 degrees, a maximum circulation frequency of .16Hz around a weakly centrally trapped particle was obtained.

For each angle the maximum trapping force is obtained for range of powers with Figure 5-20 showing the increase of the trapping Q value for the central Gaussian spot as BC2 is rotated from zero to 180^0 degrees. The intensity and Q value vary as $\sin^2(\gamma/2)$ as expected. The larger radius of the cascade trap results in a smaller percentage of light interacting with the particle confined upon the ring, resulting in a much smaller trapping efficiency.

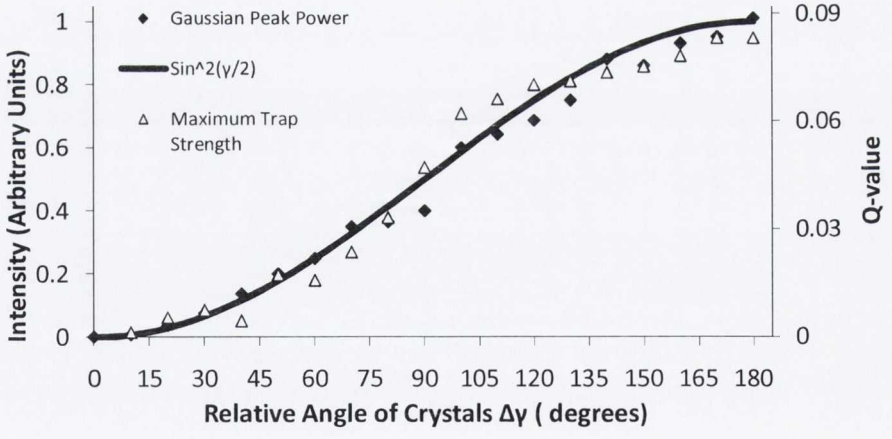

Figure 5-20: Trapping efficiency of Gaussian central spot in cascade setup as a function of relative angle between the crystals.

5.8 Discussion and conclusion

The above basic optical trapping experiments clearly demonstrate the versatility that an optical trap based on conical diffraction can provide. The continuous circulation of a particle whose diameter is smaller than the trapping ring profile has been demonstrated using two clearly distinct mechanisms. The scattering of light with an azimuthal component to the Poynting vector causes a particle to continuously circulate around the ring of light in which it is optically confined. The circulation of a low-grade calcite fragment (≈ 5 μm in diameter) demonstrated the extrinsic nature of the OAM of light. A comparison of the circulation speeds of the fragment showed that the particle in the first order field with 1ħ OAM per photon circulated at twice the rate than when in the combined conical beam with ½ħ per photon. A maximum circulation frequency of 0.34 Hz was observed with 180mW of optical power in the trapping plane. No circulation was observed for the zero order beam. Switching the handedness of the incident polarisation to be right handed changes the circulation direction. This mechanism for circulation is not suitable for the circulation of smooth transparent particles as the azimuthal component to the Poynting vector does not interact with the particle.

The conical diffraction of linear polarised light forms a $\cos^2(\theta/2)$ intensity gradient around the ring in the FIP. The position of the intensity maximum directly depends upon the orientation of linear polarisation incident upon the crystal. Rotating the linear polarisation with use of a half wave-plate rotates the position of maximum intensity through four times the angle of the fast axis of the wave-plate. The position of a trapped Latex particle 5μm in diameter around the circumference of the ring trap was controlled by the angular positioning of a half wave-plate fast axis. The continuous and steady rotation of the wave-plate via a computer controlled mechanical stage, sets the particle into a continuous rotation. This is in contrast to rotation due to OAM

transfer, where the procession rate for a given $\ell\hbar$ beam is controlled via the optical power. This mechanism enables a high optical power to form a stiffer trap giving a maximum achievable circulation speed, which can be easily selected from the circulation frequency of the wave-plate. For a conically diffracting beam with ρ_0 of 7.7 and 5μm radius the trapping efficiency Q = 0.04. This may seem like a low efficiency, however when compared to other similar experiments the value of Q = 0.04 is of the same order of magnitude for trapping efficiencies as other papers with trapping forces of the order of 1pN [40].

A conically diffracting optical trap based on cascade ICR expands upon the previous experimental results providing the added feature of a central Gaussian spot with the same waist and polarisation as the initial generating Gaussian. As the second crystal is rotated with respect to the first the intensity in the Gaussian spot increases as $\sin^2(\Delta\gamma/2)$, and the intensity in the rings decreasing at the same rate. This ability to vary the ratio of intensity between the rings and Gaussian provides a new means to select the trap stiffness ratio between the separate components. Although this is not fully demonstrated at this time, the trap stiffness of the Gaussian varies as expected from no trapping for aligned crystals to a maximum efficiency of Q = 0.09 for anti parallel crystals.

Future experimental work on these conical traps will include the development of a size tuneable ring trap as seen here with an axicon [40], and investigations into Bessel beam optical trapping exploiting the concentric ring pattern and non-diverging nature to sort and stack particles[1,41-44].

5.9 References

1 D. McGloin, "Optical tweezers: 20 years on," Philosophical Transactions of the Royal Society A: Mathematical, Physical and Engineering Sciences **364** (1849), 3521-3537 (2006).

2 Elio A. Abbondanzieri, William J. Greenleaf, Joshua W. Shaevitz, Robert Landick, and Steven M. Block, "Direct observation of base-pair stepping by RNA polymerase," Nature **438** (7067), 460-465 (2005).

3 A. Ashkin, J. M. Dziedzic, J. E. Bjorkholm, and Steven Chu, "Observation of a single-beam gradient force optical trap for dielectric particles," Optics Letters **11** (5), 288-290 (1986).

4 A. Ashkin and J.M. Dziedzic, "Optical trapping and manipulation of viruses and bacteria," Science **235** (4795), 1517-1520 (1987).

5 H. He, M. E. J. Friese, N. R. Heckenberg, and H. Rubinsztein-Dunlop, "Direct Observation of Transfer of Angular Momentum to Absorptive Particles from a Laser Beam with a Phase Singularity," Physical Review Letters **75** (5), 826 (1995).

6 William J. Greenleaf and Steven M. Block, "Single-Molecule, Motion-Based DNA Sequencing Using RNA Polymerase," Science **313** (5788), 801- (2006).

7 A. Ashkin, "Acceleration and Trapping of Particles by Radiation Pressure," Physical Review Letters **24** (4), 156 (1970).

8 A. Ashkin, "Atomic-Beam Deflection by Resonance-Radiation Pressure," Physical Review Letters **25** (19), 1321 (1970).

9 A. Ashkin, "Trapping of Atoms by Resonance Radiation Pressure," Physical Review Letters **40** (12), 729 (1978).

10 A. Ashkin, J. M. Dziedzic, J. E. Bjorkholm, and Steven Chu, "Observation of a single-beam gradient force optical trap for dielectric particles," Opt. Lett. **11** (5), 288-290 (1986).

11 J. P. Gordon, "Radiation Forces and Momenta in Dielectric Media," Physical Review A **8** (1), 14 (1973).

12 J. P. Gordon and A. Ashkin, "Motion of atoms in a radiation trap," Physical Review A **21** (5), 1606 (1980).

13 P. A. Maia Neto and H. M. Nussenzveig, "Theory of optical tweezers," EPL (Europhysics Letters) **50** (5), 702 (2000).

14 A. Ashkin, "Forces of a single-beam gradient laser trap on a dielectric sphere in the ray optics regime," Biophysical journal **61** (2), 569-582 (1992).

15 N. B. Simpson, K. Dholakia, L. Allen, and M. J. Padgett, "Mechanical equivalence of spin and orbital angular momentum of light: an optical spanner," Opt. Lett. **22** (1), 52-54 (1997).

16 Anna T. O'Neil and Miles J. Padgett, "Rotational control within optical tweezers by use of a rotating aperture," Opt. Lett. **27** (9), 743-745 (2002).

17 S. Sato and H. Inaba, "Optical trapping and manipulation of microscopic particles and biological cells by laser beams," Optical and Quantum Electronics **28** (1), 1-16 (1996).

18 Jennifer E. Curtis, Brian A. Koss, and David G. Grier, "Dynamic holographic optical tweezers," Optics Communications **207** (1-6), 169-175 (2002).

19 M. P. MacDonald, L. Paterson, K. Volke-Sepulveda, J. Arlt, W. Sibbett, and K. Dholakia, "Creation and Manipulation of Three-Dimensional Optically Trapped Structures," Science **296** (5570), 1101-1103 (2002).

20 Alexis I. Bishop, Timo A. Nieminen, Norman R. Heckenberg, and Halina Rubinsztein-Dunlop, "Optical Microrheology Using Rotating Laser-Trapped Particles," Physical Review Letters **92** (19), 198104 (2004).

21 S. Maruo, A. Takaura, and Y. Saito, "Optically driven micropump with a twin spiral microrotor," Optics Express **17** (21), 18525-18532 (2009).

22 G. Knöner, S. Parkin, T. A. Nieminen, V. L. Y. Loke, N. R. Heckenberg, and H. Rubinsztein-Dunlop, "Integrated

optomechanical microelements," Optics Express **15** (9), 5521-5530 (2007).

23 K. T. Gahagan and Jr G. A. Swartzlander, "Optical vortex trapping of particles," Optics Letters **21** (11), 827-829 (1996).

24 Justin E. Molloy and Miles J. Padgett, "Lights, action: optical tweezers," Contemporary Physics **43** (4), 241 - 258 (2002).

25 J. Arlt, R. Kuhn, and K. Dholakia, "Spatial transformation of Laguerre–Gaussian laser modes," Journal of Modern Optics **48** (5), 783 - 787 (2001).

26 A. Ashkin, "Forces of a single-beam gradient laser trap on a dielectric sphere in the ray optics regime," Biophys. J. **61** (2), 569-582 (1992).

27 Bing Shao, Sadik C. Esener, Jaclyn M. Nascimento, Michael W. Berns, Elliot L. Botvinick, and Mihrimah Ozkan, "Size tunable three-dimensional annular laser trap based on axicons," Opt. Lett. **31** (22), 3375-3377 (2006).

28 E. Higurashi, H. Ukita, H. Tanaka, and O. Ohguchi, "Optically induced rotation of anisotropic micro-objects fabricated by surface micromachining," Appl Phys Lett **64** (17), 2209-2210 (1994).

29 Gregor Knöner, Simon Parkin, Timo A. Nieminen, Vincent L. Y. Loke, Norman R. Heckenberg, and Halina Rubinsztein-Dunlop, "Integrated optomechanical microelements," Opt. Express **15** (9), 5521-5530 (2007).

30 Peter Galajda and Pal Ormos, "Complex micromachines produced and driven by light," Applied Physics Letters **78** (2), 249-251 (2001).

31 Samarendra K. Mohanty, Abha Uppal, and Pradeep K. Gupta, "Self-rotation of red blood cells in optical tweezers: prospects for high throughput malaria diagnosis," Biotechnology Letters **26** (12), 971-974 (2004).

32 M. V. Berry, "Paraxial beams of spinning light," SPIE Optical Engineering Press **3487**, 6-13 (1998).

33 M. E. J. Friese, H. Rubinsztein-Dunlop, N. R. Heckenberg, and E. W. Dearden, "Determination of the force constant of a single-beam gradient trap by measurement of backscattered light," Appl. Opt. **35** (36), 7112-7116 (1996).

34 N. B. Simpson, K. Dholakia, L. Allen, and M. J. Padgett, "Mechanical equivalence of spin and orbital angular momentum of light: an optical spanner," Optics Letters **22** (1), 52-54 (1997).

35 S. S. R. Oemrawsingh, E. R. Eliel, G. Nienhuis, and J. P. Woerdman, "Intrinsic orbital angular momentum of paraxial beams with off-axis imprinted vortices," J. Opt. Soc. Am. A **21** (11), 2089-2096 (2004).

36 A. T. O'Neil, I. MacVicar, L. Allen, and M. J. Padgett, "Intrinsic and Extrinsic Nature of the Orbital Angular Momentum of a Light Beam," Physical Review Letters **88** (5), 053601 (2002).

37 R. M. Berry and H. C. Berg, "Absence of a barrier to backwards rotation of the bacterial flagellar motor demonstrated with optical tweezers," Proceedings of the National Academy of Sciences of the United States of America **94** (26), 14433-14437 (1997).

38 M. Ota, H. Okano, and M. Yoshida, "Manipulation of micro solid particles and induced flows in water by laser irradiation," Journal of Thermal Science **16** (2), 176-180 (2007).

39 R. L. Eriksen, P. J. Rodrigo, V. R. Daria, and J. Glückstad, "Spatial Light Modulator Controlled Alignment and Spinning of Birefringent Particles Optically Trapped in an Array," Applied Optics **42** (25), 5107-5111 (2003).

40 B. Shao, S. C. Esener, J. M. Nascimento, M. W. Berns, E. L. Botvinick, and M. Ozkan, "Size tunable three-dimensional annular laser trap based on axicons," Optics Letters **31** (22), 3375-3377 (2006).

41 T. Cizmar, M. Siler, and P. Pemanek, "Sub-micron particle organization by
self-imaging of non-diffracting beams," New Journal of Physics **8** (443) (2006).

42 V. Garces-Chavez, D. Roskey, M. D. Summers, H. Melville, D. McGloin, E. M. Wright, and K. Dholakia, "Optical levitation in a Bessel light beam," Applied Physics Letters **85** (18), 4001-4003 (2004).

43 T. Cizmar O. Brzobohaty, P. Zemanek, "High qualiy quasi-Bessel beam generated by round-tip axicon," Optics Express **17** (16), 12688 (2008).

44 A. Hiroto, "Orbital motion of spherical microparticles trapped in Diffraction patterns," Physical review A. **75** (2007).

Chapter 6

CONCLUSIONS AND FUTURE WORK

6.1 Conclusions

The first detailed scientific investigation into ICD has now been carried out here in Trinity College Dublin since the initial work by Hamilton and Lloyd more than 180 years ago. During the intervening years there have been sporadic investigations, both experimental and theoretical into this most curious of optical effects. The purpose of this thesis was to investigate the newly reformulated phenomenon of internal conical diffraction as proposed by Berry[1] in 2004. The preliminary work performed by Berry *et. al.* provided the theoretical groundwork for this thesis. Chapter 2 outlined the theory of ICD in terms of the geometric wave and ray surfaces. The paraxial wave theory describes the conical beam in terms of a superposition of orthogonally polarised Bessel beams of differing order. A circularly polarised Gaussian beam is transformed into a superposition of orthogonally polarised modes whose radial electric field profiles are described by Bessel functions of zero and first order.

Chapter 3 discussed the SAM to OAM conversion in a conically diffracted field using a Gaussian beam. It has been shown previously that a circularly polarised incident beam with a SAM of $+1\hbar$ is transformed into a pure OAM state of $+½\hbar$ per photon. The final OAM state consists of two orthogonally polarised fields one with a vortex of the same handedness as the incident polarisation and the other without a vortex. These two vortex states can be easily isolated because they are orthogonally polarised at all points around R_0. Isolating the vortex state yields a first-order Bessel beam with an OAM of $1\hbar$ per photon. Linear incident polarised light with zero SAM is converted into a beam with zero OAM per photon. This chapter described the conversion of elliptically polarised light with a non-integer SAM per photon into a non-integer OAM per photon. The OAM per photon of the isolated vortex beam does not correspond to the incident SAM per photon, this was a result of the zero and first-order beams not being orthogonally polarised

at all points around R_0. Isolating the vortex beam resulted in an unequal division of power between the zero and first-order beams enabling the measurement of the OAM per photon. This work led to the publication of the paper, D. P. O'Dwyer, C. F. Phelan, Y. P. Rakovich, J. F. Donegan, and J. G. Lunney, "Generation of continuously tunable fractional optical orbital angular momentum using internal conical diffraction," Optics Express, Vol. 18, Issue 16, pp. 16480-16485 (2010).

Chapter 4 discussed the theoretical and experimental process of cascade ICD. Firstly, the SAM to OAM conversion process of the previous chapter was extended to examine the conversion process of a circularly polarised optical vortex. The optical vortex component generated from a circularly polarised Gaussian beam was isolated and re-circularly polarised before being re-conically diffracted through a second biaxial crystal. If the vortex and polarisation are of same handedness such that the total AM incident is $+2\hbar$ the final beam will have a pure OAM state of $1\frac{1}{2}\hbar$ per photon, composed of first (ℓ =1) and second order (ℓ = 2) optical vortices in superposition. Alternatively, if the vortex and polarisation are of opposite handedness such that the total AM incident is $0\hbar$, the generated beam will have a pure OAM state of $\frac{1}{2}\hbar$ per photon composed of first (ℓ =1) and zero-order (ℓ = 0) optical vortices in superposition. This demonstrates the ability of ICD to control both the SAM and OAM of a light field using standard polarisation optics and a biaxial crystal. This section also provided the theoretical groundwork for the transformation of any circularly polarised optical vortex state. This work closely resembled the paper by King[3], which described the transformation of a circularly polarised non-diffracting Bessel beam through a series of cascaded biaxial crystals. While the cascade work in this thesis uses the same process of cascaded biaxial crystals, our work describes the transformation and subsequent diffraction profile of a circularly polarised Gaussian beam through successive biaxial media. This work closely resembled the paper by King[3], which described the

transformation of a circularly polarised non-diffracting Bessel beam through a series of cascaded biaxial crystals. While the cascade work in this thesis uses the same process of cascaded biaxial crystals, our work describes the transformation and subsequent diffraction profile of a circularly polarised Gaussian beam through successive biaxial media. This lead to the publication entitled, D. O'Dwyer, C. Phelan, Y. Rakovich, P. Eastham, J. Lunney, and J. Donegan, "The creation and annihilation of optical vortices using cascade conical diffraction," Optics Express 19, 2580-2588 (2011).

Chapter 5 discused the use of ICD in a range of different optical trapping geometries. A conical beam generated from circularly polarised light is circularly symmetric with $\pm\frac{1}{2}\hbar$ OAM per photon. That is composed of easily separable OAM states of 0 and $\pm 1\hbar$ per photon. Transparent dielectric spheres whose diameter is smaller than the ring in the trapping plane are confined around the circumference of the ring. If the light incident upon the crystal is linearly polarised a gradient of intensity is formed around R_0 confining the particle at the point of highest intensity. Rotating the plane of polarisation incident upon the crystal rotates the point of maximum intensity on the ring, displacing the equilibrium position of the trapped particle. The orientation of the wave plate fast axis corresponds to the position of maximum intensity enabling the angular positioning of a particle on the circumference of the ring trap. Setting the wave plate into continuous motion sets the trapped particle into continuous motion, mimicking the circulation properties of the OAM trap without the complication of absorption or scattering. This work was successfully published, D. O'Dwyer, C. Phelan, K. Ballantine, Y. Rakovich, J. Lunney, and J. Donegan, "Conical diffraction of linearly polarised light controls the angular position of a microscopic object," Optics Express 18, 27319-27326 (2010).

Other possible trapping geometries using cascade ICD were also presented in this chapter. The cascade arrangements using a

pair of biaxial crystals generated a conical ring and Gaussian spot. The ratio of optical power between the central Gaussian spot and ring can be easily determined upon selecting the appropriate angle between the crystals. If the incident light is circularly polarised the ring trap is circularly symmetric, with the central Gaussian spot being circularly polarised with the same handedness as the incident Gaussian beam. Linearly polarised incident light generates a linearly polarised Gaussian spot. This arrangement enables the circulation and angular positioning of a particle trapped in the ring around a centrally trapped particle. This work was observed experimentally and as of time of publication has not been published.

6.2 Future work

When I started my research into ICD it was regarded as an optical side note or curiosity and did not have a particular practical use apart from a nice demonstration of singular optics. Over the course of this research, mainly due in part to the availability of laser grade biaxial materials, there has been a resurgence of interest into ICD. Papers on topics such as a conically diffracting laser to laser beam shaping have been proposed. The contribution from this project in conjunction with its sister thesis by Phelan has resulted in publications that have revealed the finer details of ICD. These publications have covered the OAM properties of the conical beam, cascaded conical diffraction and a conically diffracting optical trap.

The work performed in Chapter 3 on the OAM properties of the conical beam bring conical diffraction into the regime of quantum mechanics, something quite fitting considering Hamilton's link with quantum mechanics. If we compare the biaxial crystal to its most similar counterpart the "q-plate", the route of future experimental work required is quite clear. The "q-plate" device is being marketed as a cost effective way to convert and manipulate OAM using polarisation optics

for the field of quantum information[4]. In order for ICD to become a real competitor (if it is at all feasible), single photon measurements must be performed.

The optical trapping work performed in this thesis provides an insight into the capabilities of a conically diffracting optical trap using a basic setup. It has been proposed that the rudimentary optical trap be transferred to a SNOM optical microscope equipped with high NA oil based objective could increase the trapping efficiency. Further possible enhancements include the integration of a zoom lens to dynamically change R_0, and hence change the magnification in the objective plane. This will provide a trapping geometry that can be adjusted for a range of particles.

The ring and Gaussian beam provided by the cascade trap could also allow for the generation of a highly efficient trapping geometry previously proposed by Ashkin. The combination of a ring plus axial beam incident upon the back of the objective maximises the effect of the NA meridian rays whilst the axial Gaussian beam compensates for the reduced lateral trapping efficiency provides the best theoretical trapping geometry for a single particle.

The other main area of interest that was not explored was trapping in the non-diffracting Bessel regime. Reviewing the literature on Bessel beam trapping yields a wide are of interest in these particular traps. In designing the trap for this thesis it was decided that making a ring trap would yield more unique results instead of repeating all ready published Bessel beam based optical traps. The typical uses of Bessel beam optical traps are tasks such as particle stacking along the beam core and sorting and separating particles according to size[5-6]. The ability of the conical beam to flip between a zero and 1st order Bessel beam provides a greater flexibility over other methods of generating Bessel traps. Flipping the handedness of the incident polarisation upon the crystal is

much simpler and quicker than changing the laser mode incident upon an axicon.

One avenue of research that was only briefly investigated and not discussed in this thesis is the conical diffraction of white light. The wave surface used in chapter 2 to describe conical refraction assumed that the light being refracted was of a single wavelength, and hence the direction of the optic axis was fixed. A white light source, like that provided by a Xenon lamp generates a wide spectral range of wavelengths over the visible range. The direction of the optic axis is wavelength dependent. Figure 6-1 shows the dispersion of the white light, as it is double refracted; notice the dispersion of the different wavelengths. As the light is directed towards the optic axis, the rays are refracted around the conical point of intersection leading to the formation of conically refracted white light. This leads to the possibility of forming white light Bessel beams.

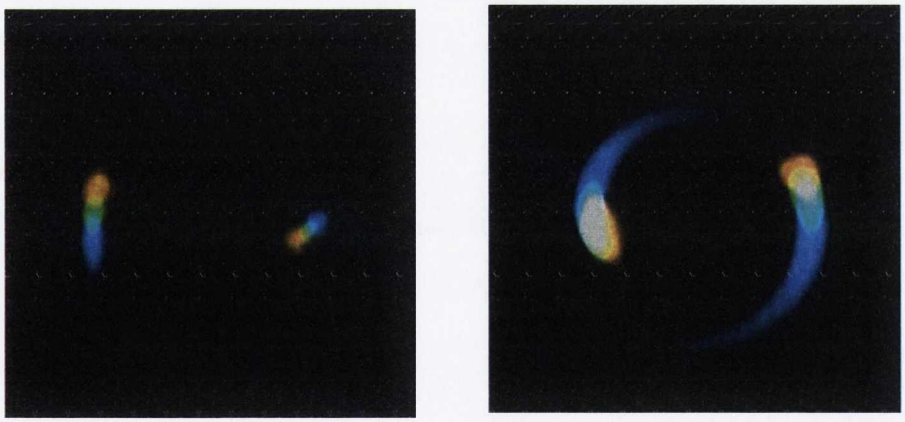

Figure 6-1: Experimental profiles of the conical diffraction of white light

6.3 References

1 M. V. Berry, "Conical diffraction asymptotics: fine structure of Poggendorff rings and axial spike," Journal of optics A: Pure and applied optics. **6**, 289 (2004).

2 M. V. Berry, M. R. Jeffery, and J. G. Lunney, "Conical diffraction: Observations and theory," Proceedings of the Royal Society A. A **462**, 1629-1642 (2006).

3 T. A. King, W. Hogervorst, N. S. Kazak, N. A. Khilo, and A. A. Ryzhevich, "Formation of higher-order Bessel light beams in biaxial crystals," Optics Communications **187** (4-6), 407-414 (2001).

4 E Karimi, B Piccirillo, E Nagali, L Marrucci, and E Santamato, "Efficient generation and sorting of orbital angular momentum eignmodes of light by thermally tuned q-plates," Applied Optics **94** (23), 231124 (2009).

5 T. Cizmar O. Brzobohaty, P. Zemanek, "High qualiy quasi-Bessel beam generated by round-tip axicon," Optics Express **17** (16), 12688 (2008).

6 A. Hiroto, "Orbital motion of spherical microparticles trapped in Diffraction patterns," Physical review A. **75** (2007)

3 P. Fischer, C. Brown, J. Morris, C. López-Mariscal, E. Wright, W. Sibbett, and K. Dholakia, "White light propagation invariant beams," Optics Express **13** (17), 6657-6666 (2005).